Single-Photon Technologies based on Quantum-Dots in Photonic Crystals:

from sources to application

A dissertation
submitted to the Niels Bohr Institute
at the University of Copenhagen
in partial fulfillment of the requirements
for the degree of
philosophiae doctor

Tau Bernstorff Lehmann
May 20, 2016

Single-Photon Technologies based on Quantum-Dots in Photonic Crystals:

from sources to application

Preface

The research presented in this thesis was carried out between February of 2013 and April of 2016. The majority of the research presented in the thesis was conducted in Professor Peter Lodahls group at Niels Bohr Institute in Copenhagen. During this time a collaboration with Professor Andrew White at the University of Queensland was conducted from October 2015 to December 2015. The research from this collaboration is presented in Chap. 7.

I would like to thank Peter Lodahl for supervising the project and challenging me to further my research. I would also thank Peter for giving me the opportunity to work in his group and in his lab.

I would like to extend my huge gratitude to my colleagues. Both the academic and social aspect of the group is a mayor element driving my continuous motivation for the research we conduct.

I would like to thank Kristian Høeg Madsen, who introduced me to the life as an experimental physicist. Kristian's commitment to and excitement about research was very motivating to me. Also the knowledge I gained from working with Kristian was essential to my ph.d.

I would also like to thank Immo Söllner, Alisa Javadi and Marta Arcari Madsen for their time as lab partners. Their willingness to always discuss issues and ideas not related to their own research has often rescued me from committing mistakes or wasting time.

I am very grateful to Gabija Kirsanské, Tomasso Pregnolato and Leonardo Midolo for producing the samples used in the experiments. Their commitment to fabricate samples at all hours of the week made a big difference for the results obtained during my ph.d.

A huge gratitude is owed to Juan Loredo, Marcelo De Almeida, Andrew White and the rest of the Quantum Information group at University of Queensland, for having me visit their group and collaborating on the work presented in Chap. 7. I am very thankful for their hospitality and for making me feel as part of the group.

Finally, the deepest thank you is owed to Helene, whose support of me has been unwavering. I am grateful and fortunate to have her in my corner. I am also grateful for my parents Marianne and Anders, and my siblings Sif and Jon, as well my family and friends, who have offered support and encouragement when things looked bleak.

Abstract

In this thesis, the application of semiconductor quantum-dots in photonic crystals is explored as a resource for single-photon technology.

Two platforms based on photonic crystals, a cavity and a waveguide, are examined as platforms single-photon sources. Both platforms demonstrate strong single-photon purity under quasi-resonant excitation. Furthermore the waveguide based platform demonstrates indistinguishable single-photons at timescales up to 13 ns.

A setup for active demultiplexing of single-photons to a three-fold single-photon state is proposed. Using a fast electro-optical modulator, single-photons from a quantum-dot are routed on timescales of the exciton lifetime. Using active demultiplexing a three-fold single-photon state is generated at an extracted rate of 2.03 ± 0.49 Hz.

An on-chip power divider integrated with a quantum-dot is investigated. Correlation measurement of the photon statistic verifies the single-photon nature of the quantum-dot. Furthermore correlation measurement between the outputs of the power divider confirms the passive separation of the single-photon emission.

A scheme for post-emission entanglement generation between single-photons from an efficient source is discussed. The possible applications of post-emission entanglement generation are presented. An experimental realization of the scheme are constructed and characterized using single-photons from an efficient source.

Resumé

I denne afhandling, undersøges muligheden for at benytte halvleder kvantepunkter i fotoniske krystaller som en resourse for enkelt foton teknologi.

To platforme baseret på fotonisk krystaller, en kavitet og en bølgeleder, undersøges som platforme for enkelt foton kilder. Begge platforme demonstrerer stærk enkelt foton renhed under kvasi-resonant eksitation. Ydermere demonstrerer den bølgerleder baseret platform uskelnelig enkelt foton på tidskalaer op til 13 ns.

Et design for aktiv demultiplexing af enkelt fotoner til en tre foldig enkelt foton tilstand bliver foreslået. Ved at benytte en hurtig elektro-optisk modulator, bliver enkelt fotoner fra et kvantepunkt dirigeret på en tidskala sammenlignlig med eksiton levetiden. Ved at benytte aktiv demultiplexing generes en tre foldig enkelt foton tilstand med ekstraheret rate på 2.03 ± 0.49 ns.

En on-chip effekt deler integreret med et kvantepunkt bliver undersøgt. Korrelation målinger af foton statistiken verificerer kvantepunktets enkelt foton natur. Ydermere bekræfter en korrelation måling mellem effekt delerens udgange den passive seperation af enkelt foton emissionen.

En metode for post-emission skabelse af sammenfiltring mellem enkelt fotoner udsendt af en effektive kilde diskuteres. De mulige anvendelser af post-emission sammenfiltring skabelse præsenteres. Opstilling for metoden realiseres eksperimentelt og karakteriseres ved hjælp af enkelt fotoner fra en effektiv kilde.

List of Publications

The work performed in the work of this Ph.D.-project has resulted in the publications listed below:

Journal Publications

1. P. Tighineanu, R. S. Daveau, T. B. Lehmann, H. E. Beere, D. A. Ritchie, P. Lodahl, and S. Stobbe. *Single-photon superradiance from a quantum dot*, Physical Review Letters, **116**, 163604 (2016).

Journal Publications in Preparation

1. K. H. Madsen, T. B. Lehmann, and P. Lodahl. *Role of multi-level states on quantum-dot emission in photonic-crystal cavities*, Submitted.

Contents

We choose to go to the moon.
We choose to go to the moon in this decade and do the other things, not because they are easy, but because they are hard, because that goal will serve to organize and measure the best of our energies and skills, because that challenge is one that we are willing to accept, one we are unwilling to postpone, and one which we intend to win, and the others, too.

John F. Kennedy

Chapter 1

Introduction

The invention of the microchip lead to a revolution in computer development and has had profound impact on the improvement of human life. The computer fulfills no purpose in its own right but enables solving otherwise practical impossible tasks and helped propel man to the moon. The computer has found application in all fields of research. Just as the computer revolutionized several research fields, the quantum computer could usher a second revolution as a new range of problems would become solvable. The quantum computer could have profound impact in simulations of quantum chemistry. Such advancement could have implication for clean energy production and distribution, which currently is the largest challenge facing humanity [1] .

In a classical computer the bit is the building block in which information is encoded, it exist in either the state 0 or 1 and they are mutually exclusive. When combined this simple structure can represent any kind of information, be it text, images or physical systems. The classical computer has been extremely successful but has found its limit when the problems of interest grow with an exponential complexity. The classical computational approach simply can not find a solution in a reasonable amount of time.

The great strength of the quantum computer is gained through quantum parallelism. The building block of the quantum computer is the quantum bit or qubit, in contrast to the classical bit the qubit can exist in a superposition of 0 and 1. This principle enables a quantum computer to generate a superposition of all possible outcomes and thereby perform computation in parallel. The quantum computer should provide an exponential improvement in computational time over a classical computer for a class of problems.

An exciting prospect of quantum computation is quantum simulation. First proposed by Richard Feynman [2] the idea is to let nature simulate nature, meaning if one system is controlled to behave like another, it can simulate properties of the system of interest. Quantum simulation would find strong applications in quantum chemistry and material science, where simulating quantum system on classical computers becomes so complex even supercomputers must resign.

The requirements for a successful platform for quantum computing are formulated in the DiVencenzo criteria [3]. Amongst these are the existence of a qubit with two orthogonal states, the ability to protect the state against decoherence and the ability to perform operations from an universal set of gates. There are several platforms vying to become the leading platform for quantum computing, among the top contenders are superconducting qubits, trapped ions and single-photons. Recent devel-

opments in single-photon technologies means practical implementation of quantum computers using single-photon qubits has become a reality.

Quantum information processing consists of a wealth of subcategories and can roughly be divided into universal quantum computers and special purpose quantum computers. A universal quantum computer is a reconfigurable entity that performs a universal set of quantum gate operations. This enables it to perform any protocol formulated in terms of these gates. Such a quantum computer is the end goal of research into quantum information, but the technical requirements for such a device ares substantial and the time line is uncertain.

Though the end goal may be far in the horizon there are many powerful applications that can be fulfilled with special-purpose quantum computers. These devices are quantum computers that work for a specific protocol, such as a quantum simulation of chemical complexes or solving intractable mathematical problems. Though not universal these devices are still very desirable for their potential to provide insights, which otherwise are obscured by complexity.

The purpose of this work is to develop technologies for single photon application, which components are diverse and only a limited part can be covered here.

This thesis begins with a treatment of solid-state quantum dots as single-photon sources. This leads to the discussion of a method to generate single-photon states for quantum computing. Finally an application of indistinguishable single-photons for entanglement generation is discussed. Entangled states are a potentially a route to quantum information processing. The thesis hereby covers single-photon technologies from the sources to potential applications.

The outline of the thesis is as follows: the following chapter contains an introduction to the leading technologies in quantum computing. A strong focus will be placed on the single photon qubit and the recent technological progress that has enabled this optical quantum computing to be among the front runner of quantum information processing.

Chap. 3 a theoretical investigation of the role of the quantum exciton complex in forming exotic states.

Chap. 4 is dedicated to the experimental exploration of the viability of solid-state quantum dots in photonic structures as a platform for single photon technology.

In Chap. 5 a scheme to alter consecutive single photons into a source of multiple temporally synchronized single photons is discussed. This scheme is then experimentally demonstrated using single photons emitted from a solid-state quantum dot.

Chap. 6 presents and demonstrates a design for integrating an optical beamsplitter and a non-classical light source on the same chip.

Finally in Chap. 7, a scheme for generating event-ready entangled photons from indistinguishable single photons using measurement is discussed. The relevant setup is constructed and the feasibility of applying a semiconductor quantum dot as the single photon source is examined.

Chapter 2

Single-photon technologies

Quantum technology is among the most exciting current research topics and is gathering an intense focus [4]. Quantum technology has with the ability to manipulate single quanta systems with high precision matured to an extend, where some of the most daring proposals no longer seem impossible.

One such proposal is quantum simulation as suggested by Richard Feynman [2]. The idea is to use a well controlled physical system to simulate another, which might appear simple, but the realization of a well controlled quantum system is a significant scientific challenge and the system must fulfill the DiVincenzo criterion [3]. The first of these requirements is the existence of a qubit, a particle that can exist in a superposition of two orthogonal states. Also required is the ability to prepare the qubit in a desired state and to preserve it against decoherence. Also needed is the ability to perform gate operations between qubits and to read-out the qubit state. Finally for the platform to be scalable the addition of qubits must not cause an exponential increase in required resources [5]. This means the success probability of state preparation and gate operation must be robust against an exponential scaling.

In this chapter some of the key components of single-photon technology for quantum information processing is reviewed and discussed.

2.1 The Qubit

The basis of all quantum computing is the qubit. A qubit is a physical entity that exists in a superposition of two orthogonal states. The two states are denoted $|0\rangle$ and $|1\rangle$. Single qubit operations are rotations around the Blochs sphere, e.g. transforming between the qubit states $|0\rangle \rightarrow |1\rangle$ or prepare the qubit in a superposition of the two states $|\psi\rangle = \frac{1}{\sqrt{2}}(|0\rangle + |1\rangle)$, finally rotations of the single qubits phase is required.

To perform computations, two-qubit operations are required. The control-not (CNOT) operations, known from classical computation, in addition to single qubit operation is sufficient to construct a universal set of gates, enabling the construction of universal quantum computer. The two-qubit CNOT gate flips the value of the target qubit $|0\rangle_t$ if the control qubit is $|1\rangle_c$ and nothing happens otherwise.

The truth table of the gate is:

$$|0\rangle_t|0\rangle_c \underset{\text{CNOT}}{\rightarrow} |0\rangle_t|0\rangle_c \tag{2.1}$$

$$|1\rangle_t|0\rangle_c \underset{\text{CNOT}}{\rightarrow} |1\rangle_t|0\rangle_c \tag{2.2}$$

$$|0\rangle_t|1\rangle_c \underset{\text{CNOT}}{\rightarrow} |1\rangle_t|1\rangle_c \tag{2.3}$$

$$|1\rangle_t|1\rangle_c \underset{\text{CNOT}}{\rightarrow} |0\rangle_t|1\rangle_c \tag{2.4}$$

The quantum CNOT gate deviates from its classical counterpart, when the target, control or both qubits are prepared in a superposition.

Some systems show significant potential for constructing well controlled qubits, e.g. superconducting qubits and ions [6, 7]. Superconducting qubits demonstrates coherence times in the order of tens μs, which far exceeds the gate operation times of hundreds of ns [8]. The operation fidelity of the gates is also demonstrated to be in the excess of 99%.

Trapped ions have been the leading architecture for quantum information processing, here ions are trapped in space using varying radio frequency fields. The basis of the qubit is two internal energy states of the ion in the trapped potential. Manipulation and read-out of the internal state of the single ions are achieved through targeting the ions with laser pulses [9].

Two qubit operations are enabled through Coulomb interaction between the ions, as the motion of an ion couples to neighboring ions through the Coulomb interaction. This means the ions are coupling through phononic modes, as a collective movement. If both ions are in their respective excited state an overall phase shift is acquired, while the state is unchanged otherwise [9]. This operation is characterized as the controlled-phase (CPhase) operation. Through single qubit rotations it is possible to utilize the phase shift to induce a controlled state flip, thereby constructing a CNOT gate.

The long coherence times of 50 s makes trapped ions extremely desirable as qubits and near unity gate fidelity is achievable [10]. At present these properties are not yet achieved in a single system [11]. A major challenge of ions as a platform for quantum information processing is the technical obstacles of ion trapping, these challenges are potentially reduced by the introduction of micro fabricated ion traps and could cause trapped ions to see wide scale application [12].

The optical qubit

Another very promising qubit candidate is the single-photon. A single-photon is a light pulse that contains only one photon and is an attractive qubit as it is naturally well protected against decoherence owing to its weak interaction with its surrounding. There are several physical bases where a single-photon have orthogonal states, e.g. polarization or time. The polarization of the photon is an useful basis as it is possible to manipulate and separate the two orthogonal states using simple linear components, such as polarizing beamsplitters and halfwave plates. A single-photon's viability as a qubit is characterized by two figures of merit, one is the single-photon purity, i.e. how often does a single pulse contain more than a single-photon, any deviation from a pure single-photon source will cause imperfections in the results of the desired process. The single-photon purity is evaluated using a Hanburry-Brown-Twiss (HBT) experiment [13], where a photon stream is sent on a 50:50 beamsplitter and the correlation of the detected events of the outputs are recorded, as shown in Fig. 2.1. The

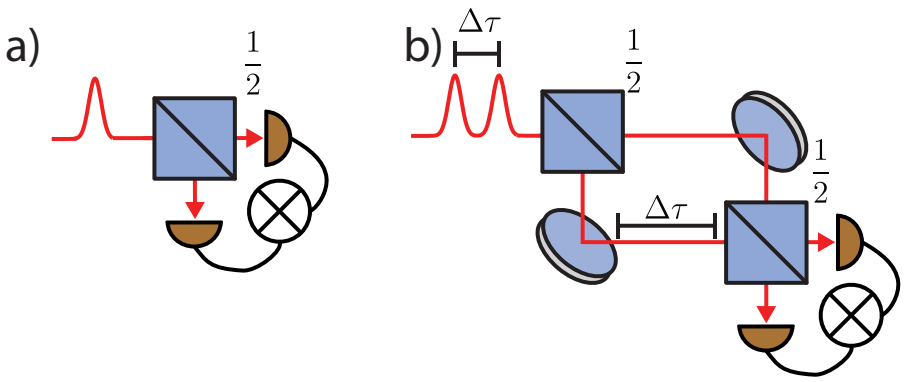

Figure 2.1: **a)** A sketch of a HBT setup. A pulse is sent onto the beamsplitter, the output of the beamsplitter is measured by photo-detectors and the measurements are correlated. If the pulse contain a single photon, no correlation at zero time delay is measured. **b)** A sketch of HOM interferometer. Two single-photons, temporally spaced by $\Delta\tau$, are coupled into the interferometer. The path length difference of the two arms is matched to $\Delta\tau$ and the two paths are recombined on the second beamsplitter. The photon statistics are measured using single-photon detectors and correlated.

recorded correlation reveals the photon statistics of the photon source, as the normalized correlation function $g^{(2)}(\tau)$ is related to the photon statistic:

$$g^{(2)}(\tau) = \frac{\langle \hat{a}^\dagger \hat{a}^\dagger \hat{a}\hat{a} \rangle}{\langle \hat{a}^\dagger \hat{a} \rangle^2} = 1 + \frac{\langle \Delta \hat{n}^2 \rangle - \langle \hat{n} \rangle}{\langle \hat{n} \rangle^2} \tag{2.5}$$

Here $\hat{a}^\dagger(\hat{a})$ is the photon creation (annihilation) operator, $\hat{n}$ is the photon number of the and $\Delta\hat{n}$ is the standard deviation of the photon number. The correlation can distinguish between a thermal state where $g^{(2)}(0) = 2$, a coherent state where $g^{(2)}(0) = 1$ and the Fock state of $n = 1$ where $g^{(2)}(0) = 0$. If only a single-photon is entering the beamsplitter no correlation is detected, while pulses with more than a single-photon yields a correlation at the zero time delay. When distinguishing between higher photon number Fock states is desired, the HBT scheme is readily extended to higher photon numbers and the corresponding higher order correlation function can reveal the photon number.

The second figure of merit is the single-photon indistinguishability of two photons emitted from the same or different sources. The indistinguishability of the single-photons is a measure of the overlap between two single-photons in all bases, e.g. frequency, polarization and optical mode. The indistinguishability is characterized by the observation of two photon interference in a Hong-Ou-Mandel (HOM) experiment [14]. In order to show HOM interference, two photons enter a beamsplitter on either side, when the temporal mismatch between the arrival time is less than the coherence time of the photons of interest interference can occur. The probability amplitude of both photons being transmitted and both photons being reflected are equal and opposite. The opposite amplitudes means these terms cancel and causes a bunching of the photons, where the two photons exit the beamsplitter together. The bunching causes an absence of temporal correlation events between the two outputs of the beamsplitter. The absence of correlation occurs if the two photons are indistinguishable and the pulses contains single-photons.

If the source emits a continuous stream of single-photons the HOM interference experiment is setup as a Mach-Zender interferometer, as seen in Fig. 2.1 (b). The single-photons are separated by $\Delta\tau$ and a path length difference between the arms is induced to match $\Delta\tau$. The two paths are recombined on

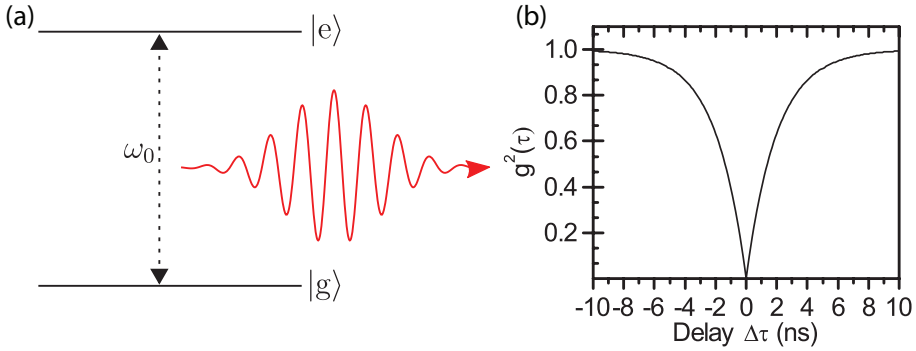

Figure 2.2: **a)** A sketch of a two-level system. The excited state $|e\rangle$ is separated from the ground state $|g\rangle$ by $\hbar\omega_0$. The spontaneous decay of $|e\rangle$ causes the emission of a single-photon with frequency ω_0 **b)** Normalized correlation function for a single-photon source with a decay rate $\gamma = 1\,\mathrm{ns}^{-1}$. At zero time delay there are no correlation as it is a single-photon source. When the delay is increased the probability of the source emitting a second photon increases causing the correlation to rise.

the second beamsplitter and in $\frac{1}{4}$ of the events the temporal difference between the single-photons is removed and the single-photons interfere at the beamsplitter. The exiting single-photons are detected and the events are temporally correlated.

2.2 Technologies for optical qubits

There are several schemes to generate single-photons for quantum information applications and Spontaneous Parametric Down Conversion(SPDC) is currently the most utilized source of photonic qubits. In SPDC a laser is used to pump a nonlinear crystal, where inside a single pump photon is separated into two photons, which is used to generate photons of equal energy with a large spectral overlap. When the pump photon is split the energy must be conserved, i.e. $\omega_{\mathrm{Pump}} = \omega_{\mathrm{Signal}} + \omega_{\mathrm{Idler}}$ where ω_{Signal} (ω_{Idler}) is the frequency of the signal (idler) photon, as the momentum is also conserved a similar equation exist for the wavevector $\mathbf{k}_{\mathrm{Pump}}$.

If the signal and idler photon are spectrally distinguishable a filter is used to separate the two photons, the creation of the photon pair is heralded by the detection of the idler photon [15]. The detection of an idler photon heralds the signal mode in a single-photon state and a single-photon source is achieved. If the two photons have equal energy the conservation of momentum is used to have the two photons propagate in orthogonal modes and makes it possible to collect both photons. As the signal and idler photon have the same frequency they demonstrate strong two-photon interference and single-photons produced from SPDC is applicable as optical qubits [14]. In order to scale to more than two photons similar devices is utilized to generate multiple indistinguishable single-photons.

The generation of single-photons in SPDC is probabilistic and inefficient. In order to overcome the inefficient generation procedure the intensity of the pump laser is often increased, leading to generation of multiple simultaneous pairs. Multiple pair generation means that the single-photon purity of the source is degraded. The inefficiency of SPDC makes it unsuitable for scalable applications.

Deterministic photon sources

To realize a single-photon source with a near unity efficiency, it has to be a deterministic source emitting single-photons on demand. A two-level system is a deterministic source, here an electron in an excited state decays to the ground state and spontaneously emit a single-photon. As the two-level system supports a single excitation only single-photons are emitted. In Fig. 2.2 (a) a two-level system is sketched, it is comprised by an excited state $|\mathrm{e}\rangle$ and ground state $|\mathrm{g}\rangle$, which are separated by the energy $\hbar\omega_0$. Using Fermi's golden rule the spontaneous decay of the excited state and the subsequent emission of single-photon in vacuum, is described by the spontaneous emission rate [16]:

$$\Gamma = \frac{4\omega_0^3}{3\hbar c^3}|\langle e|\mathbf{d}|g\rangle|^2. \tag{2.6}$$

Where $\mathbf{d}$ is the dipole moment operator of the two-level system. Fermi's golden rule shows that the transition between the two-levels must have odd parity to couple to the radiation field, as the dipole moment is an asymmetric operator.

If the two-level system is excited by a continuous wave (C. W.) laser resonant with the transition energy $\omega_{\mathrm{Laser}} = \omega_0$, the correlation of the emitted photons $g^{(2)}(\tau)$ in the weak excitation regime is [17]:

$$g^{(2)}(\tau) = (1 - e^{-\Gamma\tau/2})^2. \tag{2.7}$$

Here Γ is the radiative decay calculated by Fermi's golden rule. In Fig. 2.2 (b) the correlation function of the source is plotted. At $\tau = 0$ the $g^{(2)}(0) = 0$ and the two-level system thereby demonstrates single-photon statistics. As τ approaches the emission time of the emitter $\frac{1}{\Gamma}$, the likelihood of reexciting and emitting a single-photon increases and $g^{(2)}(\tau) \to 1$ for $\tau \to \infty$.

In nature a two-level system is illustrated by a single atom. By resonantly exciting a transition of sodium atom in an atomic beam, a two-level system was realized and antibunching observed thereby demonstrating single-photon emission [18]. Addressing single atoms in an atomic beam limits the interaction time and a deterministic spatial trapping of a single atom offers the opportunity of interaction on longer timescales. Clouds of atoms or a single atom are trapped using magneto-optical traps, where magnetic fields and trapping lasers traps a single atom to form a deterministic single-photon source [19].

Semiconductor quantum-dots

The significant experimental challenges of maintaining a magneto optical trap as well as the limited optical interaction in atomic systems has led to intense research in solid state sources of single-photons. Some of the candidates are nitrogen vacancy (NV) color centers in diamonds [20, 21] and semiconductor quantum-dots (QDs) [22, 23]. QDs are nanostructures consisting of thousands of atoms, as shown in Fig. 2.3 (a). The QDs in this thesis are grown using Stranski-Krastenow molecular beam epitaxy, where a semiconductor material with a low band gap is deposited on a material with unequal lattice constants, the lattice mismatch causes spontaneous island formation of only a couple of mono-layers in order to release the strain [24]. The low band gap island, as seen in Fig. 2.3 (b) is encapsulated by high band gap material forming an electronic confinement potential in three dimensions. The electronic density of states of an electron trapped inside the QD is a δ-function, which means that allowed electronic states in the QD are at discrete energy levels [23].

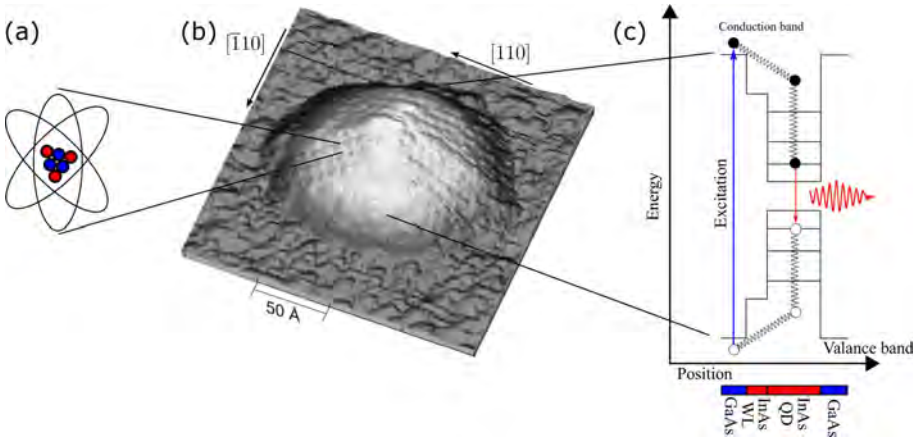

Figure 2.3: **a)** Monolayers of InAs atoms are deposited on GaAs matrix. **b)** The single QD is a consequence of strain release. The two dipoles of the QD aligns with the crystalline axes [110] and [1̄10] of the GaAs host material. Image from Ref. [25]. **c)** Energy confinement potential of the QD. The energy barriers of GaAs traps electrons and holes inside the QD, the three dimensional confinement causes discrete energy states.

The excitation and emission cycle is shown in Fig. 2.3 (c). Using a laser pulse an electron is excited across the electronic band gap, leaving a hole behind. An electron and a hole are trapped by the quantum confinement potential of the QD and due to the Coulomb potential between the two particles an exciton is formed. Through a phonon-assisted cascaded decay process, the exciton is relaxed to the ground state with a relaxation time of few tens of ps [26]. The total angular momentum of the exciton determines if it is radiative active, in which case it is referred to as bright. When the bright exciton decays a photon is spontaneously emitted and as the QD ground state is restricted to a single exciton, the photon statistic is antibunched. [23]. An antibunched photon correlation was demonstrated for InAs QDs embedded in GaAs microdisk [22].

The energy of the ground state exciton is inversely proportional to the size of the QD and as the QDs are formed spontaneously the size of the individual QDs varies and the emission energy likewise. The variation in size is manifested as an inhomogeneous broadening of the QD ensembles emission energies. The growth method thereby causes the formation of an ensemble of QD with various energies. The spatial density of the QDs are also determined by the growth process. The possibility of addressing and detecting a single QD is therefore determined by the spectral and spatial distribution.

The viability of a semiconductor QDs as a resource for optical qubits is dependent on their ability to produce indistinguishable photons. The indistinguishability of the photons emitted is determined by the coherence time of the excitons emitting the single-photons [27]. The coherence of a semiconductor QD is strongly dependent on its environment and is affected by its coupling to noise sources emanating from nuclear spins and charges found in the semiconductor material [28]. These noise sources manifests as a slowly-varying field that modifies the emission frequency of the exciton, which is visible as a spectral broadening of the fundamental line width of the QD. Such noise sources also lower the spectral overlap between two photons emitted from the QD and therefore reduces the two photon interference in a HOM measurement. It is therefore important to reduce the effect of these noise sources, if the QD is utilized as a source of photonic qubits.

Another prominent noise source in solid state QDs are phonons. Since the QDs are situated in a solid state lattice, they couple to the lattice vibrations of the host material. At cryogenic temperatures the population of phonons is low but the QD is able to emit a phonon in conjunction with the emission of a photon, which is manifested as an asymmetric side band [29]. Due to the spectral offset between photons in the phonon sideband and the zero-phonon line, the coupling to phonons causes a reduction in the single-photon indistinguishability.

Enabling scalable systems

Both atoms and QDs are deterministic single-photon sources but the collection of the single-photons emitted is not deterministic. A dipole in a homogeneous material is radiating in a 3d toriod-shaped emission pattern aligned to the orientation of the dipole, which makes efficient collection into a single mode fiber challenging. An atom or a QD has a dipole radiation pattern and modification of the system is required for efficient single-photon collection. By placing the source in an optical cavity, the emission pattern is modified to enable more efficient collection [30, 31, 32]. If the source is on resonance with the cavity mode the spontaneous emission rate is enhanced due to the Purcell effect increasing the emission into the desired mode [33]. Yet the coupling efficiency between atom and cavity mode is limited by the atom's radiative coupling to the environment.

Recently photonic structures demonstrated an enhanced light-matter interface with atoms by suppressing their radiative coupling to the environment [34, 35]. Currently the coupling efficiency of the structures are limited and scalability likewise.

Since QDs are solid state entities they can be integrated into photonic structures in order to enhance light-matter interaction and increase single-photon source brightness. There are various structures used for modifying the emission pattern of solid state QDs, one of the leading candidates are micropillars. These are pillars of high index material, often GaAs, that enables large outcoupling efficiency. The efficient outcoupling is achieved by enhancing the coupling to the cavity mode, while ensuring that the cavity mode is efficiently collected by an microscope objective.

The pillars have a QD embedded inside, often sandwiched between distributed Bragg gratings above and below to enhance interaction. These micro pillars have demonstrated record outcoupling efficiency combined with impressive single-photon purity and indistinguishability [36, 37, 38]. The outcoupling efficiency and the photonic interaction is intrinsically limited by sidewall losses of the pillar. The ability to build integrated circuits using micropillars is limited as the platform is designed around efficient outcoupling to optical fibers.

Photonic crystal

Another platform for enhancing light-matter coupling and outcoupling efficiency of solid state QDs is the photonic crystal [39]. A photonic crystal is a structure where the refractive index is varied in a periodic manner, as seen in Fig. 2.4. The variations in the refractive index causes scattering of the photons, which then interferes. For certain frequencies the Bragg condition is fulfilled and destructive interference occurs in the forward propagating direction and a photonic band gap is induced by the crystal. The band structure of a triangular photonic crystal in a membrane is shown in Fig. 2.4 (b), the optical modes confined by the total internal reflection of the membrane is denoted the slab modes. Above the light line optical modes overcome total internal reflection and couple out of the membrane.

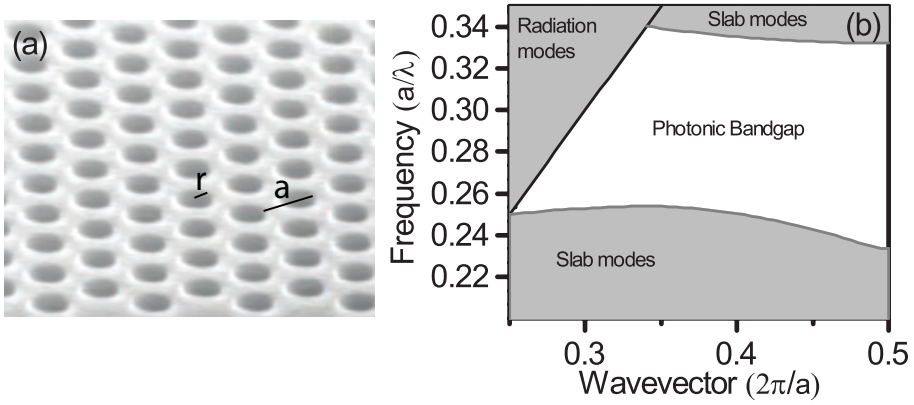

Figure 2.4: **a)** SEM image of a photonic crystal membrane. The hole radius r and the lattice constant a are marked. **b)** A band diagram for the photonic crystal. The guided modes of the unpatterned membrane are the slab modes marked in grey. The slab modes are separated into an upper and a lower band by the photonic band gap marked with white. As the structure is a membrane, light above the light line are not confined by total internal reflection and can couple to radiation modes.

The slab modes are separated by the photonic band gap induced by the photonic crystal. A photonic band gap is the optical analog to an electronic band gap, where photons within this energy band are prevented from propagating in the crystal. Photonic crystals exists in various configurations and have a large unexplored engineering potential.

In this thesis the photonic crystal employed is a two dimensional triangular lattice of air holes etched into a membrane of GaAs. The large contrast in refractive index between air and GaAs causes a strong photonic band gap. The two dimensional photonic crystal causes a strong confinement of photons within the band gap from propagating in the membrane and total internal reflection suppress photons from scattering out of the membrane. A perfect infinite photonic crystal causes a complete suppression of photons inside the band gap, but the fabricated nanostructures often have small fabrication defects, which causes a deviation from the ideal behavior. Recent progress in GaAs fabrication techniques has reduced these imperfections and more complicated structures have become feasible.

Since the photonic crystal prevents photons within the photonic band gap to propagate in the structure, an emitter with an emission frequency inside the band gap positioned in the structure is not able to radiate. A photonic crystal is a powerful tool for modifying the optical density of states experienced by a quantum emitter. The spontaneous emission rate of an emitter is therefore also controllable with photonic crystals [40]. The ability to inhibit the coupling to the environment and thereby the spontaneous decay rate of a quantum emitter, makes photonic crystals a suitable platform for creating high performance optical cavities. By introducing a defect in the otherwise perfect lattice of the photonic crystal, allowed optical states are introduced in the photonic band gap of the local density of states. These defects enhances the coupling to a single optical mode and strong coupling, which enables the observation of single-photon Rabi splitting with a QD. The defect was induced by removing three holes in line from the perfect lattice thereby forming an optical cavity with an ultra-small mode volume and a moderate loss rate. A similar device was demonstrated to have an optical mode that had an efficient outcoupling pattern and in the same context two-photon interference was

shown [41].

Having a moderate coupling between the quantum emitter and a desired mode while suppressing the coupling to all other optical modes have been demonstrated to be a viable path for a highly efficient coupling between a QD and an optical mode of $\beta > 98\%$ [42]. Here the modification of the optical density of states was induced by placing the QD in a photonic crystal waveguide, which is a row defect induced in the perfect lattice. At the edge of the Brillouin zone the Van Hove singularity appears, which induces a strong interaction at the band edge. Due to the suppression of the QD's coupling to other radiation modes, the QD is predominantly coupled to the waveguide mode [42].

Photonic waveguides are a very suitable candidate for integrated on-chip single-photon devices as the optical mode is confined within the chip. This means that on-chip rerouting of single-photons from a efficient single-photon source is viable and thereby circumventing the need for inefficient outcoupling methods [43].

On-chip circuitry

Integrating sources with optical circuits and detectors on the same chip is one of the most promising routes to realizing the necessary system efficiency to enable scalable quantum computation [44]. On chip routing is easily accomplished by rectangular waveguides etched in GaAs. More complex structures such as on-chip beamsplitters have long been utilized in classical communication and are starting to be used in single-photon technologies [45]. Active structures such as microelectro mechanical structures (MEMS) are starting to see a level of maturity where low loss active switching is possible [46], which enable the possibility of reconfigurable networks. Finally integrated superconducting detectors would eliminate the problems of outcoupling losses and inefficient detectors. Combining the various components on a single chip would mean efficient and compact optical quantum networks.

2.3 Computation using optical qubits

Having established indistinguishable single-photons as a photonic qubit and the developing platforms for efficient sources of photonic qubit, the focus is on utilizing the photonic qubit in an optical quantum computer. Optical quantum computing can be achieved by utilizing the quantum phenomena of entanglement [47]. Entangled states show correlations between qubit states, which are not explained by classical theories[48, 49].

Linear Optical Quantum computing

The most utilized quantum computing scheme is Linear Optical Quantum Computing (LOQC) proposed by Knill-Laflamme-Milburn [51]. The scheme is based on linear optical components and is readily implemented using optical beamsplitters and halfwave plates. LOQC utilizes HOM interference of indistinguishable single-photons to generate an entangled state. A successful quantum computation is heralded by detecting ancilla photons.

A LOQM CNOT gate was demonstrated using single-photons from a SPDC soruce, and later from a solid state QD source [50, 52], using the setup sketched in Fig. 2.5. The initial state of the target (control) qubit is prepared in the spatial basis and the two $\frac{1}{2}$ beamsplitters forms an interferometer around the $\frac{1}{3}$ beamspliter. The target and control qubit are mixed on the $\frac{1}{3}$ beamsplitter and if the

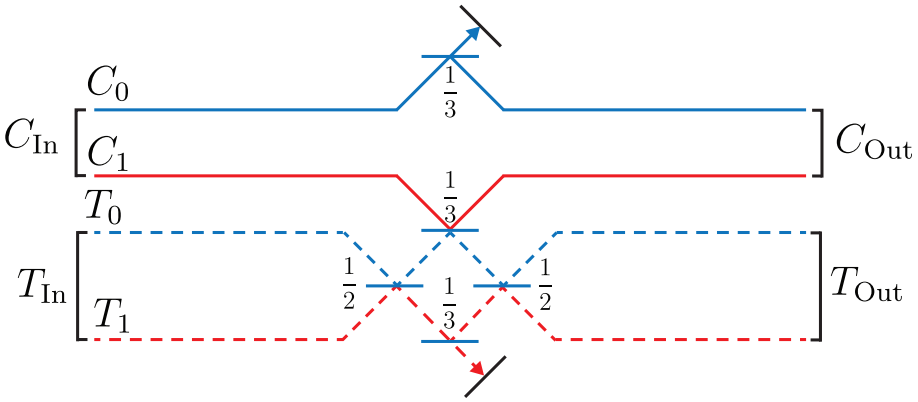

Figure 2.5: Schematic of the LOQC CNOT gate implemented by Ref. [50]. The target and control photon state is determined by their spatial mode, the control operation is performed by mixing the target and control photons on a $\frac{1}{3}$ beamsplitter. As the two $\frac{1}{2}$ beamsplitter acts as a interferometer the target state is unchanged if the control mode is empty.

control qubit is in $|0\rangle_c$ the interferometer causes no rotation to the target qubit, while if in the state $|1\rangle_c$ a phase shift is induced on the target qubit. By applying a Hadamard transformation onto the target qubit a spin-flip is achieved.

Due to the $\frac{1}{3}$ beamsplitter, the ideal success probability of the CNOT gate is $P_{\mathrm{CNOT}} = \frac{1}{9}$, which makes scalable integration challenging.

By integrating three LOQM CNOT gates, a LOQM Shor's factorizing algorithm was demonstrated [53]. Shor's factorizing algorithm is one of the most celebrated quantum algorithms, as it promises an exponential speed up of the intractable problem of prime factoring of numbers [54].

Computation using strong nonlinearities

The probabilistic nature of the gates makes LOQC unsuitable for scalable quantum information as near-unity gate fidelity is needed in order to cope with the exponential scaling of the multiple qubits and gate operations needed for practical quantum computing. In order to solve this issue a paradigm shift is necessary and deterministic quantum gates are needed. Deterministic gates with photons is challenging as the interaction between photons are weak. To implement a deterministic gate a strong non-linear material is needed and no known materials exhibit an optical nonlinearity of sufficient magnitude [55]. Instead of a bulk optical crystal, a two-level system interacting with an optical mode exhibits a nonlinearity distinguishing between a single-photon and two photons, which causes a π-phase shift. The nonlinearity occurs since the two-level system is saturated by a single-photon. A nonlinear phase shift has been demonstrated using atoms [56, 35] and a nonlinear transmission have been demonstrated using a QD in a photonic crystal waveguide [57]. A theoretical proposal for utilizing a two-level system to generate a deterministic CNOT gate is found in Ref. [58].

Cluster state

A promising alternative to LOQC is computation using entangled states called cluster states [59]. An array of entangled qubits has the ability to perform a universal set of quantum gates through detection of individual members of the cluster state. A cluster state consists of several physical qubits

that in combination represents a single computational qubit. Rotations of the computational qubit are performed by measurements of the physical qubits and the final value of the computational qubit is read-out through detection of a single physical qubit value. If the qubits are encoded in single-photon polarization the computation is implemented by waveplates and polarization discriminating single-photon detectors. Computation using cluster states greatly simplifies the process of quantum computation, but displace the experimental complexity to the generation of the cluster state.

The cascaded decay of the biexciton to the ground state of a QD produces polarization entangled photon pairs [60, 61], which are the fundamental cluster states.

Alternatively, using the three level λ-scheme found in a trion state of charged QD, cluster states of arbitrary length is generated by entangling the photon polarization with the electronic spin of the trion [62]. By continuously exciting the trion state, the length of the entangled state is increased.

Fusion gates are utilized to generate an enlarged cluster state by fusing two cluster state together [63]. The ability to herald on a successful or failed fusion attempt enables the reduction of overhead as cluster states are reused in the event of a failed fusion.

Quantum chemistry

The computational challenges in simulating quantum effects on classical computers is also present in the field of chemistry. The molecules of interest are governed by Schrödinger's equation, but the complexity of the wavefunctions quickly renders the problem intractable for classical computers.

Quantum simulation is the underlying principle for quantum chemistry, as the objective is to generate a well-controlled system with a Hamiltonian that reproduces the system of interest. The evolution of the well-controlled system is then the basis of the computation.

A simulation of the molecular energy of a hydrogen molecule was performed in an optical quantum simulator [64]. The computation was performed by utilizing a phase-estimation algorithm, where the energy eigenvalue of the system is found by operating the Hamiltonian on an eigenstate of the system [65]. The evolution of the eigenstate is determined by the eigenenergy and is equal to an accumulation of phase over time. By estimating the phase that accumulated the energy of the state is determined.

A pair of indistigushable single-photons, which were produced using SPDC, served as the photonic qubits. Using linear optical components the qubits was interfered and by measuring the polarization of the target qubit the binary phase was estimated. From the phase estimation the energy of the eigenstate of the hydrogen molecule was determined at a high precision.

Boson sampling is also applicable in the context of quantum chemistry. Boson sampling probes the outcome statistics of the nonclassical interference of bosons, e.g. indistigushable photons, which scales exponentially when solved classical [66, 67]. Boson sampling can be thought as a quantum simulation of the system unitary. As the fabrication of optical chips has improved, it should be possible to impose any desired unitary transformation in a chip for boson sampling. With well-defined unitary transformation, boson sampling can be used to calculate the vibrational spectrum of molecules. A theoretical proposal to use boson sampling with squeezed vacuum states have shown to be able to model Franck-Condon factors in Formic acid and thymine [68]. While the input states for these applications are not single-photons, it shows the potential of optical quantum computers in chemistry.

Chapter 3

Cavity Quantum Electrodynamics

Optical cavities with semiconductor QDs are an attractive platform for studying light-matter interaction. A QD coupled to a photonic crystal cavity was used to demonstrate strong coupling and single-photon Rabi splitting [69, 70]. This system is quite intricate as it contains both a nanoscale quantum emitter that can violate the dipole approximation [71, 72] and a photonic crystal cavity with a rapidly varying spatial polarization.

Often theorists have turned to the Jaynes-Cummings model to describe the interaction of the QD with the cavity. The Jaynes-Cummings model accurately captures many of the effects measured in the QD-cavity system and is successfully applied to such systems in making predictions on the system behavior.

In this chapter, the Jaynes-Cummings model is reviewed in the context of a QD embedded in a photonic crystal cavity. It is also shown why a QD in a photonic crystal cavity cannot always be approximated as a two-level emitter. Using realistic parameters it is found that the inclusion of a multi-level emitter modifies the behavior of the system quantities. These findings have direct implications for current experimental applications [73, 74, 75, 76].

It is demonstrate that the complicated local polarization causes the orthogonal dipoles of emitter to couple radiatively and build up a mutual coherence. It is demonstrated that the mutual coherence causes interference between the QD's decay path leading to the formation of mutual long-lived state.

It is shown that the formation of a long-lived mutual state significantly modifies the coherence of the single-photons emitted.

This work was a collaboration with Kristian Høgh Madsen and is presented in Ref. [77].

3.1 Single-emitter cavity QED

The simplest quantum optical system imaginable is a two-level system interacting with a single electrical field, which is the situation considered in the Jaynes-Cummnings model[78]. This simple system reveals some remarkable dynamics such as coherent population oscillations and formation of quasi-particles.

The two-level emitter consists of an excited state $|e\rangle$ and a ground state $|g\rangle$. When in the excited state the system decays to the ground state by spontaneously emitting a photon into the optical mode, while the absorption of a photon from the optical mode leads to an excitation from the ground state

to the excited state.

In the following the Hamiltonian describing this dynamic is introduced and the remarkable results of the Jaynes-Cummings model is derived in an ideal system, while the behavior of this model is studied when dissipation is included.

The Jaynes-Cummings model

The Jaynes-Cummings model [78] is the full quantum-mechanical description of a two-level emitter interacting with an optical mode. It includes a quantized electric field, which before the development of the Jaynes-Cummings model was described classically in the Rabi model [79]. The Jaynes-Cummings Hamiltonian takes the form in the rotating wave approximation:

$$H = \hbar\omega_c \hat{a}^\dagger \hat{a} + \hbar\omega_0 \hat{\sigma}_+ \hat{\sigma}_- + \hbar g \hat{\sigma}_+ \hat{a} + \hbar g^* \hat{\sigma}_- \hat{a}^\dagger. \tag{3.1}$$

Here, the frequency of the optical mode is denoted by ω_c, and $\hat{a}^\dagger$ ($\hat{a}$) is the creation (annihilation) operator of an excitation in the optical mode. The emitter has an eigenfrequency ω_0, and $\hat{\sigma}_+$ ($\hat{\sigma}_-$) takes the emitter from the ground (excited) to the excited (ground) state. Finally the strength of the interaction between the two-level system and the optical field is given by g. The Jaynes-Cummings model can be recast in a frame rotating at ω_c:

$$H = \hbar\Delta \hat{\sigma}_+ \hat{\sigma}_- + \hbar g \hat{\sigma}_+ \hat{a} + \hbar g^* \hat{\sigma}_- \hat{a}^\dagger. \tag{3.2}$$

Here, the detuning between the emitter and the optical mode is $\Delta = \omega_0 - \omega_c$. At zero detuning, $\Delta = 0$, the solution to the Jaynes-Cummings model reveals two polaritons that are split by the Rabi frequency $\Omega = \sqrt{g^2(n+1)}$. Even at $n = 0$ the two states are not degenerate. The Jaynes-Cummings model predicts that there is a reversible population transfer between the two polariton states at the Rabi frequency.

Modeling dissipation

The Jaynes-Cummings model describes an ideal system with no loss or decoherence. In a real system, there are various processes that cause deviations from the Jaynes-Cummings model. In order to describe these processes the density matrix formalism is used. The density matrix of the system, $\rho_{\mathrm{S}}(t_0) = |\Psi_{\mathrm{S}}(t_0)\rangle\langle\Psi_{\mathrm{S}}(t_0)|$, is coupled to a reservoir, $\rho_{\mathrm{R}}(H_{\mathrm{R}})$, where the system can dissipate its energy. The system and the reservoir forms the total system density matrix $\rho_{\mathrm{SR}}(t)$:

$$\rho_{\mathrm{SR}}(t) = \rho_{\mathrm{S}}(t) \otimes \rho_{\mathrm{R}}(t) \tag{3.3}$$

The time evolution of the composite system can then be determined using the Schrödinger equation:

$$i\hbar\dot{\rho}_{\mathrm{SR}}(t) = [H, \rho_{\mathrm{SR}}(t)]. \tag{3.4}$$

Depending on the nature of the reservoir, it might not be possible to solve the problem. Since the state of the reservoir is not of interest, the complexity of the problem is reduced by ignoring the evolution of the reservoir and focus on the evolution of the system. Assuming that the reservoir is Markovian, the Lindblad formalism is utilized to describe the evolution of the system under the influence of the dissipation processes [80]. The Lindblad operator has the form $\mathcal{L}(\Gamma, \hat{R}) = \Gamma(\hat{R}\rho\hat{R}^\dagger - \frac{1}{2}\hat{R}^\dagger\hat{R}^\dagger\rho - \frac{1}{2}\rho\hat{R}^\dagger\hat{R})$,

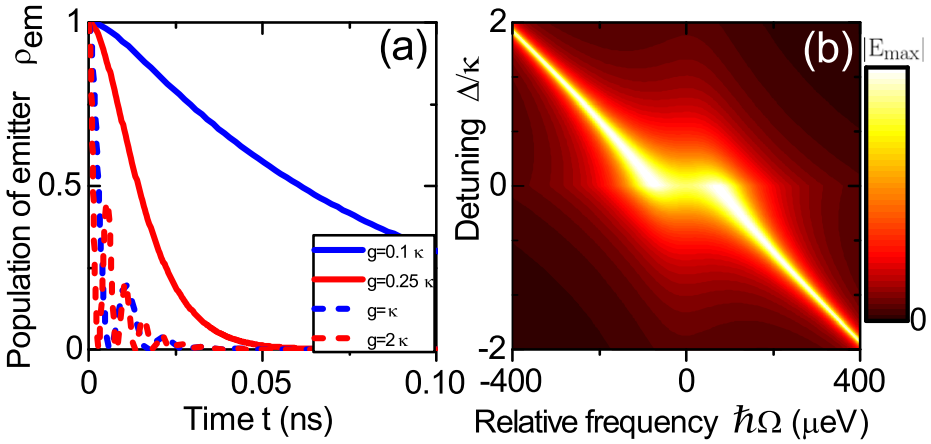

Figure 3.1: **a)** Dynamics of the population of the emitter for various coupling strengths and zero detuning $\Delta = 0$. As the coupling strength increases the exponential decay becomes faster. When the strong coupling regime is reached the decay becomes reversible with damped Rabi oscillations. **b)** Cavity spectrum for $g = \kappa$ and various detuning. As the emitter is tuned into resonance with the cavity, the linewidth of the emitter is broadened by the cavity. When the emitter and cavity is on resonance the avoided crossing is a signature of strong coupling.

where Γ is the rate of dissipation and $\hat{R}$ is the system operator which is affected by the dissipation process.

In the case of an emitter coupled to a cavity, there are two dissipation processes the cavity loss rate κ caused by mirrors with less than unity reflection, and the emitter dissipation γ caused by coupling to other optical modes. The corresponding Lindblad operators are $\mathcal{L}(\kappa, \hat{a})$ and $\mathcal{L}(\gamma, \hat{\sigma}_-)$. Finally, the pure dephasing rate γ_{dp} describes a loss of coherence in the system without dissipation. This process is described by the operator $\mathcal{L}(\gamma_{\mathrm{dp}}, \hat{\sigma}_z)$, where $\hat{\sigma}_z$ is the atomic inversion operator $\hat{\sigma}_z = [\hat{\sigma}_+, \hat{\sigma}_-]$. The time evolution for the reduced density matrix is [81]:

$$\dot{\rho}_{\mathrm{S}}(t) = -i\hbar^{-1}[H, \rho_{\mathrm{S}}(t)] + \mathcal{L}(\kappa, \hat{a}) + \mathcal{L}(\gamma, \hat{\sigma_-}) + \mathcal{L}(\gamma_{\mathrm{dp}}, \hat{\sigma_z}). \tag{3.5}$$

The temporal evolution of the emitter population $\rho_{\mathrm{Em}}(t)$ is solved using realistic parameters: $\hbar\kappa = 198\,\mu\mathrm{eV}$, $\hbar\gamma = 0.2\,\mu\mathrm{eV}$, $\hbar\gamma_{\mathrm{dp}} = 0.1\,\mu\mathrm{eV}$ [82]. Assuming that the emitter is initially excited $\rho_{\mathrm{Em}}(0) = 1$ and the cavity initially unoccupied $\rho_{\mathrm{cav}}(0) = 0$, the system is restricted to a single excitation, i.e. $\rho_{\mathrm{Em}}(t) + \rho_{\mathrm{cav}}(t) \leq 1$. These initial conditions mimic a QD in a cavity excited by a laser pulse.

In Fig. 3.1 (a), the temporal evolution of an initially excited emitter coupled to an optical cavity is shown. It is assumed that the emitter is on resonance with the cavity, $\Delta = 0$. If the coupling between the emitter and cavity is weak, $4|g| \ll |\kappa + \gamma|$, the decay follows an exponential dependence. As the coupling is increased, the decay rate is increased due to the Purcell effect [33]. If the coupling is sufficiently strong, $4|g| > |\kappa + \gamma|$, the decay of the emitter is reversible with Rabi oscillations in the population of the emitter. Increasing the coupling strength further results in an increase of the frequency of the population transfer.

The cavity spectrum as a function of frequency and detuning is shown in Fig. 3.1 (b). If the emitter is far detuned from the cavity, the emitter the emitter linewidth is given by γ and γ_{dp}. As the emitter is tuned into resonance with the cavity the linewidth of the emitter is broadened to the

linewidth of the cavity κ. Such a behavior also occurs in the weak coupling regime, as the emitter begins to couple to the cavity, it couples to the full linewidth of the cavity. As the cavity linewidth is much broader than the emitter this leads to a broadening of the emitter when observed through the cavity emission.

On resonance, the splitting in the spectrum is a signature of strong coupling between the emitter and the cavity. The avoided crossing is the Rabi splitting also observed in the ideal Jaynes-Cummings model. In this case the two polaritons are formed and they are split by the Rabi frequency $\Omega_R = \sqrt{4|g|^2 - |\gamma - \kappa|^2}$. The avoided crossing in the spectrum is a consequence of the Rabi oscillation in the temporal domain, but often the avoided crossing is observed without detecting Rabi oscillation in the population due to dissipation dampening the decay, before the revival of the emitter population is observed [70].

3.2 Quantum-dot as a multi-level emitter

The Jaynes-Cummings model assumes that the emitter is a two-level system, but a QD is a multilevel structure. Even when only the ground state exciton is considered, the exciton complex results in multiple levels.

The ground-state exciton consists of an electron with a projected angular momentum $J_z = \pm\frac{1}{2}$ and a hole with $J_z = \pm\frac{3}{2}$. The total angular momentum of the exciton is therefore either $J_z = \pm 1$ or $J_z = \pm 2$. The excitons with $J_z = \pm 1$ are bright and couple to the optical field.

The strain introduced in the sample during growth, breaks the symmetry of the QD, which causes the two bright states to mix and form new eigenstates of the QD [83]. The new eigenstates are linearly polarized with a $\pi/2$ phase difference, as the new eigenstates are positive and negative superpositions of the $|\pm 1\rangle$. The two linearly polarized dipoles are aligned along the [110] and the $[1\bar{1}0]$ crystalline axis of the host material, called the x- and the y-axis.

The two $J_z = \pm 2$ excitons are dark excitons and are split from the bright states by hundreds of μeV. The bright and dark excitons can couple through a spin-flip process of the electronic spin. The spin-flip coupling of the excitons is revealed through a biexponential decay of the exciton in a time-resolved experiment, where the fast (slow) rate are given by the decay of the bright (dark) exciton [84]. In the following discussion the dark state recombination is neglected due to the limited contribution to the radiative signal [84].

In the following it is shown how the intricate electric field of the photonic crystal cavity leads to a mixing of the polarization components, which makes it necessary to consider both bright states of the QD in the treatment of the dynamics of the system. The addition of the second dipole is treated in both weak and the strong coupling regime and the coherence of the emitted photons are examined.

Electric field of L3 cavity

Ignoring the second dipole is often justified by the fact, that it is orthogonal to the electric field of the optical cavity. In a photonic crystal cavity, the electric field is complicated and the assumption above is not justified. In figure 3.2 (b-d), the intensity profile of the M1 mode of an L3 cavity is shown. The normalized electric field in Fig. 3.2 (d) reflects a composition of both $|\mathrm{E_x}|^2$ and $|\mathrm{E_y}|^2$, this demonstrates that the local electric field polarization is strongly varying spatially. The strong

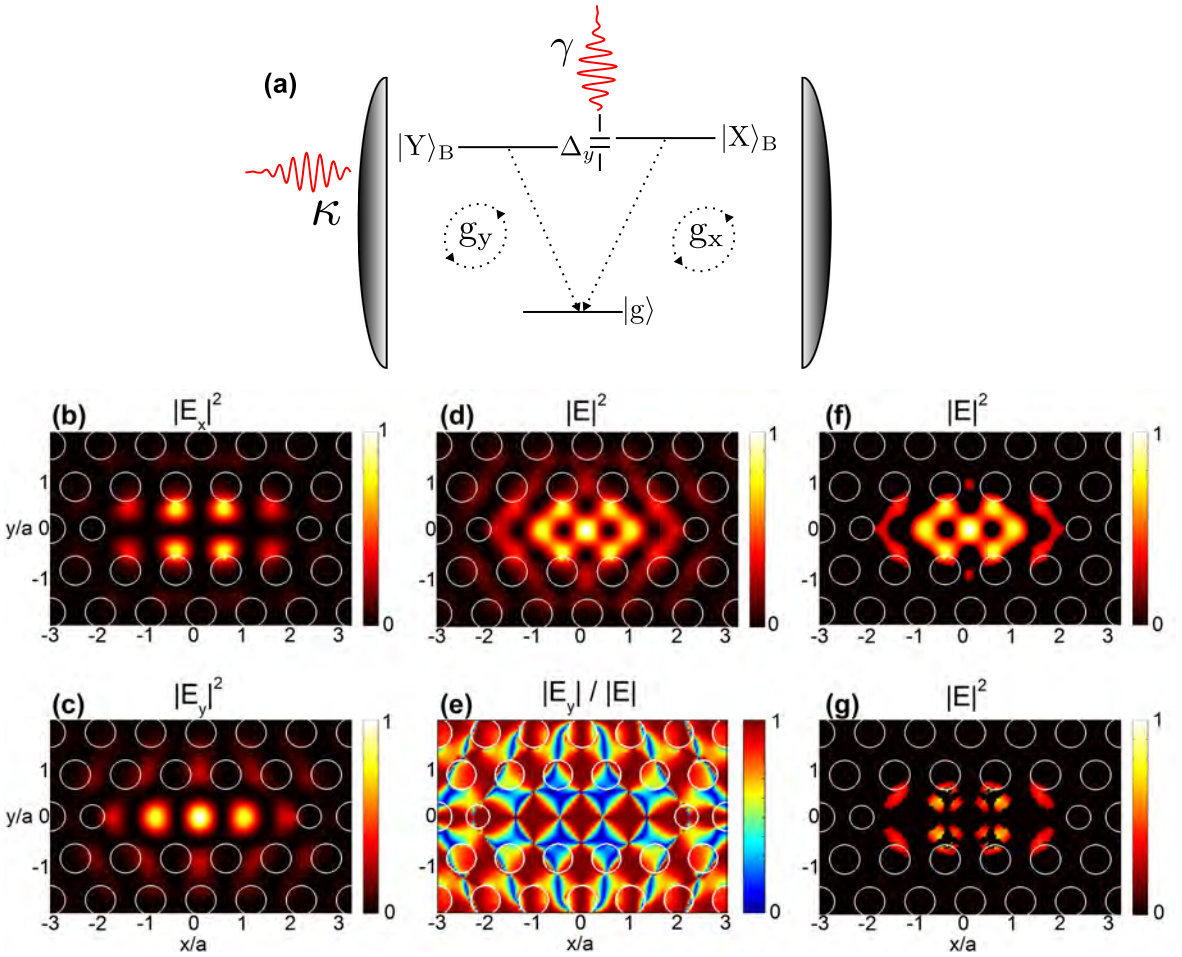

Figure 3.2: **a)** The three-level system is coupled to the cavity through g_x and g_y. The two excited states are coupled to radiation modes with the rate γ and the cavity loss rate is given by κ. The two excited states are split in energy by the fine-structure splitting Δ_y. Intensity profile of **b)** $|E_x|^2$ **c)** $|E_y|^2$ **d)** $|E|^2$ **e)** The direction of polarization, here 1 (0) corresponds to the y- (x-) polarization **f)** Intensity profile $|E|^2$ where $|E|^2 < 0.25\max(|E|^2)$ has been excluded corresponding to points of experimental significance **g)** Intensity profile where the intensity is of experimental significance and the field is off axis meaning $0.2 < |E_y|/|E| < 0.8$. The spatial coordinates x and y are scaled to the lattice constant a of the photonic crystal. All plots except (d) have units of V^2/m^2 and have been normalized to $\max(|E|^2)$

variation in the polarization of the electric field indicates, there are areas where the orthogonal dipole couples to the cavity mode.

Fig. 3.2 (e) shows the direction of the polarization inside the cavity, there are several spatial positions where the polarization of the field is completely aligned to the crystalline axes and causing one dipole to be coupled while the orthogonal is uncoupled. Fig. 3.2 (e) shows that there are intermediated positions where the polarization is "off-axis", the polarization is aligned to a superposition of the crystalline axes in these positions.

Fig. 3.2 (f) shows the area where $|E|^2 > 0.25\max(|E|^2)$, this is of importance as only areas with a reasonable electric field can obtain a coupling strength of experimental significance, the area where

this is fulfilled is $\mathrm{A}_1 = 3.057a^2$. Compared to the area of the normalized electric field $A_0 = 11.971a^2$, the area of experimental significant positions constitutes $\mathrm{A}_1/\mathrm{A}_0 = 25.5\%$ of the full mode profile.

Finally Fig. 3.2 (g) shows the area where the field is strong and is polarized considerably along both x and y $0.2 < |\mathrm{E_y}|/|\mathrm{E}| < 0.8$, with a corresponding area $\mathrm{A}_2 = 1.360a^2$. Comparing the two areas, i.e. $\mathrm{A}_2/\mathrm{A}_1 = 44.5\%$, suggest that the polarization is mixed for a large part of the cavity area of experimental significance. An investigation of the effect of a second dipole is therefore important.

Model for multi-level emitter

The system under investigation is depicted in Fig. 3.2 (a). The two bright states $|\mathrm{X}\rangle_\mathrm{B}$ and $|\mathrm{Y}\rangle_\mathrm{B}$ are polarized along the x-axis and y-axis, respectively. Both exciton states decay to the ground state $|\mathrm{g}\rangle$. The exciton states are coupled to an optical cavity with the coupling strength g_x and g_y, and detuned with respect to the cavity with Δ_x and Δ_y, respectively.

The excitons couple to optical modes other than the cavity mode, with the rate γ, which is assumed to be identical for the two dipoles. The cavity loss rate is again denoted as κ.

The possible states for the QD-cavity system are $|\mathrm{g},0\rangle$, $|\mathrm{X}\rangle_\mathrm{B} \equiv |\mathrm{X},0\rangle$, $|\mathrm{Y}\rangle_\mathrm{B} \equiv |\mathrm{Y},0\rangle$ and $|1\rangle \equiv |\mathrm{g},1\rangle$, where $|\mathrm{g},1\rangle$ is a single photon occupying the cavity. The second dipole is included in the model via the Hamiltonian $H_y = \hbar\Delta_\mathrm{y}\hat{\sigma}_\mathrm{yy} + \hbar(g_\mathrm{y}\hat{\sigma}_\mathrm{y1}a^\dagger + g_\mathrm{y}^*\hat{\sigma}_\mathrm{1y}a)$. The total Hamiltonian is:

$$\hat{H} = \hbar\Delta_\mathrm{x}\hat{\sigma}_\mathrm{xx} + \hbar\Delta_\mathrm{y}\hat{\sigma}_\mathrm{yy} + \hbar(g_\mathrm{x}\hat{\sigma}_\mathrm{x1} + g_\mathrm{x}^*\hat{\sigma}_\mathrm{1x}) + \hbar(g_\mathrm{y}\hat{\sigma}_\mathrm{y1} + g_\mathrm{y}^*\hat{\sigma}_\mathrm{1y}). \tag{3.6}$$

Here, the dipole operators are defined as $\hat{\sigma}_{ij} = |i\rangle\langle j|$. Lindblad operators are used to include dissipation as in the single dipole case: $\mathcal{L}(\kappa, \hat{\sigma}_{01})$ is the cavity loss, $\mathcal{L}(\gamma, \hat{\sigma}_{0\mathrm{x}})$ ($\mathcal{L}(\gamma, \hat{\sigma}_{0\mathrm{y}})$) is the loss due to coupling to radiation modes and the pure dephasing is included through $\mathcal{L}(2\gamma_\mathrm{dp}, \hat{\sigma}_{00} + \hat{\sigma}_{11})$. Decoherence is modeled as a dephasing process of the two bright states with respect to the ground state, but maintains the mutual coherence between the bright states. This assumption is based on experimental work suggesting that the mutual coherence between the bright states is preserved far beyond the radiative lifetime of the emitter [85].

The $\pi/2$ phase difference between the dipoles, induced by the strain, is included in the model as a relative phase between the coupling strengths.

The fact that both bright states can not be populated at the same time causes a divergence from the multiple emitter model proposed by Dicke [86]. This acts as a time-dependent interaction strength, where the transition from $|\mathrm{Y}\rangle_\mathrm{B} \rightarrow |1\rangle$ is inactive when $|\mathrm{X}\rangle_\mathrm{B}$ is occupied and vice versa.

As before non-resonant excitation is assumed and the two dipoles are therefore initially populated equally $\rho_\mathrm{x}(0) = \rho_\mathrm{y}(0) = \frac{1}{2}$. The initial state is therefore a mixed state and not a coherent superposition. This is important as it means, that there is no interference between the two decay paths at $t = 0$.

Weak coupling

We first study the case when both dipoles are in the weak coupling regime. The weak coupling regime is of experimental relevance in the efforts for constructing platforms for efficient single-photon technologies. In such single-photon experiments, polarization extinction is often used to suppress the scattered laser light. The detection polarization is matched to the far-field polarization of the cavity mode in order to enhance the detected signal.

If the far-field of the cavity mode is polarized along the x-axis, the state coupled to the cavity mode and thereby detected is $|\Psi_{\mathrm{coh}}\rangle = |\mathrm{X}\rangle_{\mathrm{B}} + \sqrt{\beta_{\mathrm{y}}}|\mathrm{Y}\rangle_{\mathrm{B}}$, which represents the coherent sum of the two dipoles, and includes interference between the fields. The fraction β_{y} of the second dipole $|\mathrm{Y}\rangle_{\mathrm{B}}$ has the far-field polarization of the cavity and is thereby coupled out through the polarizer and detected. The value β_{y} signifies the off-axis coupling between the second dipole and the local electric field.

The density matrix representing the coherent sum of the two dipoles $|\Psi_{\mathrm{coh}}\rangle$ is:

$$\rho_{\mathrm{coh}} = |\Psi_{\mathrm{coh}}\rangle\langle\Psi_{\mathrm{coh}}| = \rho_{\mathrm{x}} + \beta_{\mathrm{y}}\rho_{\mathrm{y}} + \sqrt{\beta_{\mathrm{y}}}(\rho_{\mathrm{xy}} + \rho_{\mathrm{yx}}) \tag{3.7}$$

As for the single emitter case, the population of the excited states decays exponentially with a rate given by the coupling strength to the cavity. The scenario is unchanged by the addition of a second dipole as the decay is irreversible in the weak coupling regime, the two states do not build up any coherence. The photon spontaneously emitted from one state is lost before it can excite the other state and no interference between the two states occurs and the system appears as two isolated two-level systems. As a result, the decay of the exciton is a bi-exponential with decay rates proportional to g_{x} and g_{y}, respectively.

In an experiment where the dark-exciton states are also present, the resulting decay is triple exponential. The rates of the bright excitons depend on the local photonic environment, by varying the detuning between the cavity and the excitonic state, the decay rate of the bright exciton changes while the decay of the dark excitons remains constant [84].

Strong coupling regime

In the strong coupling regime, the dynamics become more complex when including a second dipole because the decay of the dipoles interferes. If the two dipoles are in phase, the constructive interference causes an enhanced decay.

In Fig. 3.3 (a-c), the dynamics for several of the relevant system values are shown for three different coupling strengths of the y-dipole, here ρ_{x} (ρ_{y}) is the population of the x-(y-) dipole, $\rho_{\mathrm{x}}^{2-\mathrm{level}}$ ($\rho_{\mathrm{y}}^{2-\mathrm{level}}$) is the population of the x-(y-) dipole if a two-level system is assumed. Finally also the coherent sum ρ_{coh} is plotted, this is the emission from the dipoles that couples out through the cavity before being detected. The coherent sum ρ_{coh} depends on the interference between the two decay paths.

In Fig. 3.3 (a) only the x-dipole is strongly coupled to the cavity, while the y-dipole is in the weak-coupling regime, the dynamics of ρ_{x} (ρ_{y}) predictably resemble the 2-level decays. The coherent sum shows two Rabi oscillations before decaying with the background rate γ. If the coupling strength of the y-dipole is increased, the dynamics start deviating from the uncoupled case. As the coherence between the two dipoles is increased, a slowly decaying state is formed, which does not couple to the cavity and only decays through the radiation modes with the background rate γ. The coherent sum decays from unity to $\frac{1}{2}$, where a single oscillation occurs, and afterwards it decays with the background rate.

In Fig. 3.3 (d-f), the spectrum of the emission coupled through the cavity (called the cavity spectrum) and the emission leaking from the QD (called the QD spectrum) are shown. The Rabi frequency seen in the avoided crossing is given by:

$$\Omega_{\mathrm{R}} = \sqrt{4(|g_{\mathrm{x}}|^2 + |g_{\mathrm{y}}|^2) - (\kappa - \gamma)^2} \tag{3.8}$$

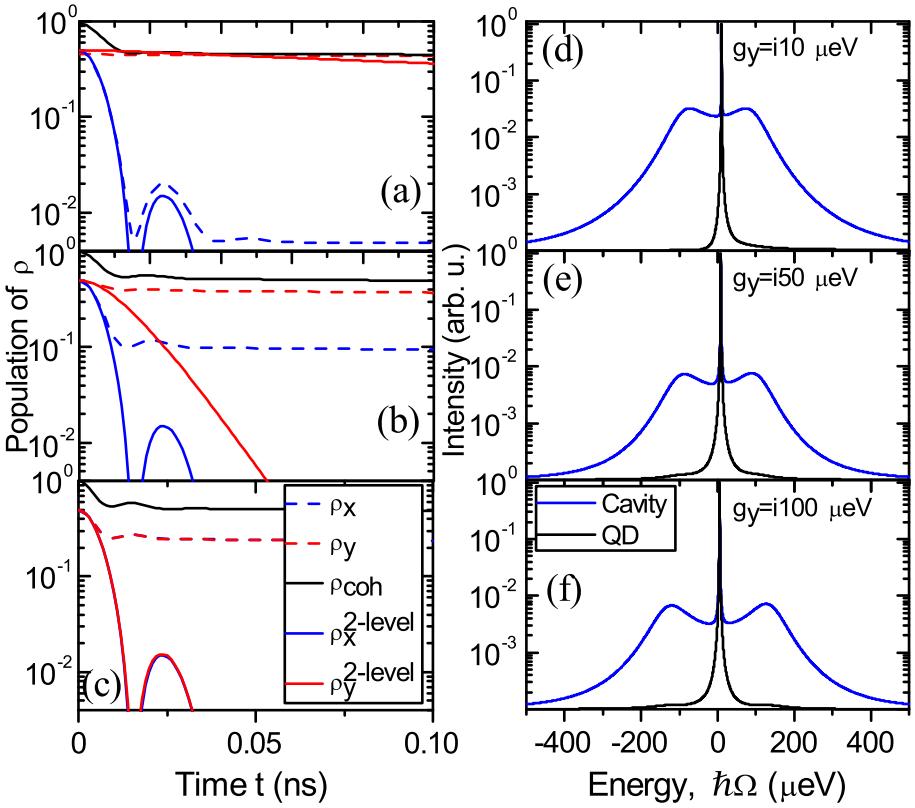

Figure 3.3: **a-c)** Dynamics of the x-dipole ρ_{x}, the y-dipole ρ_{y}, the coherent superposition ρ_{coh}, and the prediction of a two-level model with the same parameters $\rho_{\mathrm{x}}^{2-\mathrm{level}}$. The coupling of the x-dipole is $g_{\mathrm{x}} = 100\,\mu$eV y-dipole is **a)** $g_{\mathrm{y}} = 0.1ig_{\mathrm{x}}$ **b)** $g_{\mathrm{y}} = 0.5ig_{\mathrm{x}}$ **c)** $g_{\mathrm{y}} = ig_{\mathrm{x}}$. **d-f)** Cavity and QD spectra. When the y-dipole is weakly coupled the cavity spectrum shows the interaction between the x-dipole and the cavity. As the y-dipole begins to couple to the cavity the splitting increases as the Rabi frequency of the coupled emission is increased. The QD spectrum shows the slow decay of the inhibited emission decaying with the background rate γ.

This solution is very similar to the case of two independent emitters.

Since the QD emission in the QD-spectrum does not couple to the cavity, the only option for the emission is to leak out of the QD with the background rate γ. Since the slowly decaying state has an exponential decay rate, the QD spectrum has a Lorentzian lineshape.

In Fig. 3.4 (a-b), the decay rate γ_{coh} of ρ_{coh} is plotted as a function of the fine structure splitting (FFS), Δ_{y}, and the dephasing rate, γ_{dp}. In Fig. 3.4 (a) it is seen that as Δ_{y} is increased, the decay rate γ_{coh} increases quadratically at first and then linearly. The increase in γ_{coh} is due to a collapse of the slowly decaying state, since the interference between the two decay paths is reduced when the detuning is increased.

Fig. 3.4 (b) reveals that the decay rate γ_{coh} is almost independent of the dephasing rate γ_{dp}. It is quite interesting that the slowly decaying state is protected against dephasing subjected to the bright states. This is due to the mutual coherence between the two levels experiencing the same dephasing rate.

In the previous discussion the decoherence rate does not account for slow spectral diffusion of the

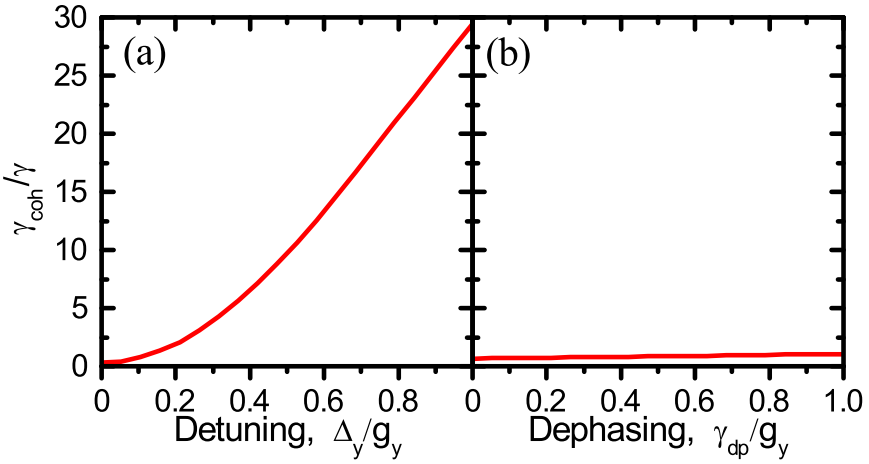

Figure 3.4: The decay rate of the coherent sum as a function of **a)** the detuning of the y-dipole Δ_y **b)** the dephasing rate γ_{dp}. As the detuning is increased the rate of the decay increases as the slowly decaying state collapses. The slowly decaying state is protected against dephasing as the mutual coherence between the bright states is preserved.

excitonic states. The spin noise induced by the Overhauser field of nearby nuclear spins occurs on time scales much longer than the exciton coherence time and is therefore not relevant for the discussion [28]. Instead this effect manifests as a time varying FFS between the two dipoles. Charge noise might have an influence on the timescale of the coherence time, but since the electronic spin couples weakly to the electric field, such effects are neglected [87]and spectral diffusion has no influence on the formation of the slowly-decaying state. A long-lived state that is protected against these dephasing processes therefore occurs naturally in such a V-scheme.

Coherence of emitted photons

A QD embedded in a photonic structure is a potential source of coherent single photons to be used as photonic qubits. We investigate how the single-photon indistinguishability is affected by the multi-level nature of the QD. The indistinguishability of a single two level system that is weakly coupled to a cavity is deduced from the coherence time T_2:

$$\frac{1}{T_2} = \frac{1}{2T_1} + \frac{1}{T_2^*} \tag{3.9}$$

Here, $T_1 = \frac{1}{\Gamma}$ is the radiative decay time, Γ is the decay rate of the emitter, and $T_2^* = \frac{1}{\gamma_{\mathrm{dp}}}$ is the dephasing time. The visibility of the photons is determined by the likeness to a transform limited photon $V = \frac{T_2}{2T_1}$, and the indistinguishability is [88]:

$$V = \frac{\Gamma}{\Gamma + 2\gamma_{\mathrm{dp}}} \tag{3.10}$$

The indistinguishability can be improved by enhancing the decay rate of the emitter through the Purcell effect. In the weak-coupling regime, the second dipole causes a reduction of the measured indistinguishability since the fine-structure splitting reduces the spectral overlap between the emitted photons. This is inferred from the fact that the V-system acts as two individual two-level systems in the weak-coupling regime.

In the following, the state $|\mathrm{X}\rangle_\mathrm{B}$ is assumed to be strongly coupled to the cavity and Eq. 3.10 does not apply as the interactions are non-Markovian. Instead, the theory presented in Ref. [27] is followed, as it is general and works for both weak and strong coupling regime. The derivation follows below.

The indistinguishability of a QD is measured by observing HOM bunching when two single-photons are interfered on a beamsplitter [89]. The photons interfered stem from the same QD emitted at different times and is conceptually equivalent to interfering two photons from different QDs. This assumption is the basis of the calculation of the indistinguishability. The unnormalized correlation function between the outputs labeled 3 and 4 of the beamsplitter is:

$$G_{34}(t,\tau) = \langle \hat{a}_3^\dagger(t)\hat{a}_4^\dagger(t+\tau)\hat{a}_4(t+\tau)\hat{a}_3(t)\rangle. \tag{3.11}$$

The operators of the outputs ports are related to the input operators through the unitary operator of the beamsplitter. If the beamsplitter is assumed balanced, the correlation function, as written in terms of the input operators, is:

$$\begin{aligned} G_{34}(t,\tau) = \frac{1}{4}\Big(\langle \hat{a}_2^\dagger(t)\hat{a}_1^\dagger(t+\tau)\hat{a}_1(t+\tau)\hat{a}_2(t)\rangle + \langle \hat{a}_1^\dagger(t)\hat{a}_2^\dagger(t+\tau)\hat{a}_2(t+\tau)\hat{a}_1(t)\rangle\Big) - \\ \langle \hat{a}_1^\dagger(t)\hat{a}_2^\dagger(t+\tau)\hat{a}_1(t+\tau)\hat{a}_2(t)\rangle - \langle \hat{a}_2^\dagger(t)\hat{a}_1^\dagger(t+\tau)\hat{a}_2(t+\tau)\hat{a}_1(t)\rangle. \end{aligned} \tag{3.12}$$

The input operators of the beamsplitter are related to the QD operator through a linear relationship $\hat{a}(t) = A(\mathbf{r})(\hat{\sigma}_\mathrm{gx}(t-\frac{\mathbf{r}}{c}) + \sqrt{\beta}\hat{\sigma}_\mathrm{gy}(t-\frac{\mathbf{r}}{c})) = A(\mathbf{r})\hat{\sigma}_\mathrm{Coh}(t-\frac{\mathbf{r}}{c})$ [90].

Using this transformation and assuming that the expectation values and coherence function of the emitters are identical, the unnormalized correlation function is rewritten to:

$$\tilde{G}_{34}^{(2)}(t,\tau) = \frac{1}{2}\Big(\langle \hat{\sigma}_\mathrm{Coh}^\dagger(t)\hat{\sigma}_\mathrm{Coh}(t)\rangle\langle \hat{\sigma}_\mathrm{Coh}^\dagger(t+\tau)\hat{\sigma}_\mathrm{Coh}(t+\tau)\rangle - |\tilde{G}^{(1)}(t,\tau)|^2\Big) \tag{3.13}$$

Here the propagation factor $A(\mathbf{r})$ is divided out for brevity and the unnormalized first order correlation function $\tilde{G}^{(1)}(t,\tau) = \langle \hat{\sigma}_\mathrm{Coh}^\dagger(t+\tau)\hat{\sigma}_\mathrm{Coh}(t)\rangle$ is introduced.

To normalize the correlation function under pulsed conditions the probability of coincidence is:

$$p_{34} = \frac{\int_{t=0}^{\infty}\int_{\tau,0}\tilde{G}_{34}^{(2)}(t,\tau)\mathrm{d}t\mathrm{d}\tau}{\int_{t=0}^{\infty}\int_{\tau,n}\tilde{G}_{34}^{(2)}(t,\tau)\mathrm{d}t\mathrm{d}\tau} \tag{3.14}$$

Here $\tau,0$ designates the short time limit and τ,n is the long time limit. In the long time limit $\tilde{G}^{(1)}(t,\tau)$ decays to zero and the expression is rewritten:

$$p_{34} = \frac{\int_{t=0}^{\infty}\int_{\tau}\tilde{G}_{34}^{(2)}(t,\tau)\mathrm{d}t\mathrm{d}\tau}{\int_{t=0}^{\infty}\int_{\tau}\langle \hat{\sigma}_\mathrm{Coh}^\dagger(t)\hat{\sigma}_\mathrm{Coh}(t)\rangle\langle \hat{\sigma}_\mathrm{Coh}^\dagger(t+\tau)\hat{\sigma}_\mathrm{Coh}(t+\tau)\rangle\mathrm{d}t\mathrm{d}\tau} \tag{3.15}$$

The indistinguishability is found from the correlation probabillity as $V = 1 - p_{34}$.

In Fig. 3.5 (a), the indistinguishability is plotted as a function of the FFS Δ_y, while $|\mathrm{X}\rangle_\mathrm{B}$ is on resonance with the cavity. At zero detuning the indistinguishability is $V = 0.2$, which might be surprising since the two dipoles are resonant with each other. The explanation for this behaviour is found in Fig. 3.4 (a). It is seen that at zero detuning the slowly decaying state dominates and the decay rate of the QD is given by the background decay rate γ. The slow decay of this state therefore makes it very susceptible to dephasing. As the detuning increases, the indistinguishability increases, which is

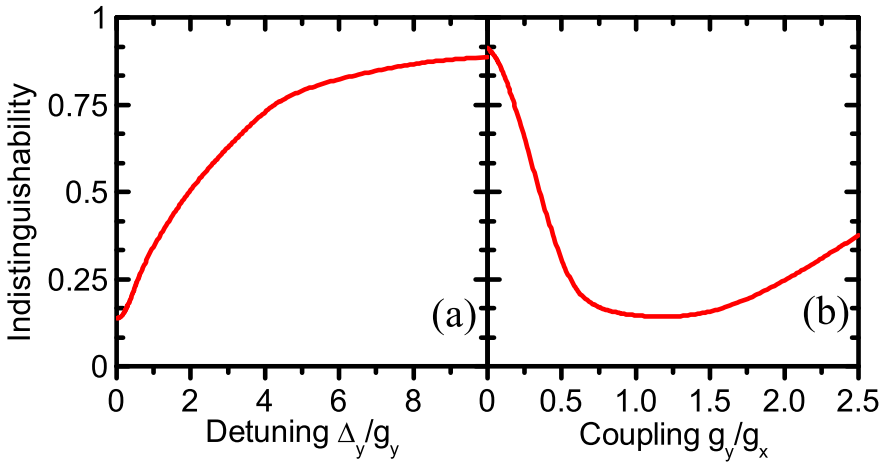

Figure 3.5: The indistinguishability as a function of **a)** the y-dipole detuning Δ_y **b)** the coupling strength of the second dipole g_y with $\Delta_y = 10\,\mu$eV. As the detuning is increased the rate of the decay increases as the slowly decaying state collapses. The slowly decaying state is protected against dephasing as the mutual coherence between the bright states is preserved.

due to the slowly decaying state breaking down and the decay rate increasing. It is interesting that the indistinguishability increases even though the spectral overlap between the two dipoles decreases. The improvement in indistinguishability is due to the slowly-decaying state collapsing, causing an increase in decay rate, this outweighs the reduction in indistinguishability caused by the spectral mismatch of the FFS.

Since the slowly decaying state is robust against dephasing, an increased dephasing would not contribute to an increased decay, but instead only cause a further reduction of the indistinguishability. After the slowly decaying state has collapsed, the indistinguishability is limited by the reduced spectral overlap between the two dipoles. If the second dipole is far detuned and no longer couples to the cavity mode, the indistinguishability rises asymptotically towards the single-dipole value.

Fig. 3.4 (b) shows the indistinguishability as a function of the coupling strength of the second dipole g_y, for $\Delta_y = 10\,\mu$eV. When the second dipole is uncoupled $g_y = 0$, the indistinguishability is at the single emitter value. As the second dipole starts coupling to the cavity, the indistinguishability decreases as both the slowly decaying state begins to form and the spectral mismatch lower the indistinguishability.

The indistinguishability reaches its lowest value when the two couplings are equal. If the coupling of the y-dipole is larger than that of the x-dipole, the slowly decaying state is destroyed again. The indistinguishability therefore begins to rise when the y-dipole is coupling stronger to the cavity than the x-dipole.

Resonant excitation

If the QD is excited resonantly instead of through the non-resonant cascade as previously, the scenario changes, as the QD is no longer initially in a statistically mixed state. Instead it is possible to prepare the QD in any superposition of the two dipoles, depending on the polarization of the laser at the position of the emitter. The local polarization of the excitation laser is closely related to the near-field

polarization of the cavity, as the laser intensity that does not couple to the cavity mode is rejected by the photonic band gap of the surrounding photonic crystal. This means that an arbitrary initial state is not possible and the state preparation is related to β_y.

If the QD is in a position where both dipoles couple significantly to the cavity mode, both dipoles are also excited at a comparable rate using a resonant laser pulse. The two dipoles are therefore excited to a coherent superposition state, which means that interference occurs between the two decay paths and the slowly decaying state forms at the first instance. It is no longer necessary for the dipoles to decay in order to build up the coherence.

If it is possible to excite the dipoles resonantly through other means than the cavity mode, e.g. through the radiation modes, it is possible to change the population ratio and potentially also the phase between the dipoles. By preparing the QD in the coherent superposition of $\frac{1}{\sqrt{2}}(|\mathrm{X}\rangle_\mathrm{B} - \mathrm{i}|\mathrm{Y}\rangle_\mathrm{B})$ the coherent superposition state $|\Psi_\mathrm{Coh}\rangle$ decays with an enhanced rate, as the decay path interferers constructively. It is thereby possible to generate long-lived or short-lived states on-demand.

Finally the shift to resonant excitation causes a reduction of the dephasing rate γ_dp as the dephasing introduced by the cascaded decay is no longer relevant [27]. Since the long-lived state is robust against dephasing, no qualitative change of the system behavior is expected.

3.3 Conclusion

In this chapter it was discussed how the Jaynes-Cummings model could be used to simulate a two-level system coupled to an optical cavity. Using realistic parameters for a QD in a photonic cavity the temporal behavior was explored in both the weak and the strong coupling regime. By considering the excitonic complexes of the QD and investigating the electric field profile of the photonic crystal cavity, it was shown that modeling the QD as a single two-level emitter is not adequate in all cases.

A theoretical model for including the orthogonal dipole of the QD was proposed and using realistic parameters the behavior was investigated in both regimes.

In the strong coupling regime it was found that by including the second dipole, a slowly decaying state is formed as a consequence of destructive interference between the decay paths of the two dipoles. This inhibited decay was seen to be robust against dephasing mechanism that preserves the mutual coherence between the dipoles.

When investigating the indistinguishability of the photons from the QD, it was found that the formation of an inhibited state made the coherence of the system susceptible to dephasing.

It was therefore determined that the coherence of two strongly coupled dipoles deviated from the single emitter case, when the slowly decaying state was formed.

Employing resonant excitation of the QD could open the possibility of preparing enhanced and inhibited states on demand, by preparing the QD in coherent superpositions. The multi-level structure of the QD thereby also facilitates the possibility of creating interesting decay dynamics.

Chapter 4

A single-photon source based on semiconductor quantum-dots

Scalable optical quantum computing requires efficient single-photon sources. Two main criteria must be fulfilled for sources in order to be applicable for quantum computing, a high single-photon purity, characterized by a suppressed $g^{(2)}(0)$ value, and a near unity indistinguishability of the emitted single-photons, measured by detecting two photon interference in a HOM interferometer.

An efficient source means that single-photons are created on-demand by a triggering event. As the source is on-demand, it is possible to interface it with other components at reliable timed events.

An efficient source enables scalable computation, which is not impaired by the exponential growth in susceptibility to inefficiencies. A near-unity efficiency enables computation to be scaled to larger complexity without being crippled by an unsurmountable integration time.

Solid-state QDs are excellent single photon emitters. By interfacing QDs with optical micro-pillars large outcoupling efficiency, single-photon emission and near transform-limited photons are achievable [37, 91, 92].

In this chapter two platforms with integrated solid-state QDs for efficient single photon generation are presented, one based on a photonic crystal cavity and one based on a photonic crystal waveguide. For both platforms QDs coupled to the system forms a single-photon emitter and the photon statistics are tested to demonstrate the single-photon nature of the source. For sources with high single-photon purity, the viability of utilizing these source as resources for photonic qubits is examined through HOM measurements.

4.1 Cavity based single-photon source

A potential candidate for an efficient single-photon source is a QD embedded in a photonic crystal cavity. This platform is attractive as the suppression of the QD's coupling to radiation modes enables near-unity couplings between QD and cavity mode.

Theoretical and experimental work suggest that the photonic crystal cavity can possess an optical mode demonstrating a high outcoupling efficiency [41].

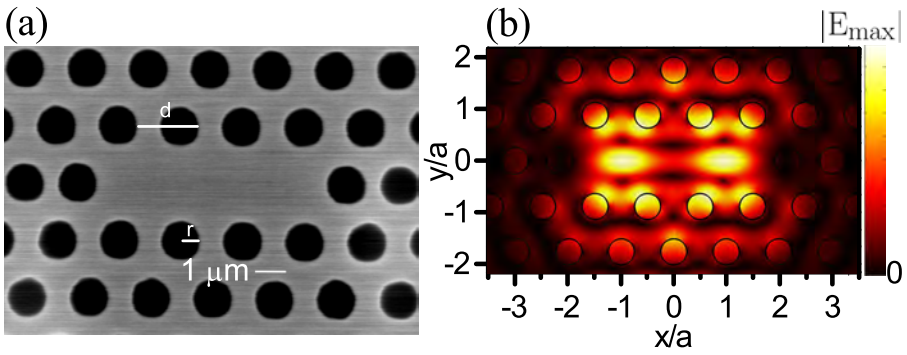

Figure 4.1: **a)** SEM image of the photonic crystal cavity. The cavity is formed by removing three holes from the perfect lattice, which induces optical states inside the band gap and enables strong confinement in-plane. The end holes of the cavity are displaced to reduce out of plane scattering. **b)** The electric field profile $|E|$ for the third order cavity mode. The electric field is predominantly confined to the optical cavity and is symmetric around the axis of the cavity. The anti-nodes of the cavity mode are localized in $(x, y) = (\pm a, 0)$.

A photonic crystal cavity

The structure of interest is a photonic crystal L3 cavity shown in the SEM in Fig. 4.1 (a). The cavity is formed by removing three holes from an otherwise perfect photonic crystal. The unperturbed photonic crystal is characterized by the lattice constant a, the hole radius r and the thickness of the membrane d. The confinement of light in the cavity is enhanced by shifting the position of the end holes of the cavity from the perfect lattice [93]. In the optimized structure the end holes on either side of the cavity are shifted by $0.175\,a$, $0.025\,a$ and $0.175\,a$ respectively, which significantly inhibits the cavity loss rate.

During the design process of the microcavity the properties of the QDs are considered to ensure an frequency overlap between the QD and the cavity.

The growth process of the QD is based on the Stranski-Krastenow method, where spontaneous island formation causing an inhomogeneous broadening of the emission frequency of the QD ensemble and the emission frequencies of the ensemble is expected to follow a Gaussian distribution [24]. The spatial density of the QDs determines if the cavity frequency is optimized for the center or the tail of the emission frequency distribution. If the spatial density is large it is advantageous to focus at the tail of the distribution to prevent several emission lines with similar frequencies from coupling to the cavity mode. Contrary, if the spatial density is low, the search is concentrated at the center frequency of the distribution as it is unlikely that more than a few QDs will be present within a single cavity.

The spatial density of the QDs is $\sim 10\,\mu\text{m}^{-1}$, the frequency distribution peak around 925 nm and the thickness of the membrane is $d = 160\,\text{nm}$. The cavity structure is therefore optimized so the third order mode is overlapped with the center of the distribution.

The mode profile is simulated by implementing a model of the photonic structure in a finite element method (FEM) solver and solving for the eigenmodes of the system. By modifying the photonic crystal parameters it is found that for a photonic crystal cavity with $a = 242\,\text{nm}$ and $r = 60\,\text{nm}$, the third order cavity mode is at $\lambda_{\text{M3}} = 923.6\,\text{nm}$. The electric field profile of the third order mode is shown in

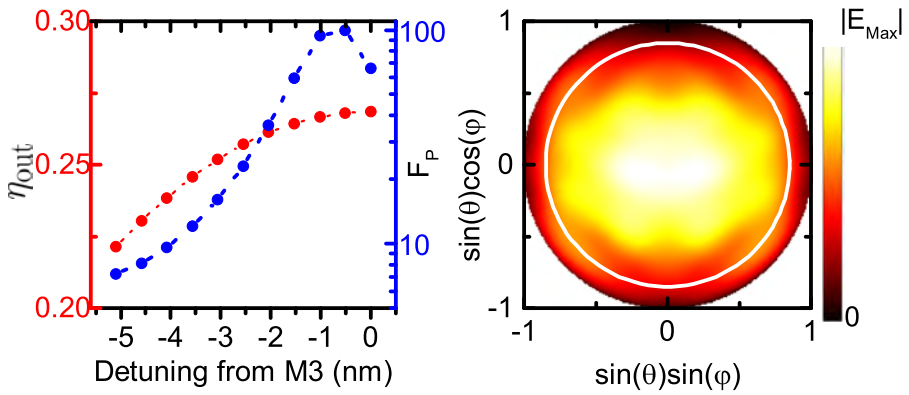

Figure 4.2: **a)** Outcoupling efficiency into the first lens η_{Out} and the Purcell enhancement F_{P} of a dipole in a L3 cavity. The dipole is positioned at the antinode of the electric field $(x, y) = (a, 0)$. By varying the detuning of the dipole from the third order cavity mode M3, the spectral dependence is investigated. Both F_{P} and η_{Out} decreases as the detuning is increased. **b)** The electric far-field pattern $|E|$ of a dipole at resonance with the M3 mode. The emission collected by a NA=0.85 objective is marked by the white circle.

Fig. 4.1 (b). The cavity modes are identified by their energy and electric field profile. The L3 cavity has six different optical modes, labeled M1-M6 from lowest to highest energy. The electric field is mainly inside the cavity and the third order mode has two anti-nodes located at $(x, y) = (\pm a, 0)$.

The radiation of a dipole inside the cavity is also simulated using the FEM solver and reveals the outcoupling pattern of the dipole, as well as the radiation rate. The outcoupling pattern of the dipole is modified by the optical structure it is embedded within. The far-field pattern of the dipole is of relevance, as it is used to calculate the fraction of the emission that is collected by a microscope objective. The outcoupling efficiency into the first lens is defined as $\eta_{\mathrm{Out}} = \frac{P_{\mathrm{Out}}}{P_{\mathrm{Total}}}$, where the collected power P_{Out} is dependent on the numerical aperture of the objective used. Fig. 4.2 (a) shows the outcoupling efficiency as a function of the detuning between the dipole and M3, where the dipole is placed at the antinode of the electric field $(x, y) = (a, 0)$. A numerical aperture of NA $= 0.85$ is assumed to match the numerical aperture of the microscope used in the optical setup. As the detuning is increased η_{Out} decreases slightly, but η_{Out} is quite broadband. Since the dipole is placed at the center of a membrane, half the emission is lost propagating away from the microscope objective, meaning that the efficiency is theoretically bound to $\eta_{\mathrm{Out}} < 0.5$.

Fig. 4.2 (b) shows the far-field pattern of a dipole at resonance with the M3 mode and located in the antinode of the electric field. The plot shows that a large fraction of the emission is located around the center of the objective. It is therefore possible to collect a $\eta_{\mathrm{Out}} = 26.8\%$ into a objective with NA $= 0.85$.

The numerical simulations are used to calculate the radiation rate of the emitter. The decay rate $\Gamma(\mathbf{r}_0, \omega, \mathbf{e_p})$ of an emitter is modified by the local density of optical states(LDOS) $\rho(\mathbf{r_0}, \omega, \mathbf{e_p})$ at the position of the emitter $\mathbf{r}_0$ [94]:

$$\Gamma(\mathbf{r}_0, \omega, \mathbf{e_p}) = \Gamma_{\mathrm{rad}}^{\mathrm{hom}}(\omega) \frac{\rho(\mathbf{r}_0, \omega, \mathbf{e_p})}{\rho_{\mathrm{hom}}(\omega)} + \Gamma_{\mathrm{nrad}}(\omega). \tag{4.1}$$

Here $\Gamma_{\mathrm{rad}}^{\mathrm{hom}}(\omega)$ is the decay rate of the QD in a homogeneous medium, $\rho_{\mathrm{hom}}(\omega)$ is the density of optical

states of a homogeneous medium and the non-radiative decay rate Γ_{nrad} describes processes that cause the loss of an excitation without producing photon. The quantum efficiency of the QD is defined as $\mathrm{QE} = \frac{\Gamma_{\mathrm{rad}}(\mathbf{r_0},\omega,\mathbf{e_p})}{\Gamma_{\mathrm{rad}}(\mathbf{r_0},\omega,\mathbf{e_p})+\Gamma_{\mathrm{nrad}}(\omega)}$. Lifetime meausrements shows that the quantum efficiency of InAs QDs is $\mathrm{QE} \sim 95\%$ [95].

The local density of optical states (LDOS) quantifies the number of optical states that an emitter can couple to, and is determined by the optical environment at the position of the emitter. If the LDOS is zero the emitter cannot radiate and the spontaneous emission of the emitter is inhibited. Whereas if the LDOS is greater than the density of optical states of a homogeneous medium, the decay rate is enhanced. An enhancement of the decay rate due to the environment is quantified by the Purcell factor [33]:

$$\mathrm{F_P} = \frac{\Gamma(\mathbf{r}_0, \omega, \mathbf{e_p})}{\Gamma^{\mathrm{hom}}(\omega)}. \tag{4.2}$$

Eq. (4.2) assumes the non-radiative rate is independent of the emitter being in a homogeneous medium or a patterned structure. The Purcell enhancement of an emitter in an optical cavity is given by the cavity quality factor, which is determined by the cavity loss rate $Q = \frac{\omega_c}{\kappa}$ and the cavity mode volume. The mode volume quantifies the spatial extent of the cavity's electric field. The Purcell enhancement of an emitter in an optical cavity is given by [96]:

$$F_P = \frac{3}{4\pi^2}\frac{Q}{V}\left(\frac{\lambda}{n}\right)^3 \frac{|\mathbf{d}\cdot\mathbf{f}(\mathbf{r}_0)|^2}{|\mathbf{d}|^2}. \tag{4.3}$$

Here Γ_{rad} is the radiative decay rate into optical modes other than the cavity mode and $\mathbf{d}$ is the dipole transition element of the emitter. Finally $\mathbf{f}(\mathbf{r_0})$ denotes the normalized electric field strength at the position of the emitter.

The Purcell factor determines the coupling efficiency of the emitter to the desired outcoupling mode. The efficiency of the coupling to the desired mode is the β-factor and is related to the Purcell factor through [37]:

$$\beta = \frac{\mathrm{F_P}}{1+\mathrm{F_P}} = \frac{\Gamma_{\mathrm{mode}}}{\Gamma_{\mathrm{mode}}+\Gamma_{\mathrm{rad}}+\Gamma_{\mathrm{nrad}}}. \tag{4.4}$$

Here Γ_{mode} is the radiative decay rate into the desired mode.

In Fig. 4.2 (a) the Purcell factor as function of the detuning between the emitter and the M3 mode is shown. The Purcell enhancement is $F_{\mathrm{P}} = 66$ at zero detuning and at $\Delta = 0.5\,\mathrm{nm}$ the Purcell factor is increased to $F_{\mathrm{P}} = 100$. As the detuning is further increased the enhancement is reducing until it reaches $F_{\mathrm{P}} = 7$ at $\Delta = 5\,\mathrm{nm}$. The findings here are consistent with the theoretical results of Ref. [41].

The brightness of the emitter into the objective of question is found as $\eta_{\mathrm{Out}}\beta$. It is noted that due to the definition of the β-factor, this expression also includes the quantum efficiency of the emitter.

The expression $\eta_{\mathrm{Out}}\beta$ only estimates the outcoupling brightness and does not include the incoupling to an optical fiber. If the optical setup following the microscope objective is consisting solely of free space optics, the mode shape is not of concern. Most practical application of a single-photon source requires coupling to and propagation in an optical fiber and the fiber incoupling efficiency cannot be ignored. The incoupling efficiency η_{Coup} is given by an overlap integral between the emission far-field pattern and the mode profile of the fiber [97]. The optical mode of a single mode fiber is a Gaussian mode and η_{Coup} is found as:

$$\eta_{\mathrm{Coup}} = \frac{|\int E^*_{\mathrm{Gaus}}(\mathbf{r})E_{\mathrm{Out}}(\mathbf{r})\mathrm{d}\mathbf{r}|^2}{\int|E_{\mathrm{Out}}(\mathbf{r})|^2\mathrm{d}\mathbf{r}|\int|E_{\mathrm{Gaus}}(\mathbf{r})|^2\mathrm{d}\mathbf{r}}. \tag{4.5}$$

The far-field calculated by the FEM solver does not contain phase information and the information required to calculate the overlap integral is not available. But from the far-field pattern in Fig. 4.2 (b) it appears that far-field pattern deviates significantly from a Gaussian profile. Some mode mismatch between the photoluminescence and a single-mode fiber is therefore expected.

Experimental setup

Sample preparation

A sample mask is prepared using the structure parameters extracted from the simulations. In order to account for variations in the fabrication procedure, multiple structures with parameters close to the optimized values are included in the sample mask design.

The designed mask is patterned on a wafer containing InAs QD using electron beam photo lithography. After the sample is patterned, the photonic structure is etched into the sample using an inductively coupled plasma etching process. The etching process also removes a sacrificial layer beneath the QD layer. The removal of the sacrificial layer means that the photonic structure is a membrane with the QD layer in the center.

To observe single-photon emission from the QD it is necessary to cool the sample to tens of K. The sample is therefore placed in a closed-cycled cryostat, that cools to a few K. The cryostat used is an AttoDry 500, which consists of a cryostat from Montana instruments fitted with nano precision piezoelectric stepping motors from AttoCube.

The piezoelectric elements have a single step resolution of $\sim 10\,\text{nm}$ which enables a high precision in the positioning of the membrane. A readout of the piezo resistance provides an absolute positioning feedback, which enables the system to revert back to a previous position without the need to relate the position to alignment markers. The precision of the resistive readout is limited to $\sim 200\,\text{nm}$ and is thereby limiting the possibility to use this mechanism to reproducible position the membrane at nanoscale precision.

Optical setup

To collect the photoluminescence from the QDs a confocal optical setup is built around the cryostat. The setup is shown in Fig. 4.3 (a), the confocal setup consists of two paths, one for excitation of the sample and one for the collection of the photoluminescence. The excitation laser is coupled out of the fiber and collimated to a 2 mm spot by an optical lens. The excitation laser is sent through a linear polarizer to ensure that the polarization of the light going to the sample is linear and stable. Even though the excitation laser light is propagated in a polarization maintaining fiber, polarization fluctuations are observed. The polarization rotations are manifested as power fluctuations when projected on the linear polarizer but are suppressed using an active power stabilization. The power stabilization consists of a photodiode(PD), which measures the intensity of the excitation beam after the polarizer and an acoustic optic modulator controlled by a PID loop, which keeps the measured intensity constant.

After the polarizer the beam is sent through a 90/10 beamsplitter, which transmits 90% while reflecting 10%. The reflected part of the excitation beam is sent towards the sample chamber, while the transmitted part is used to stabilize the PID device. An Olympus LCPLN100XIR microscope

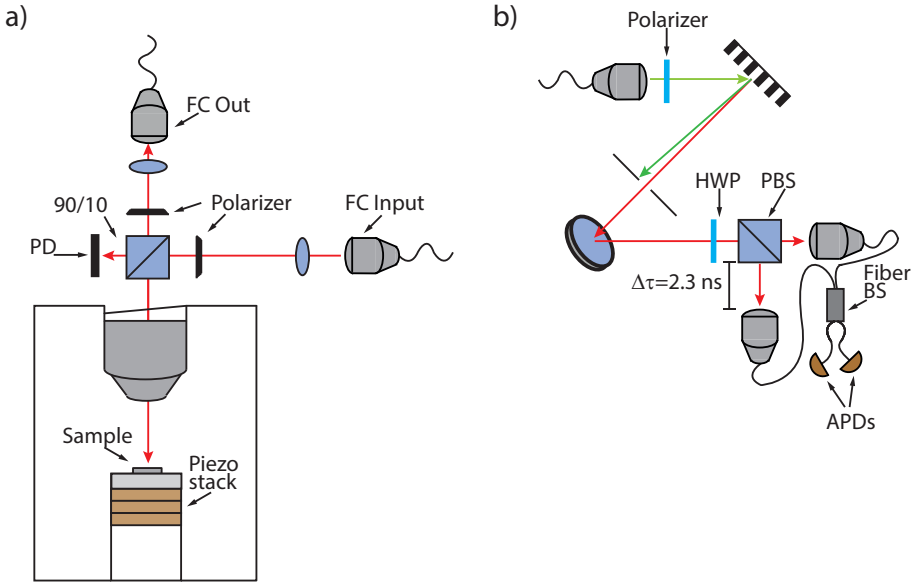

Figure 4.3: **a)** Schematic representation of the setup used for photoluminescence measurement of the QD in a photonic crystal cavity. The laser light used for excitation is coupled out of FC input, the light is collimated using a lens and sent through a linear polarizer. The polarized light is sent to a beamsplitter reflecting 10% of the light towards the sample space. A tilted vacuum window is placed above the microscope objective which focus the laser light onto the sample and collects the photoluminescence. The photoluminescence is sent through the beamsplitter where 90% is transmitted. A linear polarizer is used to suppress scattered laser light. Using a lens the photoluminescence is coupled into a single mode fiber. A PD measures the the transmitted intensity of the beamsplitter for the active power stabilization.**b)** Spectral filter setup of the photoluminescence. The collected emission is coupled out of the single mode fiber and sent through a polarizer. The emission is reflected off the grating, which separates the frequency components in different optical paths. A pinhole is used to block all unwanted frequencies and only transmit the desired frequency. A HWP in front of a PBS acts as a variable beamsplitter, which is used to change from HBT measurements to HOM measurement, by changing the beamsplitter from 100:0 to 50:50. A fiberbased beamsplitter is coupled to fibercoupled APDs for detection of the photon correlations.

objective is placed inside the vacuum chamber of the cryostat. The objective has a working distance of WD = 1.2 mm and numerical aperture of NA = 0.85. Due to the short working distance, the microscope has to be placed inside the chamber in order to bring the sample in focus. A benefit of having the objective inside the chamber is that the emission from the sample is collimated before being transmitted through the top window of the sample chamber. This ensures that aberrations due to the window are reduced.

The collected photoluminescence from the sample is sent to the 90/10 beamsplitter, where the transmitted part is sent through a polarizer that is orthogonal to the incoupling polarizer, causing a suppression of the scattered laser light. After the polarizer the emission is coupled into a single mode fiber, which is coupled to the detection setups.

Detection

The spectral properties of the photoluminescence is examined using an Andor Shamrock spectrometer. The spectrometer contains a grating with 150 l/mm for broadband measurements and a grating with 1200 l/mm for a higher spectral resolution. After the grating the emission is either sent towards a Andor Newton EMCCD to measure a spectrum or towards a slit that suppresses the unwanted emission, and the frequency of interest is detected by an Avalanche Photo Detector(APD) in order to investigate the temporal properties.

The single-photon properties of the photoluminescence are probed using the grating setup in Fig. 4.3 (b). The photoluminescence is coupled out of the single mode fiber and sent through a linear polarizer. The optical grating reflects the different frequency components of the photoluminescence at slightly different angles, making it possible to filter the desired frequency by having a pinhole blocking the undesired frequencies. The filtered emission is sent through a HWP and a PBS, which in combination constitutes a variable beamsplitter. Using the HWP and PBS as a variable beamsplitter renders it possible to switch between HBT and HOM measurement without any realignment. By setting the splitting ration to 100:0, the setup is primed for a HBT measurement, while setting the splitting ratio to 50:50 enables a HOM measurement. The linear polarizer is important as it ensures that the desired splitting ratio is maintained. During the integration time of a measurement, temperature change or stress along an optical fiber might cause rotations of the polarization. If the rotation of the outcoupled polarization occurs, the HWP in front of the PBS no longer causes a rotation into 50:50 or 100:0. By ensuring that the polarization is fixed, any rotation before the polarizer leads to a reduced intensity rather than an undesired splitting ratio. Maintaining the desired splitting ratio is particularly important for the HOM measurement, where a deviation from the desired 50:50 splitting ratio causes a distortion of the extracted indistinguishability.

After the PBS, the emission in each of the output arms is coupled into single mode fibers, with an induced path length difference of $\Delta\tau = 2.3\,\text{ns}$. The two arms are recombined in a fiberbased beamsplitter, which is highly beneficial in the context of HOM measurements as it ensures a perfect mode overlap between the two arms. The visibility of the interferometer when aligned is therefore approaching unity. As the transmitted and reflected part of the PBS is orthogonal in polarization this destroys any two photon interference. Using manual fiber polarization controllers, the polarization of the two arms is aligned. After the beamsplitter the emission is detected using fibercoupled APD from Perkin-Elmer.

Spectral investigation

The sample is cooled to 6 K and the photoluminescence of the sample is collected. By spatially aligning the excitation laser to the cavity, the photoluminescence from the QDs coupled to the cavity is collected and measured.

In Fig. 4.4 (a) the sample is excited above band gap $\lambda_{\text{laser}} = 800\,\text{nm}$ by a C. W. laser. The third order mode is located at 930 nm, while the fourth and fifth order mode is seen at 923 nm and 915 nm respectively. The spectrum shows that QD emission, which does not spectrally overlap with the cavity modes, is suppressed by the photonic band gap.

The spectrum shows the spectral structure of the third order mode is quite broadband, owing to a moderate Q-factor of $Q = 770$. Even though the Q-factor is moderate, a reasonable Purcell

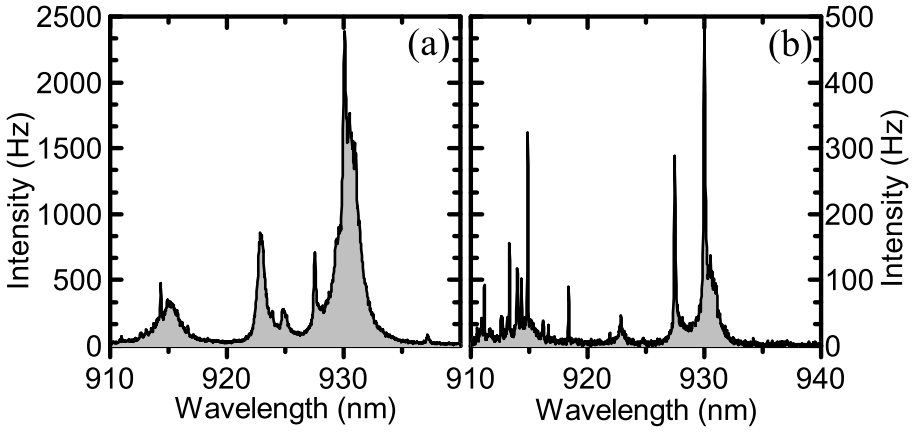

Figure 4.4: Emission spectra of QDs in a L3 cavity under C.W. excitation at $\lambda_{\text{laser}} = 800\,\text{nm}$. **a)** At high excitation power the third order cavity mode is visible at 930 nm. The fourth and fifth order mode are visible at 923 nm and 915 nm respectively. Overlapping with the broad emission of the cavity mode emission lines are seen at 928 nm and 931 nm. **b)** By reducing the excitation power the individual emission lines that are spatially and spectrally coupled with the modes are revealed. Several bright emission lines are observed and the most dominant line is spectrally overlapping with the third order mode.

enhancement is expected. The spectrum also reveals narrow emission lines overlapped with the cavity modes.

By reducing the excitation power individual emission lines are visible. As seen in Fig. 4.4 (b) the emission line at 930 nm is both bright and resonant with the third order mode, making this emission line interesting for further investigation.

The emission spectra in Fig. 4.4 (a) and (b) are both populated by several emission lines and such lines contribute negatively to the measurement of the single-photon purity. The issue is resolved by spectrally filtering away the unwanted emission lines or exciting the desired emission line through a resonance closer in energy to the emission line of interest.

During above band excitation, the excited carriers relax into the ensemble of QDs and causes a highly populated spectrum. When exciting a higher lying QD resonance, the carriers are trapped inside the specific QD. Through a cascaded decay the exciton relaxes to the ground state. When the exciton has decayed to the ground state, it recombines through the spontaneous emission of a photon. As only carriers inside the intended QD are excited, only emission from that QD is seen in the emission spectrum, making quasi-resonant excitation suitable for suppressing multi photon emission.

The emission frequency of the exciton ground state is likely to shift from above band excitation to quasi-resonant excitation. This effect is a consequence of the large number carriers excited during above band excitation, these carriers causes a screening of the built-in electric field of the sample. Since quasi-resonant excitation does not generate an abundance of carriers, the exciton line is expected to experience a red shift as a consequence of the missing screening potential [98].

By tuning the excitation laser frequency closer to the emission frequency of the QD line of interest a resonance for the QD is found. By exciting the sample at $\lambda_{\text{laser}} = 885\,\text{nm}$ it is possible to observe emission from the QD of interest. Fig. 4.5 shows the emission spectrum under excitation through the

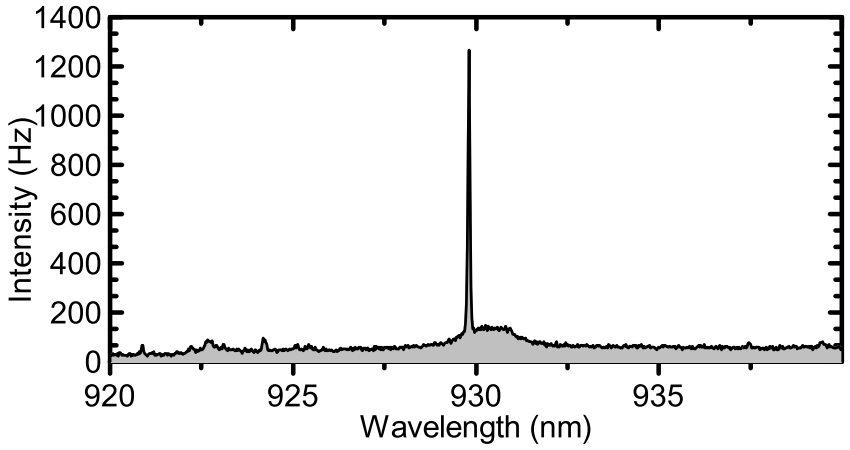

Figure 4.5: Photoluminescence spectrum of the emission line of interest excited through higher-lying resonance. The spectrum is dominated by a single emission line. There appears to be non negligible emission at the low energy side of the emission line.

$\lambda_{\text{laser}} = 885\,\text{nm}$. From the spectrum it is clear that exciting through the resonance has suppressed the emission from other QDs coupled to the cavity. As the excitation laser is detuned from the emission line by 45 nm it can not be characterized as a quasi-resonant excitation, but nonetheless the found resonance yields an improvement in the spectrum compared to above band excitation.

No higher-lying resonance is found by tuning the laser closer to the emission frequency of the QD ground state. The suppression of exciting through a resonance closer to the emission line might be caused by the photonic crystal band gap. The photonic crystal band gap suppresses the availability of optical states at the frequency of these quasi-resonant states. The coupling between the excitation laser and the emitter is therefore strongly inhibited. The likelihood of generating carriers in the quasi-resonant state is therefore very low and no emission is observed at the emission frequency of the exciton ground state.

As the introduction of the L3 cavity causes perturbation of the photonic band gap and introduces the cavity modes, there are available optical states inside the band gap. It is possible to excite through these quasi-resonant states. If the QD of interest has an excited state in resonance with a higher energy cavity mode, it is possible to excite the QD quasi-resonantly. Unfortunately the observation of a resonance through a higher-lying cavity mode is seldom, potentially hindered by the fact that not all the cavity modes are co-polarized.

When exciting through a higher-lying cavity mode, the excitation process is enhanced if the two cavity modes are co-polarized. Since the polarization of the laser determines the angular momentum of the created exciton, the polarization of the excitation laser determines, which of the two dipoles of the QD is excited. The local electric field of the laser light coupled to a cavity mode is strong and a dipole coupled to that cavity mode is excited efficiently. The structural axes of the fabricated cavities are aligned to the crystalline axis of the GaAs and thereby the dipole axes. One dipole is therefore more likely to couple efficiently to the cavity mode than the other dipole.

Unlike above band excitation, the initial population of the dipoles is therefore unequal. The decay from the excited state to the exciton ground state does not preserve the spin of the exciton, but spin-flips between the two bright states requires both the electron and the hole spin to flip reducing

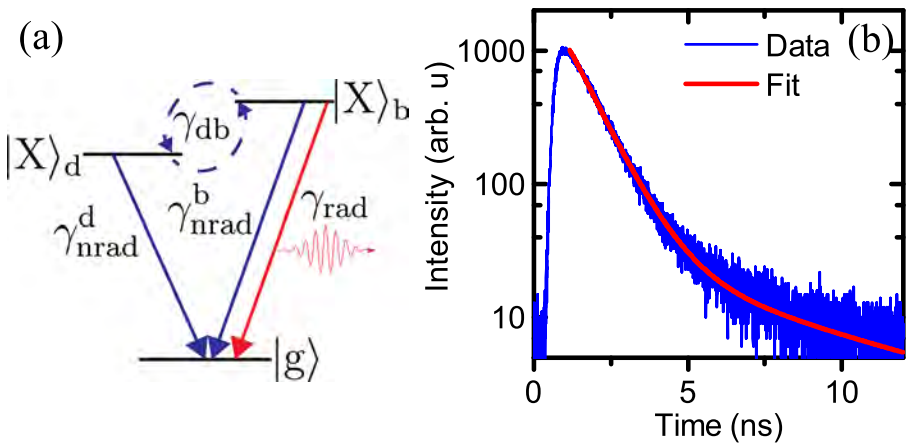

Figure 4.6: **a)** Three-level model of the QD. The bright exciton $|X\rangle_b$ couple radiatively to the ground state $|g\rangle$ with γ_{rad} and non-radiatively with γ^b_{nrad}. The dark exciton $|X\rangle_d$ couple to the ground state with the rate γ^d_{nrad}. The bright and the dark exciton couple through spin-flip processes with the rate γ_{db}. **b)** Life time measurement of the QD emission line with $\lambda_{laser} = 885\,nm$. The QD exhibits a bi-exponential decay with a fast rate $\gamma_{fast} = 1.114 \pm 0.006\,ns^{-1}$ and a slow rate $\gamma_{slow} = 0.180 \pm 0.007\,ns^{-1}$. The rates are extracted from a bi-exponential fit to the data.

the likelihood of it occurring.

Fig. 4.5 reveals a significant sideband at the low energy side of the emission line, which is a consequence of the exciton coupling to phonic states in the sample, as the QD is embedded in a solid-state matrix it experiences the lattice vibrations of the crystal. As the exciton is coupling to the phonon reservoir it can emit (absorb) a phonon when emitting a photon, thereby red (blue) shifting the emission frequency.

As the sideband in Fig. 4.5 is at the low energy side of the zero-phonon line, it is concluded that QD is predominantly emitting phonons. The asymmetry in the sideband is understood when considering the phonon density of states at $\sim 10\,K$ [29]. As the phonon occupation probability is related to the temperature of the host material, there are no available phonons for absorption at cryogenic temperatures. The phonon-assisted spontaneous emission therefore only occurs through the emission of both a phonon and a photon. The emission spectrum of the QD is therefore asymmetric towards the low energy side of the zero-phonon line.

Fig. 4.6 (a) shows the three-level model of the QD exciton. The bright exciton $|X\rangle_b$ couple radiatively to the ground state $|g\rangle$ through the rate γ_{rad} and non-radiatively with the rate γ^b_{nrad}. The dark exciton couple $|X\rangle_d$ to the ground state $|g\rangle$ with the rate γ^d_{nrad}. The bright exciton and the dark exciton couples through spin-flip processes with the rate γ_{db}. The population of the bright and dark exciton is found using rate equations for both levels. The population of the bright exciton $\rho_{bright}(t)$ is a bi-exponential decay [84]:

$$\rho_{bright}(t) = A_{fast} e^{-\gamma_{fast} t} + A_{slow} e^{-\gamma_{slow} t} \tag{4.6}$$

Assuming the two non-radiative rates are equal and the spin-flip rate is much smaller than the other rates $\gamma_{rad}, \gamma_{nrad} \gg \gamma_{db}$, the fast rate of the bi-exponential decay is given by $\gamma_{fast} = \gamma_{rad} + \gamma_{nrad}$, while the slow rate is $\gamma_{slow} = \gamma_{nrad}$.

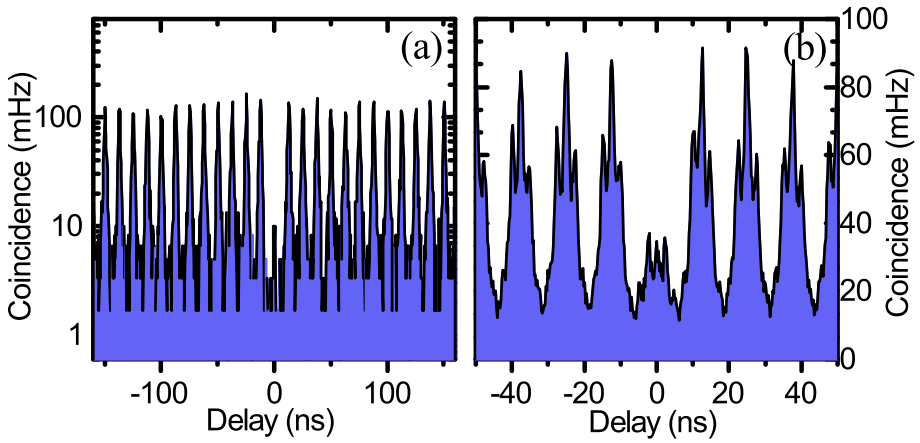

Figure 4.7: **a)** HBT measurement of the filtered emission at $P = 0.5P_0$ and $\lambda_{\text{laser}} = 885\,\text{nm}$. The antibunched emission demonstrates that the emission consists of single-photons. The extracted normalized second order correlation at zero time delay $g^{(2)}(0) = 0.06 \pm 0.026$ is significantly below the single-photon limit. **b)** HOM measurement of the filtered emission at $P = 0.5P_0$ and exciting through the resonance at $\lambda_{\text{laser}} = 885\,\text{nm}$. The five peaks at $\tau = 0$ are the correlated peaks of interest. By comparing the central correlated peak to the side peaks the visibility is extracted to $V = 0.03 \pm 0.003$.

Fig. 4.6 (b) shows the measured decay of the exciton line and the decay is bi-exponential. The decay is fitted using the bi-exponential model with the rates $\gamma_{\text{fast}} = 1.114 \pm 0.006\,\text{ns}^{-1}$ and $\gamma_{\text{slow}} = 0.180 \pm 0.007\,\text{ns}^{-1}$. From the extracted rates the radiative decay is found $\gamma_{\text{rad}} = \gamma_{\text{fast}} - \gamma_{\text{slow}} = 0.934 \pm 0.007$, which indicates the emission rate is not Purcell enhanced as this is comparable to the decay rate commonly found for QDs in unpatterned membranes [94, 99]. From the extracted rates the quantum efficiency is determined QE $= 83.8 \pm 0.008\%$, which is less than usually seen for InAs QDs [95].

Single-photon characteristics

To investigate the viability of embedded QDs as a single-photon source, the photons statistics of the photoluminescence is determined, using a HBT experiment. As discussed previously this experiment is able to determine if the source is emitting single-photons or not.

By exciting through the resonance at $\lambda_{\text{laser}} = 885\,\text{nm}$ and at half the saturation power, the second order correlation is measured and is shown in Fig. 4.7 (a). The second order correlation shows a strong suppression of $g^{(2)}(0)$ compared to the side peaks and the single-photon purity is extracted to $g^{(2)}(0) = 0.06 \pm 0.026$. Under these excitation conditions the detected single-photon rate is $\Gamma_{\text{det}} = 37 \pm 0.2\,\text{kHz}$.

The indistinguishability of two consecutive photons is tested using a HOM interferometer. A schematically depiction of the setup can be seen in Fig. 4.3 (b). After the emission is filtered by the grating it is sent through the HWP and the PBS. The HWP is set such that the emission is oriented 45° to the PBS, and the PBS therefore acts as a 50:50 beamsplitter. Using an optical delay path in the excitation optics it is possible to excite the QD twice per laser pulse. The separation between the two pulses is matched to the delay in the interferometer $\Delta\tau = 2.3\,\text{ns}$. If the first emitted

photon is propagating in the delay arm, while the second photon is propagating in the short arm, the temporal difference is removed and the photons will arrive at the second beamsplitter at the same time. If the photons are indistinguishable the Hong-Ou-Mandel effect causes the photons to bunch, causing no measured correlation between the output of the fiberbased beamsplitter. If the photons are distinguishable, there is no interference and correlations are observed.

The indistinguishability of the emitted photons are determined by the coherence time of the exciton and is defined as $T_2^{-1} = (2T_1)^{-1} + (T_2^*)^{-1}$ where T_1 is the exciton radiative lifetime and T_2^* is the pure dephasing time [100]. The pure dephasing time is a consequence of the decoherence processes experienced by the exciton, which occur on a variety of timescales from $\sim$ ps to $\sim$ ms [28]. By improving the radiative lifetime compared to the dephasing time, fourier transform limited photons are achieved when $\frac{T_2}{2T_1} \to 1$. Transform limited single-photons yield a perfect two photon interference in a HOM interferometer.

The decoherence processes are divided in two regimes, the decoherence mechanism that occur during the spontaneous emission process of the photon, and the processes that also occur while there is no exciton present in the QD. The decoherence occurring during the spontaneous emission event is an intrinsic dephasing process of the exciton, an example of such a decoherence process is the decay of the exciton from an excited state to the ground state under quasi-resonant excitation [27]. Under quasi-resonant excitation, the decay of the exciton from the excited state to the QD s-state is associated with a coherence loss, due to the induced timing jitter when decaying from the excited level. The phonon-assisted spontaneous emission, which gives rise to the phonon sidebands, is another pure dephasing process that causes loss of coherence during the spontaneous emission cycle.

In contrast to these fast decoherence processes there are also decoherence processes are occurring on timescales much longer than the lifetime of the exciton. These decoherence processes are manifested as spectral diffusion of the emission line, a slow spectral wandering of the emission energy that reduces the spectral overlap between photons emitted with a large delay and thereby reduces two photon interference [101, 91]. By measuring the indistinguishability as a function of the separation in emission time, the timescales of the relevant decoherence processes are characterized.

The two predominant sources of spectral diffusion in solid-state QDs are spin noise and charge noise. Decoherence due to spin noise occurs as a consequence of the nuclear spins of the GaAs host material. As these nuclear spin precess in time, the total magnetic field experienced by an electronic spin varies in time [102, 103]. The emission frequency of the exciton is perturbed, which over time manifests as spectral diffusion. The spin noise is relevant on time scales of $\sim \mu$s [28].

Another slow decoherence process is the charge noise, which is a consequence of variations in trapped charges in the vicinity of the QD [104, 105], causing a fluctuating electric field at the position of the QD. The varying electric field modifies the emission energy of the ground state exciton through the d.c. Stark shift. The relevant timescale of charge noise has been measured to be on the order of $\sim$ ms $-$ s. Charge noise is a result of the purity of the grown QD material [28]. By electrically gating the QD the effects of the charge noise can be reduce and near-transform limited photons are emitted under resonant excitation of the ground state exciton [92].

In Fig. 4.7 (b) the HOM measurement of the filtered emission of the QD when excited through the $\lambda_{\text{laser}} = 885\,\text{nm}$ resonance is shown. The region of interest is around $\tau = 0$, these five peaks are the so called correlated peaks, while the peaks at other delays are uncorrelated [106]. The peak at $\tau = 0$ is the correlation when the first emitted photon propagates in the delay path and the second photon in

the short path, this peak is affected by the indistinguishability of the photons. The peaks at $\tau = \pm\Delta\tau$ are the correlations where both photons are taking either the short path or the long path. Finally the peaks $\tau = \pm 2\Delta\tau$ arise from the first photon taking the short path and the second photon taking the long path. The expected ratio between the peaks are 1:2:2:2:1 for completely distinguishable photons and is determined by the probability of the individual photons taking the desired path through the interferometer versus the undesired [89].

A deviation from the peak structure of distinguishable photons therefore indicates some degree of two photon interference. By comparing the central peak to the side peak a visibility of $V = 0.03 \pm 0.003$ is extracted. This indicates the single-photons emitted are distinguishable. The non-resonant excitation scheme is likely causing the reduced visibility [27].

The phonon sideband seen in Fig. 4.5 is likely contributing to the reduced indistinguishability. The photon emitted into the phonon sideband contributes to a reduced spectral overlap. Even though the relative intensity of the phonon sideband is considerably lower than the intensity of the zero phonon line, the contribution is still significant as the frequency range of the sideband is broader [107]. Part of the phonon sideband is filtered, but the filter is too broadband to eliminate the full sideband. Detection of the phonon sideband lowers the two-photon interference, but does not affect the single-photon purity as the phonon sideband is emitted from the same QD.

Alternatively the orthogonal dipole of the QD might contribute to the detected emission and since the two dipoles are split by the fine structure splitting, the emission from the respective dipoles has a reduced spectral overlap.

The cavity based single-photon source demonstrates a high single-photon purity with count rates of tens of kHz. The lack of quasi-resonant excitation option limits the measured indistinguishability and makes the source unsuitable for quantum information processing.

4.2 Waveguide based single-photon source

An alternative platform for a single-photon source is a QD embedded in photonic crystal waveguide.

The photonic crystal waveguide is formed by leaving out a single or multiple rows of holes in an otherwise perfect crystal, which induces optical states inside the photonic band gap forming a propagating waveguide mode along the defect.

As the waveguide is formed in a photonic crystal the coupling to other modes is strongly suppressed, and an efficient light-matter interface is therefore created between the QD and the waveguide mode [42].

In addition to an efficient coupling interface, the emission is propagating inside the membrane making it suitable for integration with optical components, thereby circumventing outcoupling mechanism.

The ability to efficiently integrate single-photon sources with on-chip photonic components makes photonic crytal waveguides an attractive platform.

Photonic crystal waveguide

A SEM image of a W1 photonic crystal waveguide is shown in Fig. 4.8 (a). A row of air holes is left out of the perfect lattice thereby forming a waveguide.

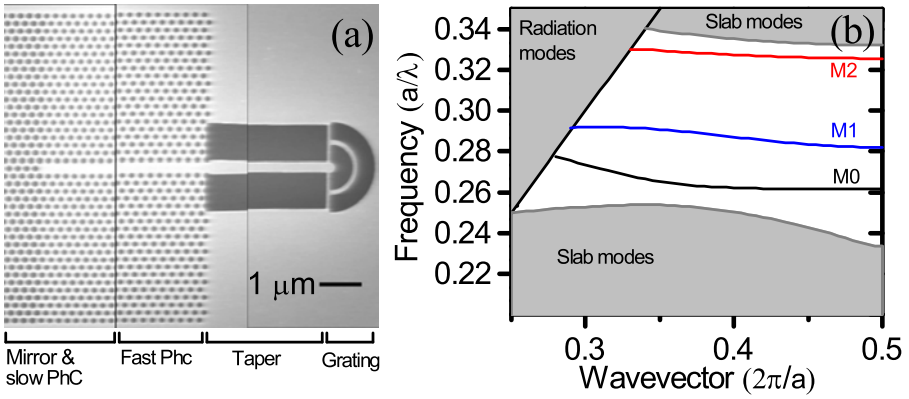

Figure 4.8: **a)** SEM image of the photonic crytal waveguide. The structure consists of two photonic waveguides with different lattice constants a, causing an offset in the band edge. The slow waveguide is terminated in a mirror to reflect the emission, the slow waveguide transitions to the fast waveguide, and the fast waveguide is coupled to an adiabatic tapered waveguide. The tapered waveguide is coupled to a second-order Bragg grating for outcoupling. The image is cut and stitched for size. **b)** The band structure for the photonic crystal waveguide. Inside the photonic band gap, illustrated by the white area, three waveguide modes are induced by the defect. Above the light line emission couple to radiation modes and the slab modes are confined to propagate in the membrane.

In Fig. 4.8 (b) the band diagram of such a photonic waveguide is shown, the photonic band gap is shown as the white region between the radiation modes and the slab modes. The radiation modes are modes that lie above the light line of the membrane, these are not confined by total internal reflection and therefore escape the membrane. On the other hand the slab modes are confined to the membrane by total internal reflection and the photonic crystal separates the slab modes into two bands. The waveguide induces three waveguide modes inside the photonic band gap, labeled M0-M2, where the fundamental mode of the waveguide M0 is the one of interest.

By embedding a QD in a waveguide structure the interaction between the QD and the waveguide enhances the spontaneous emission rate through the Purcell effect. In the case of the waveguide the Purcell enhancement is given by [108]:

$$F_P = \left(\frac{3\lambda^2 a}{4\pi n^3 V_{\text{eff}}} \right) n_g(\omega) \tag{4.7}$$

Here a is the lattice constant of the photonic crystal and V_{eff} is the effective mode volume of the waveguide mode. From this expression it is seen that the Purcell enhancement is proportional to the group index $n_g(\omega) = \frac{c}{v_g}$. The group velocity v_g is a concept from solid state physics and is given by the derivative of the dispersion relation. From the band diagram in Fig. 4.8 (b), the group velocity of the waveguide mode is expected to diverge, $n_g \to \infty$, when approaching the edge of the Brillouin zone. A strong enhancement of the Purcell factor is thereby expected and an efficient light matter interface attained.

Photonic structure

A sample with QDs embedded in photonic crystal waveguides is fabricated. The photonic crystal waveguide is seen in Fig. 4.8 (a). The structure is comprised of two photonic crystal waveguides with

different lattice constants a, which means their band edges are slightly offset. The offset of the band edges introduces a difference in group velocity between the two waveguides at the same wavelength. The slow waveguide has the band edge at the lower wavelength, which means that photons emitted at the band edge of this waveguide experiences an increased group velocity when transitioning to the other waveguide, which is designated the fast waveguide.

The slow waveguide is terminated in one end using a photonic mirror, the other end transitions to the fast waveguide, a transition region between the two waveguides reduces the transition losses. The fast waveguide is terminated in an adiabatic taper, which connects the waveguide with a Bragg grating.

Since n_g is diverging towards the wavelength of the band edge, the wavelength range close to the band edge is suitable for an efficient light-matter interface. Unfortunately, the large group index causes an increased scattering losses, due to fabrication imperfection and Anderson localization [109, 110, 111]. For this reason a photonic crystal waveguide is unsuitable for long length propagation of light close to the band edge and the slow waveguide is therefore coupled to a fast light waveguide. As the n_g at the wavelength of interest is lower, the scattering losses due to imperfections are reduced.

In order to excite the sample and collect the emission using the same objective, the emission is directed perpendicular out of the membrane by terminating the waveguide in a circular second-order Bragg grating, see Fig. 4.8 (a). The Bragg grating is based the constructive and destructive interference of the photons in the various scattering directions. The grating has a pitch of $\Lambda = \frac{\lambda_0}{2n_{\mathrm{GaAs}}}$, where λ_0 is the design wavelength in free space [112]. Such a outcoupling grating has a theoretical outcoupling efficiency of 40% over wavelength range of $890 - 920\,\mathrm{nm}$ into an objective with NA $= 0.65$ [113].

To reduce the losses in the transition from the photonic crystal waveguide to the second-order Bragg grating, an adiabatic taper is introduced [114], this is a dielectric waveguide where the width of the waveguide is reduced while obeying the adiabatic criteria [115]. By slowly reducing the width of the waveguide, the mode profile is expanded beyond the waveguide while the intensity remains in the fundamental waveguide mode. The separation of the outcoupling grating from the photonic crystal reduces distortion in the far-field pattern of the grating.

Experimental

The fabricated sample is mounted in a Liquid He bath cryostat from AttoCube. The sample is mounted on piezoelectric stepping motors that are placed in an optical dipstick, where a microscope objective is mounted inside the optical dipstick above the sample. The stick is placed inside the cryostat, where it is in thermic contact with the He, which maintains the sample at $\sim 4\,\mathrm{K}$.

An optical breadboard is mounted on top of the optical stick, where the optical setup for the confocal microscopy is mounted.

The QDs are excited using a Coherent Mira Ti:Sapphire laser pumped by a 9 W Verdi diode, which is operated either C.W. or mode-locked to generate ps pulses. The excitation laser is aligned to the photonic crystal waveguide, while the collection spot is aligned to the outcoupling grating. By translating the excitation spot along the waveguide it is possible to probe confined regions of the waveguide, while the collection spot remains stationary. This means that it is possible to find QDs coupled to the waveguide.

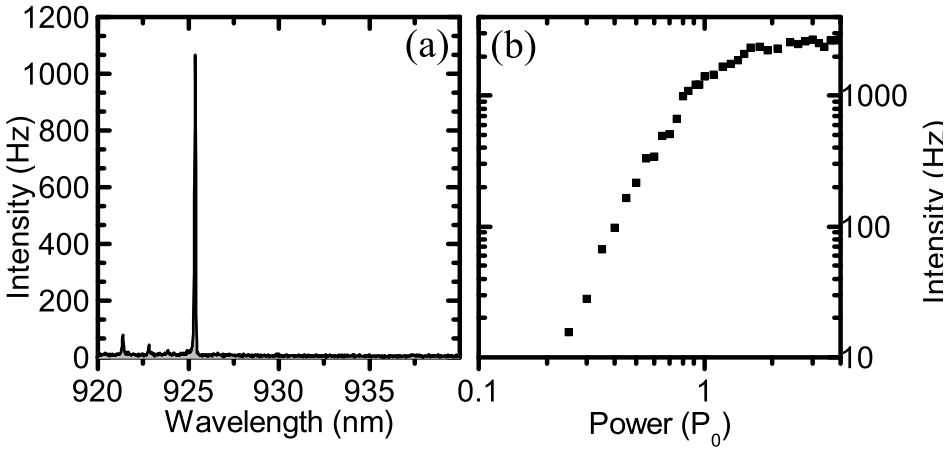

Figure 4.9: **a)** Emission spectrum from the outcoupling grating under pulsed excitation with $\lambda_{\text{laser}} = 913\,\text{nm}$. The spectrum is dominated by a bright emission line at 925 nm. Emission above 925 nm is completely suppressed by the photonic crystal band gap. **b)** The detected count rates on the CCD versus power. The power series is used to determine the saturation power P_0 of the emission line.

Photoluminescence

By tuning the wavelength of the excitation laser a strong p-shell resonance for a QD is found at 913 nm. In Fig. 4.9 (a) the spectrum under p-shell excitation is shown, where a dominant emission line at 925.5 nm and two weaker emission lines at 921 nm and 923 nm is seen. The spectrum around the bright emission line is not polluted by background emission and the line is therefore a prime candidate for further investigation.

The availability of a p-shell for excitation is likely due to the nature of the photonic waveguide. As the photonic waveguide increases the available optical states over a broad range of frequencies, it also induces optical states that overlap with the frequency of the p-shell resonance of a coupled QD. This has a dramatic impact on the likelihood of exciting the QD through a p-shell resonance.

In Fig. 4.9 (b) the detected emission as a function of excitation power is plotted, from which the saturation power P_0 of the emission line is extracted. The detected count rates grows exponentially until saturation power is reached.

Single-photon measurements

To probe the single-photon properties of the QD coupled to the photonic crystal waveguide, both measurements of the single-photon purity and the indistinguishability of the single-photons are performed.

In Fig. 4.10 (a) the second order correlation of the HBT measurement is shown. The measurement shows a strong suppression of the correlations at $\tau = 0$, the extracted normalized correlation is determined to $g^{(2)}(0) = 0.014 \pm 0.004$. The filtered emission is therefore concluded to contain little emission from other sources. Under these excitation conditions the detected count rates are $\Gamma_{\text{det}} = 38 \pm 0.2\,\text{kHz}$.

As the photon source exhibits a high single-photon purity, the indistinguishability of the emitted single-photons is tested. The QD is excited through the p-shell at $\frac{1}{2}P_0$ and the filtered emission is

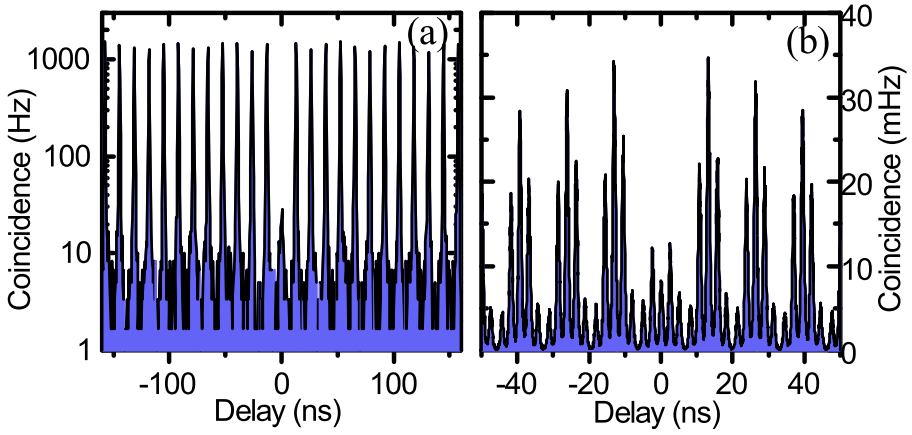

Figure 4.10: **a)** The second order correlation after HBT measurement of the filtered emission from the QD at $P = 0.5P_0$ with $\lambda_{\text{laser}} = 913\,\text{nm}$. At $\tau = 0\,\text{ns}$ the correlation is strongly suppressed to $g^{(2)}(0) = 0.014 \pm 0.004$. The suppressed $g^{(2)}(0)$ demonstrates that the photons emitted are single-photons. **b)** The second order correlation after HOM measurement of the filtered emission. The reduction of the peak at $\tau = 0\,\text{ns}$ compared to the peaks at $\tau = \pm 2\,\text{ns}$ indicates that two photon interference has occurred. The observation of interference shows that the photons have some degree of indistinguishability and is extracted to be $V = 0.32 \pm 0.02$.

sent through the fiberbased HOM interferometer. The second order correlation of the detected events is seen in Fig. 4.10 (b).

The central correlated peak is clearly reduced compared to the side peaks and the visibility is extracted to be $V = 0.32 \pm 0.024$, there is therefore some degree of two-photon interference, which promising for the use of the QD as a resource of indistinguishable single-photons. The observation of two-photon interference under quasi-resonant excitation is encouraging as the suppression of scattered laser light is a challenging aspect of resonant excitation of QDs [116]. Conversely, the indistinguishability is intrinsically limited in quasi-resonant excitation, owing to the dephasing process during the decay from the excited state to the exciton ground state.

Measurements of the same QD under similar conditions yielded a comparable extracted $V = 0.28 \pm 0.03$ and a radiative decay of $\Gamma = 4.32 \pm 0.15\,\text{ns}^{-1}$ was extracted [117]. From $V = \frac{\Gamma}{\Gamma + 2\gamma_{\text{dp}}}$, the dephasing rate was extracted $\gamma_{\text{dp}} = 5.85 \pm 0.8\,\text{ns}^{-1}$.

As the exact position of the QD is unknown and therefore the polarization of the local electric field too, it is not possible to determine the degree of mixing between the two dipoles of the QD. As the emission coupled to the photonic waveguide obtains the polarization of the waveguide, it is impossible to use polarization to separate the two dipoles. The fine structure splitting causes a spectral mismatch between the two dipoles reducing two-photon interference.

In order to probe the timescales of the decoherence processes, the two-photon interference is measured with the photons emitted $\sim 13\,\text{ns}$ apart. The double pulsing of the excitation laser is therefore no longer necessary and the optical delay is matched to the repetition time of the excitation laser, i.e. $\Delta\tau = \frac{n}{\Gamma_{\text{laser}}}, n \in \mathbb{R}_{>0}$. The excitation conditions are otherwise kept constant and the filtered emission is sent through the HOM interferometer with path length difference matching $\Delta\tau = \frac{1}{\Gamma_{\text{laser}}}$.

The resulting second order correlation is shown in Fig. 4.11. In contrast to the previous HOM

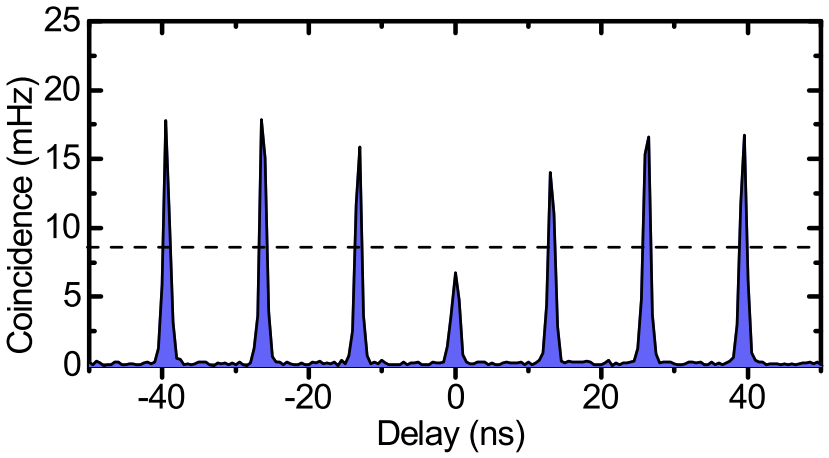

Figure 4.11: A HOM measurement with a path length difference of $\Delta\tau = \frac{1}{\Gamma_{\text{laser}}}$ of the photoluminescence, the visibility is extracted to $V_{13\,\text{ns}} = 0.24 \pm 0.06$. The expected coincidence counts for completely distinguishable photons are shown by the dashed line.

measurements there is a single correlated peak at $\tau = 0$. For distinguishable photons the expected relation between the peaks are 0.5 at $\tau = 0$ and 0.75 at $\tau = \pm\frac{n}{\Gamma_{\text{laser}}}$ of the remaining peaks [107, 101].

In Fig. 4.11 half of the average of the relevant side peaks are marked with the dashed line, showing the expected peak height of completely distinguishable photons. The correlated peak at $\tau = 0$ is clearly below this value and the extracted visibility is $V_{13\,\text{ns}} = 0.24 \pm 0.06$. This indicates that the photons are still indistinguishable to some extent at this timescale. A decrease in the HOM visibility on these time scales has also been observed under resonant excitation [118].

It is possible to reduce the decay in indistinguishability by electrically gating the QD, which suppresses charge noise by stabilizing the Fermi level of the QD [101].

As mentioned the side peaks at $\tau = \pm\frac{1}{\Gamma_{\text{laser}}}$ should be at $\frac{3}{4}$ compared to the other side peaks. From figure 4.11 it is not immediately clear that this is the case, even though the peaks at $\tau = \pm 13\,\text{ns}$ appear lower than the subsequent uncorrelated peaks. The relative peak height might be obscured by the decaying envelope observed in Fig. 4.10 (b). The observed asymmetry around $\tau = 0$ is not expected to be a property of the photon source as it would be averaged out, instead it is expected to be a consequence of the detection setup. An unequal splitting ratio of the recombine beamsplitter could induce this asymmetry, but would lead to a reduced classical visibility, which was not the case. Unequal detector efficiency is likely causing the observed asymmetry

4.3 Conclusion

Two platforms for a QD based single-photon source were investigated.

A QD embedded in a photonic crystal cavity demonstrated a single-photon purity of $g^{(2)}(0) = 0.06 \pm 0.026$, while a count rate of $\Gamma_{\text{det}} = 37 \pm 0.2\,\text{kHz}$ was detected. An indistinguishability of $V = 0.03 \pm 0.003$ was extracted and it was concluded that the photons were distinguishable.

The waveguide based source demonstrated an impressive single-photon purity of $g^{(2)}(0) = 0.014 \pm 0.004$ under quasi-resonant excitation conditions, with a detected count rate of $\Gamma_{\text{det}} = 38 \pm 0.2\,\text{kHz}$. Under these excitation conditions two-photon interference was observed with a visibility of $V =$

0.32 ± 0.024. By increasing the temporal spacing between the emitted photons, single-photon indistinguishability was demonstrated up to $\tau = 13\,\mathrm{ns}$ with an extracted visibillity of $V_{13\,\mathrm{ns}} = 0.24 \pm 0.06$.

QDs in photonic crystal structures are therefore viable candidates for single-photon technologies.

Chapter 5

Single-photon time-division demultiplexing

An optical quantum computer requires an initial state consisting of multiple qubits. Efficient generation of a state containing multiple single-photons is therefore necessary to enable optical quantum computing. A multiple single-photon state is denoted a N-fold single-photon state, where N is the number of single-photons. The state is characterized by consisting of N single-photons in separate and orthogonal modes.

A N-fold single-photon state is realized by synchronizing N single-photon sources. The sources emit into separate modes and the single-photons are collected into individual optical fibers [66]. This method is often used with SPDC sources, but their inefficient single-photon generation makes SPDC sources unsuited for scalable applications.

Alternatively multiple deterministic single-photon sources, e.g. QD, under synchronized excitation could generate the N-fold single-photon state. Currently there are significant challenges in producing indistinguishable single-photons from separate QDs [119]. For the single-photons to be suitable for most quantum computing scheme, they must maintain a high degree of indistinguishability.

To ensure a large degree of indistinguishability, indistinguishable single-photons from an efficient source should be modified into an N-fold single-photon source. A QD can be utilized as a source of indistinguishable single-photons, with application in photonic quantum computing [120, 121]. The single-photons emitted from the QD are collected in an optical fiber for later manipulation and detection. Single-photons guided in an optical fiber are time-division multiplexed, as the single-photons are temporally spaced in a single channel. To manipulate the individual photons, the interaction must be faster, than the temporal separation of the single-photons.

Alternatively, the single-photons are time-division demultiplexed. Time-demultiplex single-photons are propagating parallel in time but in orthogonal modes. By demultiplexing the stream of single-photons emitted from the QD, the temporal separation of the photons is eliminated and the single-photons are propagating in different modes, e.g. different optical fibers. The demultiplexing of single-photons is achievable using passive or active components.

Time-division demultiplexing of single-photons enables the ability to manipulate and interfere single-photons as desired using passive optical components. A N-fold single-photon source is well suited for generating input states for LOQC applications.

In this chapter a scheme to actively perform time-division demultiplexing of single-photons is presented. The scheme is based on an electro-optical modulator (EOM), which manipulates the polarization of single-photons. The modulation of the single-photon polarization on $\sim$ ns timescale is utilized to route and synchronize single-photons.

A setup implementing the scheme is build, characterized and utilized to generate a demultiplexed 3-fold single-photon state.

5.1 Multiplexing introduction

The concept of multiplexing and demultiplexing is well known from classical optical communication, where these techniques are utilized to increase the communication bandwidth of an optical fiber. Multiplexing entails having multiple channels combined into a single channel, which requires orthogonal modes to avoid crosstalk, e.g. frequency or polarization. Demultiplexing is the reverse process where information from a single channel is distributed into multiple channels. In classical communication frequency-division multiplexing is used, where the different information channels have different frequencies and are separated using an array waveguide grating [122]. Frequency-division multiplexing is unsuitable for demultiplexing of single-photons in the context of quantum information processing, as the photonic qubits are required to have the same frequency for application in quantum information gates.

Spatial multiplexing can modify N inefficient probabilistic sources into a single near-deterministic photon source [123]. N inefficient sources are connected to a main channel through an active switch. When the creation of a single-photon in one source is heralded that source is switched to the main channel and the remaining sources are blocked. By having sufficient sources the success probability of single-photon creation per pulse approaches unity. Spatial multiplexing was used to improve the performance of a SPCD source. By using two sources the heralded count rate was enhanced by 63% [123].

Time-division multiplexing of a single probabilistic source can form an efficient source of single-photons at a chosen reduced repetition rate [124]. A single inefficient source is coupled to a switching network that switches between N delay lines, where the delay matches a multiple of the pulse separation time. When the successful creation of a single-photon is heralded, the single-photon is switched into a delay line that matches the reduced repetition rate, by having a sufficient number of delay lines the overall source efficiency is enhanced. If a single-photon source has a generation probability of 50% and the demultiplexing setup consist of a single delay, the single-photon probability is enhanced at the repetition rate $\Gamma_{\mathrm{Rep}}^{\mathrm{Mux}} = \frac{1}{2}\Gamma_{\mathrm{Rep}}^{\mathrm{Initial}}$. A switching cycle consists of two creation attempts, if the first creation event is successful the photon is delayed. If the second excitation event is successful no delay is applied. If both creation events are successful, one delay line is coupled to the output. In some switching cycles neither pulse one or two are successful and the single-photon probability is enhanced to 75%. By adding multiple delay lines the single-photon probability approaches unity.

These applications are based on the heralding of single-photon generation, which is possible with SPDC sources. In SPDC the heralding occurs as a consequence of the photon pair generation. Heralding of single-photon emission is also possible in the context of QD emission, as the cascaded decay of the QD bi-exciton leads to a deterministic preparation of the groundstate exciton and the detection of a bi-exciton single-photon therefore heralds groundstate single-photon [125].

Introduction to Pockel cells

An EOM is a device, which employs an electro-optical effect to modulate an optical field. A crystal where the inversion symmetry is broken, e.g. Lithium Tantalate (LTA), exhibts an additional birefringence when an electric field is applied. A linear response to the electric field characterizes the Pockel effect. A transverse EM-field propagating in the crystal experiences a difference in refractive index along the ordinary- (o) and the extraordinary axis (e) given by:

$$\begin{aligned} \Delta n_{\mathrm{o}} &= -\frac{1}{2} n_{\mathrm{o}}^3 r_{13} E. \\ \Delta n_{\mathrm{e}} &= -\frac{1}{2} n_{\mathrm{e}}^3 r_{33} E. \end{aligned} \tag{5.1}$$

Here n_{o} (n_{e}) is the refractive index along the o (e) optical axis when no electric field is applied. The electro-optical coefficients r_{13} and r_{33} describes the material response to an applied electric field. Finally E is the electrical field applied to the crystal. As the electro-optical coefficients are unequal, the phase between the o and e-axis is controlled by the applied field. An unequal phase shift between the o and e-axis amounts to a rotation of the polarization. An EOM is therefore perceived as a voltage controlled polarization rotator(wave plate). The total phase retardation between the o and e-axis of a photon with wavelength λ is given by [126]:

$$\Gamma = |\phi_e - \phi_o| = \frac{2\pi}{\lambda} |(n_{\mathrm{e}} - n_{\mathrm{o}}) + (\Delta n_{\mathrm{e}} - \Delta n_{\mathrm{o}})| L = \Gamma_0 + \Gamma_\Delta. \tag{5.2}$$

The phase retardation Γ_0 that occurs as a consequence of the natural birefringence is in the context of the Pockel effect neglected, as it is a static effect. Instead the focus is on the retardation pertaining to the electric field Γ_Δ.

The electric field is either transversely or longitudinally applied to the crystal, relative to the propagation direction of the photons. In a transverse Pockel cell with width d, the applied electric field is given by $E = \frac{V}{d}$.

The voltage needed to rotate the polarization into the orthogonal state, i.e. $\Gamma_\Delta = \pi$, is called the halfwave voltage V_π. From Eq. (5.2) the halfwave voltage for the longitudinal and transverse Pockel cell is determined:

$$V_\pi^{\mathrm{Longi}} = \frac{\lambda}{n_{\mathrm{e}}^3 r_{33} - n_{\mathrm{o}}^3 r_{13}} \qquad V_\pi^{\mathrm{Trans}} = \frac{\lambda}{n_{\mathrm{e}}^3 r_{33} - n_{\mathrm{o}}^3 r_{13}} \frac{d}{L}. \tag{5.3}$$

These equations are used to determines the required voltage to rotate photons between orthogonal polarizations.

5.2 Demultiplexing scheme

A general scheme for demultiplexing a stream of single-photons is proposed, where the only requirement for the source is single-photon creation at a fixed temporal separation. Fig. 5.1 shows a schematic representation of the scheme for 3-fold single-photon state generation, but the scheme is readily extendable to higher photon number. Single-photons emitted at the repetition time $\Delta\tau$ are coupled out of the input fiber and aligned into the Pockel cell. When a photon leaves the Pockel cell it is sent through a polarizing beamsplitter (PBS), which discriminates between horizontal and vertical polarized photons. If horizontally polarized the photon is transmitted and is coupled into the fiber

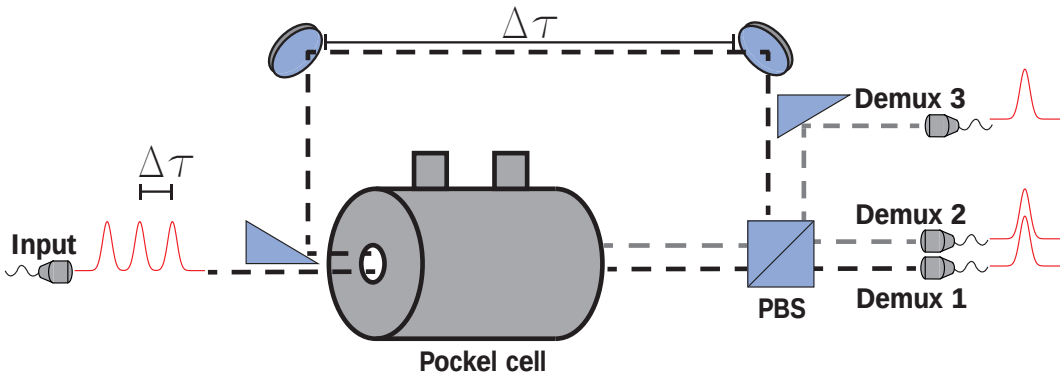

Figure 5.1: Schematic representation of the demultiplexing setup. Single-photons emitted $\Delta\tau$ apart are coupled out of the fiber labeled Input, where the beam is coupled into the Pockel cell. After coupling out of the Pockels cell the photons are sent through the PBS, where transmitted photons are coupled into the fiber labeled Demux 1. Reflected photons are sent in a temporal delay loop matching the time separation of the single-photon. The delayed photons are aligned through the Pockel cell, the exiting beam is marked by gray, and sent through the PBS. Transmitted photons are coupled into Demux 2, while the reflected photons are coupled into Demux 3.

labeled Demux 1. If the polarization of the photon is vertical, it is reflected of the PBS. The reflected photon is aligned into a delay loop, where the path length matches the temporal separation of the single-photons. The single-photon in the delay loop is aligned into the Pockel cell, when the photon exit the Pockel cell it is sent through the PBS. Transmitted photons are coupled to the fiber labeled Demux 2, while reflected photons are coupled into Demux 3.

The Pockel cell is required to obtain full switching of the single-photon on timescales faster than the separation time $\Delta\tau$ for the scheme to operate at maximum efficiency.

Fig. 5.2 shows the photon configuration for the individual steps in the demultiplexing process. In Fig. 5.2 (a) the first photon enters the setup, the photon is polarized along the horizontal axis as it enters the Pockel cell. As no electric field is applied to the cell, the photon remains horizontally polarized and is therefore reflected by the PBS. Fig. 5.2 (b) shows the next time instance, where PH3 is in the delay path and PH2 enters the system. PH2 is also horizontal polarized and matches the polarization of PH3. As the two photons enter the Pockel cell, no electric field is applied and PH3 and PH2 remain horizontal polarized. Fig. 5.2 (c) shows the third time instance, where both PH3 and PH2 are reflected of the PBS. PH3 is being picked off by a right angle mirror and coupled into the fiber called Demux 3. At the same time PH2 is reflected into the delay loop and PH1 enters the system polarized along the horizontal axis. As PH2 and PH1 enters the Pockel cell, an electric field is applied to the cell. The two photons are rotated to the vertical polarization, meaning they are transmitted by the PBS. Fig. 5.2 (d) shows the final time instance, where photons PH2 and PH1 are being coupled into Demux 2 and Demux 1 respectively. PH3 is delayed by an additional $\Delta\tau$ and any residual temporal difference is removed after coupling into the fibers. Successful application of the setup leaves the three single-photons demultiplex, as they are temporally synchronized in individual fibers.

The method is readily scalable to a larger photon number by coupling PH3 into the Pockel cell instead of coupling it into Demux 3. By continuously coupling additional paths through the cell, the

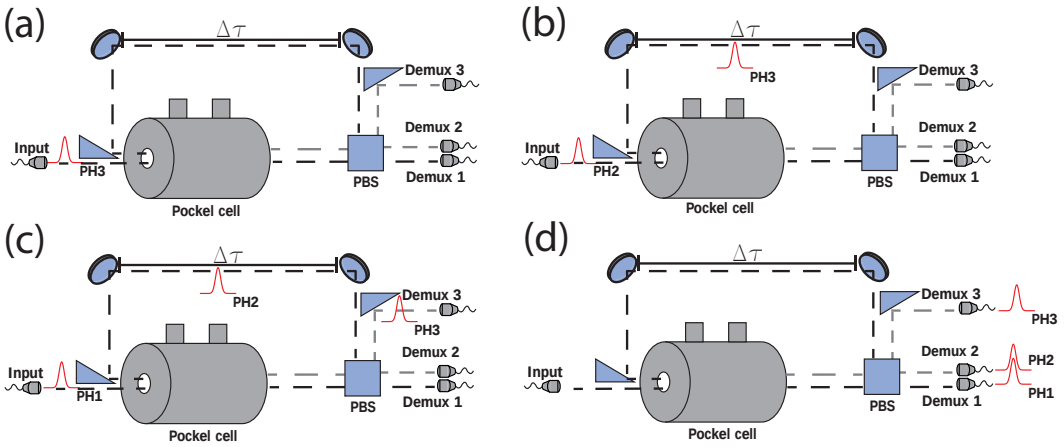

Figure 5.2: Photon configuration at various time steps. **a)** The first photon labeled PH3 enters the circuit, the photon is horizontally polarized. **b)** No electric field is applied to the Pockel cell so PH3 is reflected of the PBS and into the delay loop. The second photon PH2 which is also horizontally polarized enters the circuit. **c)** No field is applied to the Pockel cell and both PH3 and PH2 are reflected of the PBS. The photon PH3 is coupled into the fiber Demux 3 using a right angle prism mirror and PH2 is send to the delay loop. When this occurs PH1 enters the circuit. **d)** An electric field is applied to the cell making it rotate the polarization of PH2 and PH1. The two photons are therefore transmitted and PH2 is coupled into Demux 2 and PH1 is coupled into Demux 1. By adjusting the length of the outcoupling fibers the three photons are synchronized.

scheme is scalable to arbitrary photon number.

The Pockel cell

For the experimental demonstration a Conoptics 360-80 LTA phase modulator is used. The optical properties of LTA are shown in Table. 5.1 [127]. The Conoptics 260-80 cell is a transverse cell with a length $L = 80\,\text{mm}$ and $d = 2\,\text{mm}$. Using Eq. (5.3) the reqired halfwave voltage at $\lambda = 980\,\text{nm}$ is calculated to be $V_\pi = 110\,\text{V}$.

Wavelength (nm)	n_e	r_{33}(pm/V)	n_o	r_{13}(pm/V)
980	2.1443	29.6 ±0.3	2.1402	6.96 ± 0.07

Table 5.1: Electro-optical properties of LTA at $\lambda = 980\,\text{nm}$. In context of electro-optical modulation the required parameters are the electro optical coefficients r_{13}, r_{33} and the steady state refrective index of the (extra-)ordinary axis n_o (n_e) [127].

To induce polarization rotation besides the natural birefringence, a voltage is applied to the electrodes, which is supplied from a Conoptics 25DS amplifier. Fig. 5.3 shows the response of the Pockel Cell recorded by a Perkin-Elmer APD. The signal is generated by sending a C.W. laser through the Pockel cell, while driving the Pockel cell at V_π. The trigger signal is generated by a Field-Programmable Gate

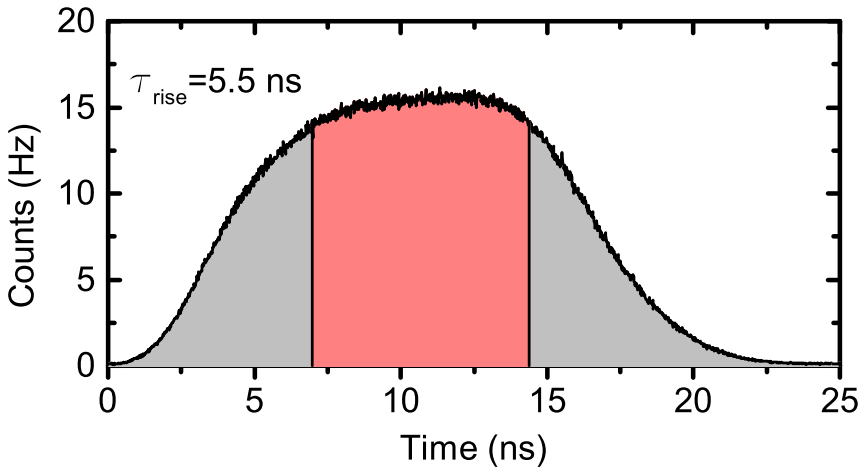

Figure 5.3: The response function of the Pockel cell when driven at V_π. The rise time is extracted to $\tau_r = 5.5 \pm 0.1\,\text{ns}$. The switching window is marked in red and is extracted to $\tau_{\text{switch}} \sim 7\,\text{ns}$. The response function is measured by a C.W. source modulated by the Pockel cell at $\Gamma_{\text{trig}} = \frac{\Gamma_{\text{laser}}}{3}$ and detected using an APD.

Array (FPGA), by frequency dividing a $\Gamma_{\text{laser}} = 76\,\text{MHz}$ signal from the excitation laser by three. The demultiplexing scheme requires that the Pockel cell rise time τ_{rise} is less than the temporal separation $\Delta\tau$. This requirement ensures full rotation occurs while no photons are present in the crystal. From the measured response the rise time is determined to $\tau_{\text{rise}} = 5.5 \pm 0.1\,\text{ns}$. The rise time is defined as the elapsed time from the signal is 10% to it reaches 90%. Fig. 5.3 also demonstrates the switching window of the Pockel cell, the switching window stems from the electronics and the Pockel cell having intrinsic delay before returning to the original configuration. The switching windows is defined as time duration where the intensity is 90% of maximum. Fig. 5.3 shows the switching window marked in red and the duration of the window is $\tau_{\text{switch}} \sim 7\,\text{ns}$, while the elapsed time from on to off is $\tau_{\text{cycle}} \sim 20\,\text{ns}$. According to the vendor specifications the maximum repetition rate is $\Gamma_{\text{trig}} = 30\,\text{MHz}$ which is limited by the amplifier [128, 129]. As the required rate for the scheme is $\Gamma_{\text{trig}} = \frac{\Gamma_{\text{laser}}}{3} = 25.3\,\text{MHz}$, the setup is not limited by the repetition rate of the amplifier. For applications that requires faster switching rates, alternative driving options could drive the Conoptics 360-80 at upto $\Gamma_{\text{trig}} = 200\,\text{MHz}$ [128]. The switching window reduces the required precision of the photon arrival time. Additionally, the required precision of the delay loop length is reduced as the photon can arrive at any time during the switching window.

Setup and alignment

To experimentally demonstrate active demultiplexing of single-photons, the setup outlined in Fig. 5.1 is constructed. The objective is to obtain a method for reproducible alignment of the setup.

Using two pinholes, at the same height, the incoupling beam is aligned straight and parallel to the optical table. The fibercoupler is placed on a translation stage, which controls its position in the xz-plane, and is aligned to the first pinhole. By utilizing a tip-tilt mount the angle of the fiber coupler is controlled, which is utilized to align the beam through the second pinhole. By continuously reiterating the alignment to the pinholes, a convergence is achieved where the beam path through both pinholes

is maximized. Eliminating the need for optical mirrors after the fibercoupler is advantageous, as dielectric mirrors might cause an unstable polarization. Two $f = 250\,\mathrm{mm}$ lenses are introduced, which forms a telescope with unity magnification. Due to the 2 mm aperture of Pockel cell it is necessary to focus the beam through the Pockel cell, to prevent cutting of the beam. The lenses are mounted in xz-precision stages enabling precise control of their position with respect to the beam. The first lens is placed after the first pinhole and the signal through the second pinhole is optimized. The second lens is positioned in order to recollimate the beam and the signal through the second pinhole is optimized using the second lens. This method ensures the beam enters the lenses at the center and not being displaced by the lenses.

The Pockel cell is introduced into the beam path while monitoring the signal through the second pinhole and the signal is optimized. An one inch PBS is then placed in the beam path and extinction ratio is optimized for the reflection. The beam reflected of the PBS is propagating through a meander of optical mirrors in order to obtain the correct delay. The dielectric mirrors might induce polarization rotations but silver mirrors are avoided, due to their reduced efficiency. A right-angled mirror is utilized to couple to path into Pockel cell, the right-angled mirror is positioned close to the original beam without cutting it. The final two mirrors before the right-angle mirror are used to align through the cell. A third $f = 250\,\mathrm{mm}$ lens is placed before the right-angled mirror to focus the delayed beam through the Pockel cell. After the single-photons have left the demultiplexing setup at the PBS, they are coupled into single-mode fibers using dielectric mirrors.

5.3 Single-photon efficiency

In contrast to classical information processing, in quantum information processing losses cannot be overcome by increasing the signal strength [130]. On the contrary any loss causes a reduced qubit rate, which scale exponentially with the number of qubits required. This highlights the importance of quantifying and minimizing losses in single-photon applications. To estimate the single-photon transmission, the individual components of the demultiplexing setup are therefore characterized.

Achieving a N-fold single-photon state

To demultiplex a single-photon source into a N-fold photon source, N consecutive single-photons are required, the probability is determined by:

$$P_{N\mathrm{photon}} = \eta^N. \tag{5.4}$$

Where η is the single-photon probability, η is a product of a multitude of processes, which are separated into four main constituents:

$$\eta = \eta_{\mathrm{Gen}}\,\eta_{\mathrm{Out}}\,\eta_{\mathrm{Setup}}\,\eta_{\mathrm{Filter}}. \tag{5.5}$$

Here η_{Gen} is the generation efficiency of a photon at the frequency of interest, which included the quantum efficiency of the QD and the probability of generating an excitation in the desired state. Changes in the charge configuration around the QD might block the state of interest from being excited, called blinking, which lowers η_{Gen} [131]. The outcoupling efficiency η_{Out} describes the efficiency of the single-photon coupling to the optical fiber used to collect the emission. The coupling efficiency

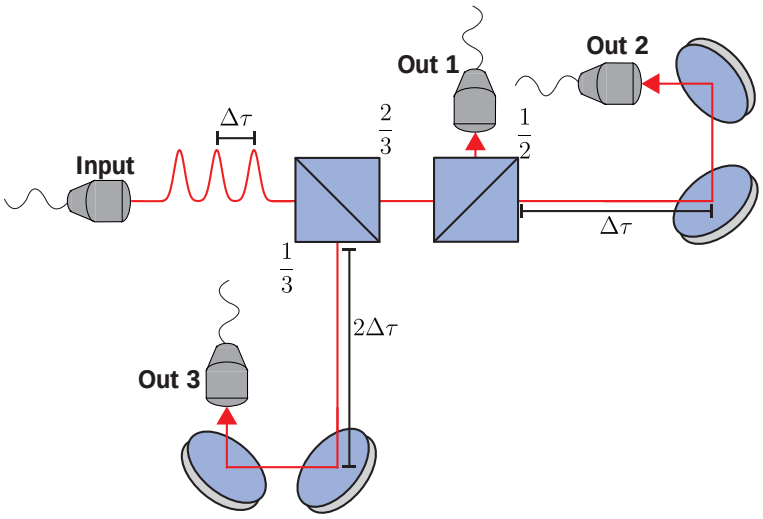

Figure 5.4: A schematic representation of a probabilistic setup for time-division demultiplexing. Single-photons separated by $\Delta\tau$ are entering the setup at the fiber labeled Input. A beamsplitter with $R = \frac{1}{3}$ and $T = \frac{2}{3}$ is followed by a beamsplitter with $R = T = \frac{1}{2}$ in transmission. At the outputs of the beamsplitters, the photons are coupled into optical fibers. The optical path lengths are matched to multiples of $\Delta\tau$, in order to temporally synchronize single-photons in the different fibers.

between QD and optical mode, i.e. the β-factor, as well as the outcoupling efficiency from the photonic structure are included in η_{Out}. The total transmission of optical components in the setup is included in η_{Setup}. Finally it is necessary to spectrally separate the emission of the exciton line of interest from undesired emission. The transmission of the filter setup is characterized by η_{Filter} . Each of the constituents can be carefully evaluated and optimized.

The single-photon efficiency η is estimated from the measured single-photon rate Γ_{QD}, excitation repetition rate Γ_{laser} and the detector efficiency η_{det} through $\eta = \frac{\Gamma_{\mathrm{QD}}}{\Gamma_{\mathrm{laser}}\eta_{\mathrm{det}}}$. This method potentially underestimates the rate of consecutive photons, as the QD blinking is ignored. If the QD is blinking, the measured count rate is an average of both the on and off state of the QD. If the lifetime of the on-state is longer than the time required to emit N photons $\tau_{\mathrm{blink}} > \frac{1}{N\Gamma_{\mathrm{laser}}}$, the temporal correlation of the on-state means the N-fold single-photon rate is greater than the rate predicted from η.

Even though the effect of blinking causes an underestimate of the consecutive photon rate, the detected count rates set a lower bound. The predicted rate of N consecutive single-photon states is calculated using:

$$\Gamma_{N-\mathrm{fold}} = P_{N-\mathrm{fold}}\frac{\Gamma_{\mathrm{laser}}}{N}. \tag{5.6}$$

The probability of achieving N consecutive photons $P_{N-\mathrm{fold}}$ is not directly measurable, but is estimated as η^N. The predicted rate of N consecutive single-photons also provides an upper bound for the expected demultiplex N-fold single-photon source.

Efficiency of a probabilistic demultiplexing scheme

The need for a deterministic single-photon demultiplexing setup is best illustrated by comparing it to a probabilistic source of same photon number. Fig. 5.4 shows a setup for 3-fold single-photon

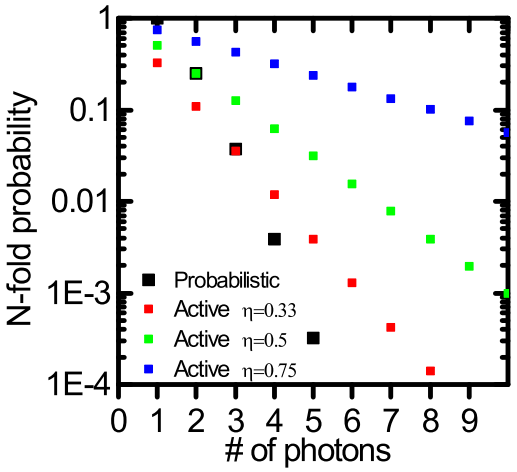

Figure 5.5: The probability of obtaining a N-fold single-photon as a function of the number of photons in the desired state. The probability is shown for both a probabilistic demultiplexing scheme and an active scheme with an assumed single-photon transmission of η. The intersection signifies the break even point where active demultiplexing is more efficient than the probabilistic approach.

source. Single-photons are sent through the first beamsplitter, which reflects s$R = \frac{1}{3}$ and transmits $T = \frac{2}{3}$. The second beamsplitter reflects $R = \frac{1}{2}$ and transmits $T = \frac{1}{2}$, the two beamsplitters generate a superposition of 27 different states with equal probability. The desired 3-fold single-photon state is generated when the first photon is transmitted and then reflected, the second photon is transmitted twice and the third photon is reflected at the first beamsplitter. Each of these events has a probability of $\frac{1}{3}$ and the total probability for a successful 3-fold single-photon state is therefore $\frac{1}{27}$. Since the delay in each output is matched to the temporal spacing of the single-photons in the input, the three photons in the fibers are temporally synchronized.

The scaling for N-fold single-photon source is determined by extrapolating the above argument. The scheme needed to generate the desired time synchronized N-fold single-photon state is a 1 to N beamsplitter. The probability of a single-photon taking the desired path is $P_1 = \frac{1}{N}$. Since a single successful N-fold single-photon event is conditioned on all N single-photons taking the desired path, the scaling for a N-fold single-photon state is:

$$P_N = N^{-N}. \tag{5.7}$$

Eq. (5.7) is the optimal scaling for a probabilistic source and does not account for insertion losses. This unfavorable scaling of passive demultiplexing makes it unsuitable for scalable implementation.

For active demultiplexing to outperform passive demultiplexing, the single-photon transmission should exceed $\frac{1}{N}$. This scaling shows the required single-photon transmission for active demultiplexing is relaxed when the photon number is increased. Fig. 5.5 shows the N-fold probability as a function of number of photons, for probabilistic demultiplexing and for active demultiplexing for different efficiencies. Fig. 5.5 illustrates the breakeven point where active demultiplexing is more efficient than the probabilistic approach.

Fig. 5.5 also demonstrates the exponential scaling of the losses with the photon number, which highlights the need for highly efficient active demultiplexing for large photon number applications.

Component	Transmission (%)
Transmission 1st pass	$94.3\% \pm 0.4\%$
Transmission of V at PBS	$98.4\% \pm 0.1\%$
Reflection of H at PBS	$98.9 \pm 0.1\%$
Transmission 2nd pass	$75.7\% \pm 0.3\%$
Fiber coupling Demux 1	$91.7\ \% \pm 3.3\%$
Fiber coupling Demux 2	$89.2\ \% \pm 3.2\%$
Fiber coupling Demux 3	$82.5\ \% \pm 2.1\%$
Total path transmission	
Demux 1	$86.4\% \pm 3.0\%$
Demux 2	$63.7\% \pm 2.3\%$
Demux 3	$58.8\% \pm 1.5\%$

Table 5.2: Measured transmission efficiencies for the various components of the demultiplexing setup.

Measured efficiency

In order to provide an estimate of the expected rate of a 3-fold single-photon state, the transmission through each component of the setup is measured. Measuring these efficiencies with single-photons is impractical and instead the measurement is performed using a diode laser, that is detected using a power meter. The measurement is conducted by integrating the signal for one minute and obtaining the mean value, the errors are then extracted from the standard deviation on the measurement. The obtained transmissions are shown in Table. 5.2. The first value in Table. 5.2 is the transmission efficiency through the Pockel cell, which quantifies how well the incoupling fiber is aligned to the Pockel cell. As seen from Table. 5.2 the obtained transmission is $94.3\% \pm 0.4\%$. The obtained transmission surpasses the vendors estimate of $T > 85\%$ [128].

The second value in Table. 5.2 is the transmission of vertical polarization at the PBS, which shows the discrimination between the two polarizations and route the single-photon to the correct path. Any deviation from the desired routing lowers the generation of the 3-fold single-photon state. This value is strongly dependent on the incident angle of the beam and the optimum angle is not perpendicular. Since the path of the incident photon is fixed by the coupling through the Pockel cell, the only option to improve the extinction ratio is to rotate the PBS around its axis. The reflected beam is the displaces as the PBS is rotated around the axis. Since the reflected beam is part of the delay loop the range of rotation is limited to not cause a large beam deflection. The transmission of the vertical polarization is $98.4\% \pm 0.1\%$. The reflection of the horizontal polarization at the PBS was measured to $98.9\% \pm 0.1\%$, which shows the PBS does not introduce significant loss.

The efficiency of the incoupling of the delay loop into the Pockel cell is measured to $75.7\% \pm 0.3$, which is dramatically lower than the value obtained of the first pass transmission efficiency. As a half-wave plate is introduced in the path and rotated to maximize the throughput, polarization mismatch is ruled out. Instead the path must be misaligned to the Pockel cell. Using a CCD camera the transmitted beam is inspected, but the beam profile does not indicate any cutting of the beams.

Currently the cause of the low transmission is unclear.

Finally the incoupling into the individual fibers is determined. The transmitted beam of the first pass is coupled into the fiber designated Demux 1 with a coupling efficiency of $91.7\% \pm 3.3\%$. The transmitted beam of the second round trip is coupled into the fiber labeled Demux 2 with an efficiency of $89.2\% \pm 3.2\%$ and the reflected beam of the PBS of the delay loop is coupled into the fiber labeled Demux 3 with an efficiency of $82.5\% \pm 2.1\%$. The measured efficiency does also include propagation losses in the fiber. The measured efficiency of the Demux 1 and 2 is within tolerance of air to fiber couplings, but could potentially be improved by employing AR-coated fibers. The coupling efficiency of Demux 3 is considerably lower than the comparable outcoupling fiber Demux 2. The coupling efficiency of the two fibers is expected to be comparable, as they are the transmitted and the reflected component of the same beam, which indicates potentially some component in the fiber coupler has to be replaced.

One thing of note is the measured error on the fiber coupling efficiencies is higher than the previously measured errors. While measuring the coupling efficiency into the fibers, a slow periodic oscillation of the signal out of the fiber is observed. These oscillations are observed in all three fibers, causing an increase of the observed error. These oscillations are not observed when measuring the power before the fiber. Since there is no polarization projection after the outcoupling fiber, rotations of the polarization is ruled out as causing the fluctuations in power. These oscillations might be a consequence of mechanical instability or temperature fluctuation across the fiber.

Having measured the transmission of the individual component, it is possible to estimate the total single-photon efficiency as well as the three photon probability. By multiplying the efficiency of each of the components in the individual paths, an estimate of the total single-photon efficiency is aggregated. The resulting single-photon efficiency is shown in Table. 5.2, for Demux 1 the total efficiency is estimated to 86.4%. For the remaining two paths, the low transmission through the Pockel cell of the second round trip is causing a lower overall path efficiency, with 63.7% and 58.8% for Demux 2 and 3 respectively. This illustrates the importance of improving the incoupling of the second round trip.

Finally the 3-fold single-photon probability is estimated from the product of the single-photon probabilities:

$$P_{3-\text{fold}} = 32.4\% \pm 1.8\%. \tag{5.8}$$

The above estimate does not include the detector efficiencies, but these are ignored as they are not an element of the demultiplexing scheme.

Based on these measured efficiencies the probability of generating a 3-fold single-photon state, when three consecutive photons are coupled into the setup, is close to one in three. When comparing this combined efficiency to the ideal prediction of the probabilistic demultiplexing of $\frac{1}{27}$, a dramatic performance enhancement should be attainable.

5.4 Active demultiplexing of a solid-state source

To demonstrate the feasibility of active demultiplexing of single-photons, a single-photon source with sufficient count rates is needed. Sufficient count rates are needed to ensure three consecutive photons

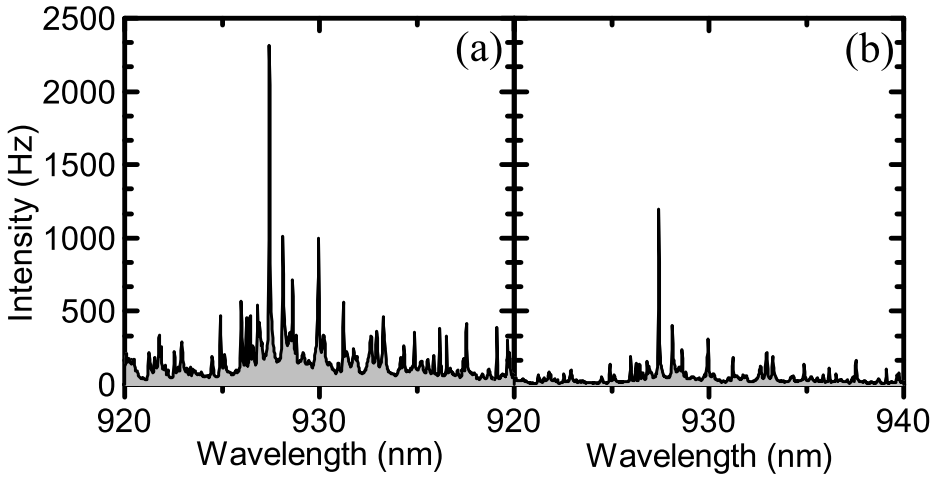

Figure 5.6: Spectrum of the emission collected into the optical fiber under pulsed excitation at 856 nm**a)** at P_0 **b)** at $\frac{1}{2}P_0$. In both spectra multiple emission lines are visible. Besides multiple emission lines, a broadband background, overlapping in frequency with the emission lines, is present. Reducing the excitation power also yields a reduction of the background.

are being coupled in to the demultiplexing setup at rates, which yields adequate statistics in reasonable integration time.

Bright single-photon source

The source of the single-photons is a solid state QD embedded in a photonic crystal waveguide, which enhances the coupling efficiency with the desired mode. The photonic crystal waveguide is coupled to a tapered ridge waveguide. The purpose of the tapered waveguide is to generate an efficient overlap with an optical fiber. By mounting an optical fiber on a piezoelectric stage it is possible to align the fiber to the tapered waveguide in order to couple a large fraction of the emission into the fiber. Using this method single-photon count rates in the order of $\sim$ MHz are obtained. Such count rates makes it feasible to create a three photon state at a reasonable rate.

Fig. 5.6 shows spectra from the sample after the fiber has been aligned to the tapered waveguide. Several emission lines are present in the spectrum, but the emission line of interest is the most intense line at 927.42 nm. Fig. 5.6 (a) shows the emission at the saturation power P_0 of the line at 927.42 nm, while Fig. 5.6 (b) is from the same sample at $\frac{1}{2}P_0$. It is evident from the spectra that besides other emission lines, there is also a considerable background overlapping with the frequency of the strong emission line. Such a background is not suppressed by spectral filtering and contributes to the measured single-photon purity.

In order to suppress the undesired collected emission, the signal is filtered using a grating setup. After the grating setup a HBT measurement is conducted using a fiberbased beamsplitter. Fig. 5.7 (a) shows the HBT measurement of the filtered emission at P_0, the extracted $g^{(2)}(0) = 0.72 \pm 0.017$ does not imply single-photon emission. Fig. 5.7 (b) shows a HBT measurement of the filtered emission at $\frac{1}{2}P_0$, the extracted $g^{(2)}(0) = 0.52 \pm 0.033$ is within the single-photon requirement of $g^{(2)} < \frac{1}{2}$. The sample has been through several thermal cycles, which potentially has lead to a degradation, which

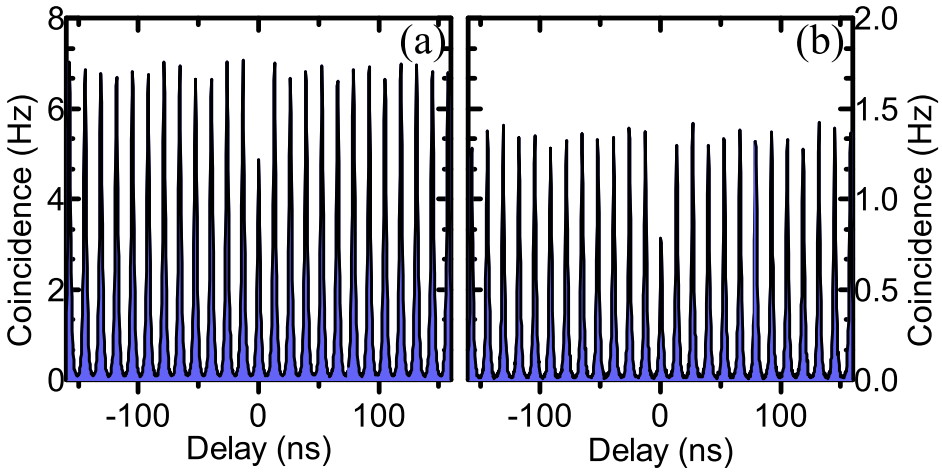

Figure 5.7: HBT measurement of the intense emission line of interest under pulsed excitation at 856 nm **a)**at P_0. The extracted $g^{(2)}(0) = 0.72 \pm 0.017$ signifies a low single-photon purity **b)** at $\frac{1}{2}P_0$. The extracted $g^{(2)}(0) = 0.52 \pm 0.033$.

is manifested as an increased $g^{(2)}(0)$.

The low single-photon purity of the source makes it unsuitable for quantum information processing. The source is still suitable for demonstrating the principle of demultiplexing. If the single-photon purity is not modified by demultiplexing process, it is reasonable this would also be the case for a source with a high single-photon purity. Thereby, if the extracted $g^{(2)}(\tau)$ of the source after demultiplexing is comparable to the initial $g^{(2)}(\tau)$, the scheme is considered successful.

Detection of a 3-fold single-photon state

To demonstrate the successful demultiplexing of the single-photon source, correlation measurements between the three outputs of the setup are required.

Calibration of the Pockel cell

To detect a 3-fold single-photon state, the demultiplexing system is calibrated. A few parameters are available for adjustment such as the applied switching voltage, the steady state voltage and the timing between the electronic trigger pulse and the emission pulse entering the Pockel cell. For demultiplexing the applied voltage is set to V_π and is determined by observing the switched pulse being orthogonal to the preceding pulse. To synchronize the trigger pulse with the optical emission an electronic delay is introduced, using e.g. an electronic delay box or a coaxial cable of appropriate length.

In Fig. 5.8 the temporal evolution of the emission in each of the outcoupling fibers is shown. The signal is observed over a switching period of $\Gamma_{\text{trig}} = \frac{3}{\Gamma_{\text{laser}}}$ during active switching of the cell. The signal is acquired by performing a correlation measurement between the trigger signal and the incoupled photoluminescence recorded on a fibercoupled APD. The correlation measurements are used for calibrating the Pockel cell settings. An advantage of this method is the photoluminescence is being detected as single events and the recorded events are therefore linear in the measured intensity. This means the integration time is significantly reduced compared to calibration using correlation

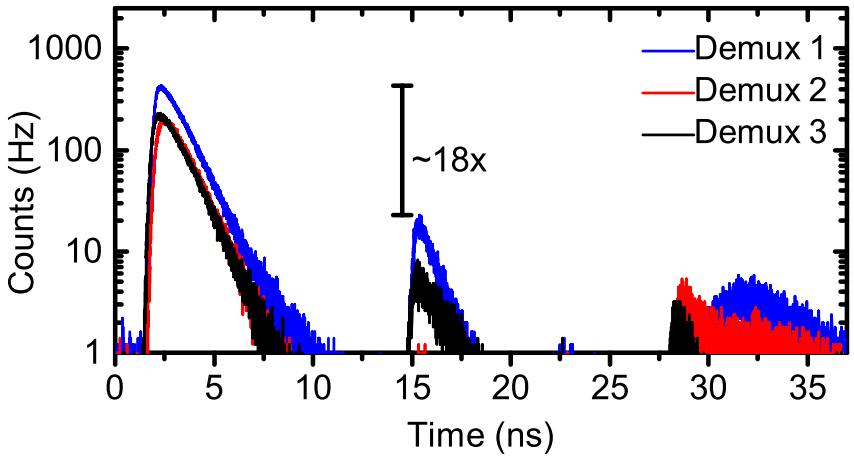

Figure 5.8: Time traces of the outcoupling fibers of the demultiplexing setup during active demultiplexing. The synchronization signal is the frequency divided trigger signal from the excitation laser also used as the switching signal. The suppression of the peaks at 15 ns and 27.5 ns indicates that the emission in the subsequent pulses is switched to the alternate outcouplers. As the reference signal is the same for the traces, these time traces are also used to set the electronic delays between the APDs.

measurements, where the rate of coincidence events is lower. Secondly the Picoharp 300 used for these measurement has a timing resolution of 4 ps [132], which outperforms other timetagging units, which means a timing resolution of a few ps of the rising edge of the PL is possible. Such a timing precision has profound implication for application where synchronization of optical pulses is necessary, e.g.HOM interference.

Fig. 5.8 demonstrates the photoluminescence is temporally synchronized, which is achieved using electronic delay to offset any path length difference in the individual coupling arms. This synchronization is important for the correlation measurements. If the system is used for demultiplexing of photonic qubits, the temporal synchronization has to be performed on the qubits using fibers of appropriate length. For the demonstration of this application it is sufficient to synchronize the electronic signals.

Fig. 5.8 also illustrates the switching of subsequent pulses to the other outcoupling fibers, which is seen by the suppression of the peaks at $\tau = 15$ ns and $\tau = 27.5$ ns, as in the unmodulated scenario all pulses of single time trace should have equal intensity. The signal of Demux 1 is transmitted by the PBS once before being coupled out. The signal in Demux 2 is first reflected into the delay loop and then transmitted by the PBS. The emission in Demux 3 is reflected twice at the PBS.

The signal seen for Demux 1 and 2 has similarities as they are both transmitted in their final step. The ratio between the initial peak and the peak $\tau = 15$ ns is used to quantify how successful the Pokcel cell is in rotating the subsequent pulse to the horizontal polarization. The suppression is extracted to 18.4 ± 1.8, which is less than the measured extinction ratio of the PBS in transmission. The suppression factor appears to be time dependent as the peak at $\tau = 27$ ns is suppressed by a factor of ~ 100, which is comparable to the measured extinction ratio of the PBS. This indicates the switching signal is not optimal even at the setting with the best contrast. Referring to Fig. 5.3 it is seen that the length of the switching window might cause an overlap of two subsequent pulses in the

tail of the switching window. This issue lowers the overall efficiency of the setup and is potentially solved by narrowing the switching pulses after the FPGA. Alternatively an amplifier able to generate shorter pulses might solve the issue. The difference in intensity is due to unequal coupling efficiency of the different paths, induced by the extra round trip and incoupling to the EOM of fiber 2 and 3.

The reason for the differentiation of the signal of Demux 3 to Demux 2 is due to the switching pulse series. The emission at $\tau = 2.5\,\text{ns}$ of Demux 3 is switched to reflect twice of the PBS. The peak at $\tau = 15\,\text{ns}$ is the suppressed reflection of the emission intended for Demux 2, that is set to first reflect then transmit. This also means the emission experiences the rising egde of the switching pulse, which would explain the strong suppression of this peak. The final peak at $\tau = 27\,\text{ns}$ is the emission that was intended to be coupled into Demux 1. This emission is supposed to be transmitted on the first path through the PBS, but is not switched by the Pockel cell. On the second round trip the Pockel cell is set to reflect the emission and the pulse is coupled to Demux 3.

Fig. 5.9 shows HBT measurements of the emission coupled into the demultiplexing setup and of Demux 2. The sample is excited at saturation with a pulsed laser at $\lambda_{\text{laser}} = 856\,\text{nm}$. Correlations on all three output are performed by mating a fiberbased beamsplitter to the respective fiber and recording the correlation events on fibercoupled APDs. Using the HBT the single-photon purity of the source is compared to the value after demultiplexing. The single-photon purity of the source is $g^{(2)}(0) = 0.72 \pm 0.017$. From the HBT measurement it is seen that the emission is correlated at the repetition time $\tau_{\text{laser}} = \frac{1}{\Gamma_{\text{laser}}}$ of the excitation laser as expected. The most immediate difference is the strong correlation at τ_{laser} is suppressed and the correlation instead occurs at $\frac{3}{\Gamma_{\text{laser}}}$. The suppression of the correlation in between $\frac{3}{\Gamma_{\text{laser}}}$ is due to the rerouting of the single-photons by the Pockel cell.

The extracted single-photon purities after the demultiplexing setup are $g^{(2)}_{\text{Demux1}} = 0.72 \pm 0.043$, $g^{(2)}_{\text{Demux2}} = 0.78 \pm 0.075$ and $g^{(2)}_{\text{Demux3}} = 0.71 \pm 0.063$. The single-photon purities after the demultiplexing setup are preserved within the errors compared to the single-photon purity of the source. A preservation of the single-photon purity is also expected for a pure single-photon source and it is therefore argued the scheme is viable for single-photon demultiplexing.

Correlation of demultiplexed source

With the calibration of the switching pulses and the indication of active photon routing, the photon correlation between the outcoupling fibers is required to verify if the demultiplexing scheme is generating a 3-fold single-photon state in the outcoupling fibers.

Measuring three photon correlations between the outputs is the strongest evidence of the desired outcome. In order to measure such a three photon correlation, the PicoHarp correlation device used previously is not sufficient as it is limited to two channels. Instead a quTools quTau timetagging device is utilized for these measurements. This device has eight input channels and a timing resolution of the quTau is 81 ps. The reduced resolution is not an issue, as the measurements are performed under pulsed excitation.

To perform the measurement, the three output fibers are mated with fibercoupled APDs and the correlations are measured using the quTau device. The quTau device performs the correlations internally and the coincidence rates are extracted. It is also possible to access the timestamps of recorded events for post processing.

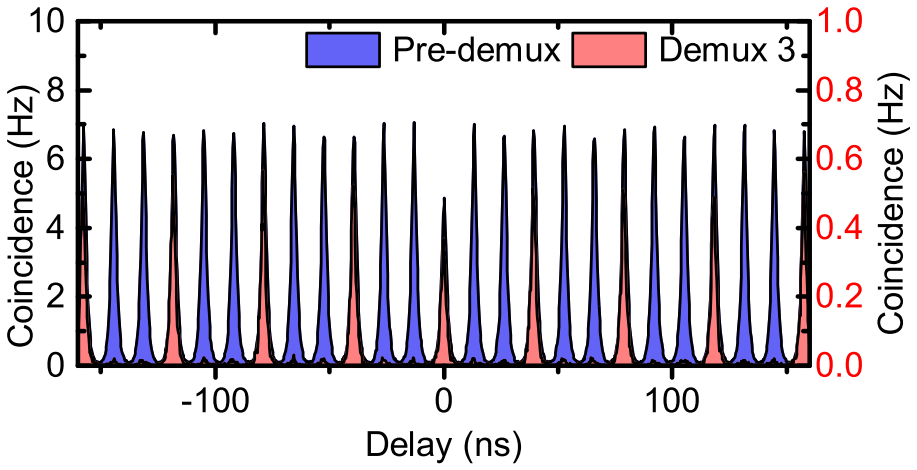

Figure 5.9: HBT measurement on the filtered emission under pulsed excitation at $\lambda_{\text{laser}} = 856\,\text{nm}$ at saturation. The correlation measurement is conducted before the demultiplexing setup and on Demux 3. The measurement before the demultiplexing setup shows a correlated emission at the τ_{laser} and the single-photon purity is extracted to $g^{(2)}(0) = 0.72 \pm 0.017$. The measurements of the individual outcoupling fibers show a suppression at $\frac{3}{\Gamma_{\text{laser}}}$. The extracted normalized second order correlation after the demultiplexing is $g^{(2)}_{\text{Demux3}} = 0.71 \pm 0.063$

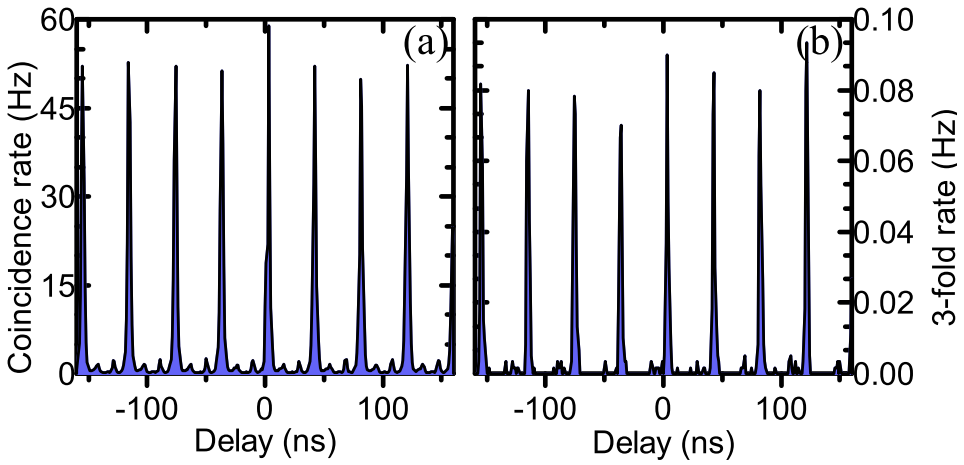

Figure 5.10: Higher order correlation measurements of the demultiplexed emission, the sample is excited at saturation and $\lambda_{\text{laser}} = 856\,\text{nm}$ **a)** Second order correlation between Demux 1 and 3. The signal is strongly correlated at repetition rate of the applied switching. **b)** Third order correlation between Demux 1, 2 and 3 for $\tau_2 = 0$. Again the signal is strongly correlated at the repetition rate of the switching. The fact that 3-fold events are suppressed between the switching events demonstrates the deterministic routing of photons.

The third order correlation $g^{(3)}(\tau_1, \tau_2)$ is calculated as: [133, 134]:

$$g^{(3)}(\tau_1, \tau_2) = \frac{\langle a_1^\dagger a_2^\dagger(\tau_1) a_3^\dagger(\tau_2) a_3(\tau_2) a_2(\tau_1) a_1 \rangle}{\langle a_1^\dagger a_1 \rangle \langle a_2^\dagger a_2 \rangle \langle a_3^\dagger a_3 \rangle}. \tag{5.9}$$

Where a_i is the annihilation operator of a photon in Demux i. This means that if a photon is detected in each of the demultiplexing outputs at the same time, a 3-fold event is registered. The normalized

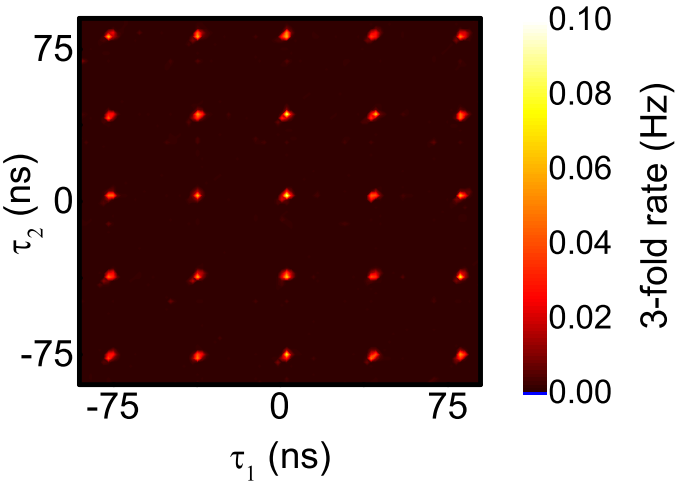

Figure 5.11: Third order correlation of the demultiplex emission as a function of the delay between Demux 1 and 2 (3), τ_1 (τ_2). The third order correlation shows a strong correlation at the repetition period of the switching pulse. The strong suppression of correlation events between the switching windows shows the active routing creates correlation events at the desired repetition period.

third order correlation function is thus expected to have $g^{(3)}(0,0) = 1$ for the demultiplexed source. On the other hand if the active demultiplexing is switched off, a higher order Fock state can be probed, as the setup is equivalent to a third order HBT setup when the switching is inactive. A Fock state with $n = 2$ yields a $g^{(3)}(0,0) < 1$ [134].

Fig. 5.10 (a) shows the second order correlation between Demux 1 and 3. As expected strong correlations are seen at $\frac{3}{\Gamma_{\text{laser}}}$ and there is a strong suppression of the correlations between the peaks.

In Fig. 5.10 (b) the unnormalized third order correlation between Demux 1, 2 and 3 is shown. As the third order correlation is a function of two times, in Fig. 5.10 (b) $\tau_2 = 0$ in order to generate a 2d plot. Fig. 5.10 (b) reveals the third order correlations also occur at $\frac{3}{\Gamma_{\text{laser}}}$. The fact that third order correlations are measured at the induced repetition rate unequivocally demonstrates the active demultiplexing of single-photons. Some correlation between the switching events is observed, which is due to the residual emission not being switched to the correct port. It is possible to suppress these correlations further by improving the discrimination of pulses. These residual correlations lower the extracted 3-fold single-photon rate.

Fig. 5.11 shows the third order correlation between Demux 1, 2 and 3 as a function of the delay between Demux 1 and 2, τ_1 and Demux 1 and 3, τ_2, and reveals a correlation at $\frac{3}{\Gamma_{\text{laser}}}$. Fig. 5.11 reproduces the behaviour from Fig. 5.10 (b) in both τ_1 and τ_2.

Single-photon efficiency

From the single-photon count rates in each of outcoupling fibers an expected 3-fold coincidence rate is extracted. For each output the detected count rate is $\Gamma_{\text{Demux1}} = 187.9 \pm 0.2\,\text{kHz}$, $\Gamma_{\text{Demux2}} = 90.8 \pm 0.1\,\text{kHz}$ and $\Gamma_{\text{Demux3}} = 100.0 \pm 0.1\,\text{kHz}$. The detected count rate before the demultiplexing

setup is measured to $\Gamma_{\text{Input}} = 942 \pm 0.9\,\text{kHz}$. The 3-fold single-photon transmission is estimated as:

$$\eta_{3-\text{fold}}^{\text{active}} = \left(\frac{\Gamma_{\text{Demux1}} + \Gamma_{\text{Demux2}} + \Gamma_{\text{Demux3}}}{\Gamma_{\text{Input}}} \right)^3 = 7.5 \pm 1\%. \tag{5.10}$$

The estimated 3-fold single-photon transmission is considerably lower than the estimate obtained using the C.W. diode. It is not clear why these estimates deviate so dramatically.

Finally the 3-fold coincidence rate is estimated from the single-photon count rates as:

$$\Gamma_{3-\text{fold}}^{\text{active}} = \left(\frac{\Gamma_{\text{Demux1}} + \Gamma_{\text{Demux2}} + \Gamma_{\text{Demux3}}}{\Gamma_{\text{laser}}} \right)^3 \frac{\Gamma_{\text{laser}}}{3} = 3.14 \pm 0.13\,\text{Hz}. \tag{5.11}$$

Extracting the 3-fold single-photon rate

In order to estimate the prospect of using demultiplexing of a single-photon source to generate a 3-fold single-photon state, an estimate of the 3-fold single-photon rate is needed.

The bin width in the correlation measurements determines the temporal resolution of the correlation measurement. The measurement is also dependent on the instrument response function of the detection system, i.e. the minimum time resolution is the 81 ps bin size of the timetagging device. When performing the correlation measurement, increasing the bin width increases the rate of correlation events at the cost of timing resolution.

In order to maximize the detection of 3-fold single-photon events the bin width of the correlation measurement is set to be much greater than the decay time of the emitter in question. Making the bin larger than the decay time ensures that photons emitted in the end of an excitation cycle also contribute to the 3-fold single-photon rate. Conversely, the bin width should not exceed half the pulse separation. This requirement is to minimize the likelihood of photons of a preceding pulse being detected as a photon of the current pulse. By choosing the correct binwidth the 3-fold statistics are improved without increasing the required integration time.

Fig. 5.12 (a) shows the 3-fold coincidence counts as a function of the bin width. This shows the trend of increasing the bin width to increase the detected 3-fold events. The number of events increases linearly with the bin size until the bin size is greater than the lifetime, as extracted from the lifetime in the timetrace measurement. The number of events is then constant and only increases slightly when the bin size allows for overlap between the adjacent excitation pulses. The absence of a large increase is due to the suppression of photons between switching events, caused by the active demultiplexing. As expected the detected 3-fold events increase drastically, when the bin width reaches a width where photon from adjacent switching pulses are counted in the same bin.

The trend in Fig. 5.12 (a) shows that a suitable bin width is 4 ns to perform the analysis. A cross section of the third order correlation with this bin width is shown in Fig. 5.12 (b). Fig. 5.12 (b) shows that at this bin width the correlation becomes quite binary with sharp contrast between the pulses. Such a behavior is desirable when extracting the number of 3-fold event, as the 3-fold rate can be extracted from the peak height.

With the chosen bin width a 3-fold coincidence rate is extracted:

$$\Gamma_{3-\text{fold}} = 0.45 \pm 0.027\,\text{Hz}. \tag{5.12}$$

The extracted rate is considerably lower than the expected rate of 3.6 Hz. By inspecting the recorded single-photon count rates, it is discovered that only $\sim 25\%$ of the counts are recorded. The failure

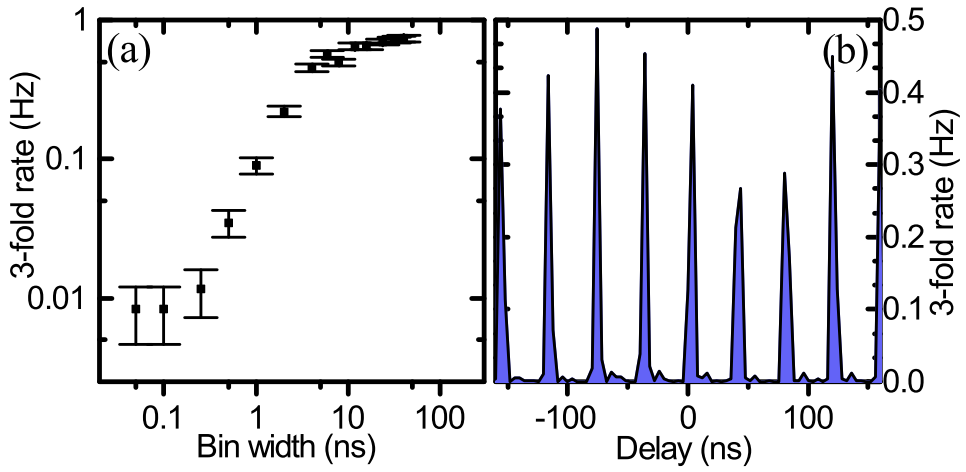

Figure 5.12: **a)** The 3-fold coincidence rate as a function of the coincidence bin width. As the bin width is increased the rate of detected 3-fold single-photon events increases, since the temporal requirement on correlated events is being reduced. **b)** The 3-fold single-photon rate as function of τ_1 using a bin width of 4 ns, $\tau_2 = 0$. Using the chosen bin width it is possible to extract a 3-fold coincidence rate of $\Gamma_{3-\text{fold}} = 0.45 \pm 0.027\,\text{Hz}$.

to record all timestamps is likely related to a buffer filling up without being read out. This is likely caused by a insufficient ability to write to the harddrive rapidly enough, to acquire all timestamps.

The recorded count rates are $\Gamma_{\text{Demux1}} = 44.7 \pm 0.2\,\text{kHz}$, $\Gamma_{\text{Demux2}} = 22.6 \pm 0.2\,\text{kHz}$ and $\Gamma_{\text{Demux3}} = 23.9 \pm 0.2\,\text{kHz}$. Using the recorded rates an expected 3-fold coincidence rate of $\Gamma_{3-\text{fold}} = 0.044 \pm 0.005\,\text{Hz}$ is extracted, significantly smaller than the recorded 3-fold rate.

The loss of recorded events is not expected to occur at random but is expected to be correlated across the three channels. That the loss is correlated is also indicated by the fact, that the measured 3-fold rate is ~ 10 times greater than the 3-fold rate expected from the number of recorded events if the loss was uncorrelated. The indication of a periodic drop of recorded events is therefore examined.

The periodic drop is also confirmed by inspecting the single-photon timestamps. In Fig. 5.13 the single-photon events are binned with a bin width of $2\,\mu$s for each of the channels and plotted as a function of elapsed time. A periodic drop of detected events is observed. The plots also show that the losses are correlated over all three channels, consistent with a failure to write the device buffer to harddrive in sufficient time. It is assumed that the photon rate is uniform in time and the loss is a consequence of the timetagging device. An estimate of the 3-fold count rate, if not data loss had occur is then made. This can be thought of as a post-selection of the time windows where events have been recorded. For Demux 1 the extracted post-selected count rate is $\Gamma^{\text{Post-Sel}}_{\text{Demux1}} = 181 \pm 42\,\text{kHz}$, which is comparable to the count rates measured with the PicoHarp device.

Using the post-selected count rate it is determined that 24.1±5.6% of the events has been recorded. By post-selecting the events recorded and extrapolate the rate to the full time, the extracted 3-fold single-photon rate is:

$$\Gamma^{\text{Post-Sel}}_{3-\text{fold}} = 2.03 \pm 0.49\,\text{Hz}. \tag{5.13}$$

The post-selected 3-fold single-photon rate aligns well with the rate observed, when performing

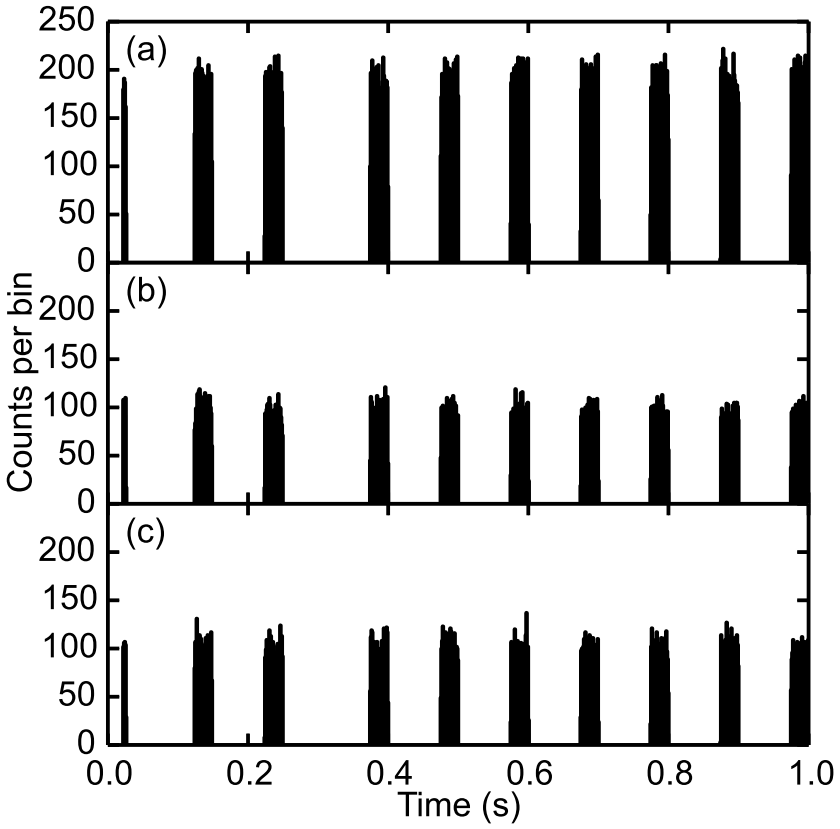

Figure 5.13: Time trace of photon events for **a)** Demux 1 **b)** Demux 2 **c)** Demux 3. The events have been accumulated in bin of width $2\,\mu$s. The plots reveal a reoccurring loss of recorded events. The three plots also shows that drop of recorded events is occurring simultaneous over all three channels.

real-time 3-fold correlation events using the quTools timetagging device. This extracted rate is lower than the 3-fold coincidence rate estimated from the individual single-photon count rates. This is likely explained by the failure to completely switch the single-photons in subsequent pulses as seen in Fig. 5.8. By completely suppressing, the leaking photons the extracted and the estimated 3-fold rate should align. See Appendix B for details on the analysis.

If the efficient source is demultiplexed by probabilistic setup, a 3-fold single-photon rate is:

$$\Gamma^{\mathrm{Prob}}_{\mathrm{N-fold}} = \frac{1}{3^3}\left(\frac{\Gamma_{\mathrm{Input}}}{\Gamma_{\mathrm{laser}}}\right)^3 \frac{\Gamma_{\mathrm{laser}}}{3} = 1.79 \pm 0.005\,\mathrm{Hz}. \tag{5.14}$$

The expected 3-fold single-photon rate from the probabilistic scheme is thereby three times greater than the measured 3-fold single-photon rate. Conversely, the post-selected rate is slightly greater than the expected probabilistic rate, within the error. This is very promising for the active demultiplexing scheme as the calculated rate for the probabilistic assumes completely lossless transmission.

5.5 Conclusion

In this chapter a novel scheme for single-photon demultiplexing was presented and discussed. An optical setup was built to realize the scheme and its components were characterized.

Photons from an efficient QD was utilized to demonstrate the demultiplexing capabilities of the scheme. The high single-photon count rate made it feasible to obtain a 3-fold single-photon state.

Demultiplexed photons were detected and their mutual correlations were measured. From the correlation measurements a 3-fold single-photon rate of $\Gamma_{3-\text{fold}} = 0.45 \pm 0.027\,\text{Hz}$ was extracted. It was discovered that a systematic loss mechanism caused the majority of events to not be recorded, which greatly diminished the extracted 3-fold single-photon rate. By post-selecting on the time intervals where events had been recorded, a 3-fold single-photon rate of $\Gamma_{3-\text{fold}}^{\text{Post}-\text{Sel}} = 2.03 \pm 0.49\,\text{Hz}$ was estimated. This rate showed that the concept of active demultiplexing is a viable alternative to probabilistic demultiplexing.

Several loss mechanisms were identified, both in the optical setup and in the switching process. By improving these mechanisms the overall efficiency of the process will be improved. With such improvements the active single-photon demultiplexing can become a resource for preparing N-fold single-photon states for optical quantum computing.

Chapter 6

On-chip beamsplitter with single-photons

Optical quantum information processing requires an efficient source of photonic qubits. Solid-state QDs in photonic structures have recently shown single-photon emission with high purity and indistinguishability, which opens up new routes towards scalable quantum networks [36, 37, 135].

To date the best results for single-photon emission have been observed on micropillar structures [92, 91], however in these experiments the source brightness is limited by inefficient outcoupling. A route to circumvent outcoupling losses is to integrate all optical components on the chip containing the QD. Integrating the optical elements has several benefits besides circumventing outcoupling losses, e.g. more compact systems and optical mode overlaps that are stable over long time scales.

A fundamental component of any optical system is the beamsplitter, which is used to combine or split multiple optical modes. In the quantum regime the four port beamsplitter is described by the unitary transformation [133]:

$$\hat{U}_{\mathrm{BS}} = \begin{pmatrix} t^* & r \\ r^* & t \end{pmatrix}. \tag{6.1}$$

The unitarity of the transformation requires that $|r|^2 + |t|^2 = 1$. For a 50:50 beamsplitter the transformation is:

$$\hat{U}_{\mathrm{50:50\ BS}} = \frac{1}{\sqrt{2}} \begin{pmatrix} 1 & i \\ i & 1 \end{pmatrix}. \tag{6.2}$$

The transformation shows that the reflected and transmitted part is $\pi/2$ out-of-phase.

An on-chip beamsplitter is achieved with directional [136] or multimode interference(MMI) couplers [137]. These structures have been developed for integrated photonic circuits in the context of classical information processing. Recently, the interest for integrated beamsplitter has moved in the quantum domain, using non-classical light sources [138, 67, 139]. Experiments involving single-photons emitted from QDs and integrated beamspliiter are usually carried out in a configuration where the source is located off-chip, leading to large in-coupling losses. Such losses are avoidable by integrating the source on the same chip as the beamsplitter.

Recently directional couplers with embedded QD have been demonstrated [45, 140, 141]. These

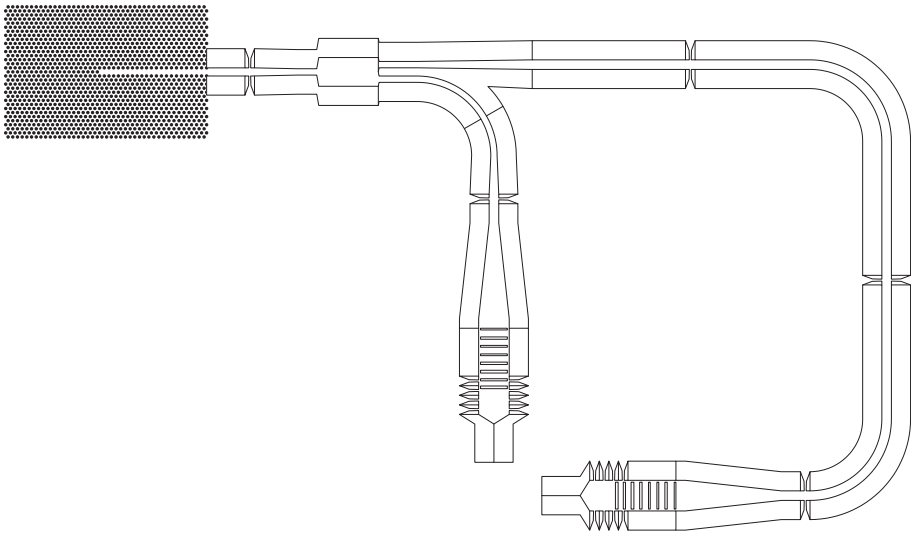

Figure 6.1: Sketch of the photonic structure. A photonic crystal waveguide is terminated in a photonic mirror to enhance the signal. The unterminated end is connected to a single-mode waveguide, which is coupled to a MMI power divider. The two outputs of the power divider is connected to efficient outcoupling gratings. The two outcoupling gratings are rotated $\pi/2$ relative, which causes their far-field patterns to have orthogonal polarization.

demonstrations show that the non-classical photon statistic of a single-photon source can be observed using integrated photonic beamsplitters.

In this chapter a platform for integrating an efficient source of single-photons with a MMI beamsplitter is discussed and demonstrated. The FEM simulation in Fig. 6.3(b) was performed by Leonardo Midolo and the FEM simulation in Fig. 6.4 (b) was performed by Moritz Matthiae.

6.1 The Circuit

A sketch of the circuit is shown in Fig. 6.1. QDs are embedded inside a photonic crystal waveguide, which is terminated by a photonic mirror in one end. The combination of a QD and a photonic crystal waveguide constitutes an efficient light-matter interface, and coupling efficiencies of $\beta > 98\%$ are experimentally obtainable [42], making this system a solid foundation for building an efficient quantum circuit upon.

The unterminated end of the photonic crystal waveguide is coupled to a single-mode waveguide. The single-mode waveguide is then interfaced with various structures such as beamsplitters or outcoupling gratings. By interfacing photonic crystal waveguides with rectangular single-mode waveguides, low-loss transmission of single-photons is possible. In photonic crystals fabrication defects lead to scattering losses and localization [111], these effects lower the overall transmission and therefore makes photonic crystal waveguides unsuitable for routing of single-photons.

The single-mode waveguide is connected to a MMI $-3\,\mathrm{dB}$ power divider and the outputs of the MMI is coupled to efficient outcoupling gratings. The MMI power divider and the efficient outcoupling gratings are discussed in detail below.

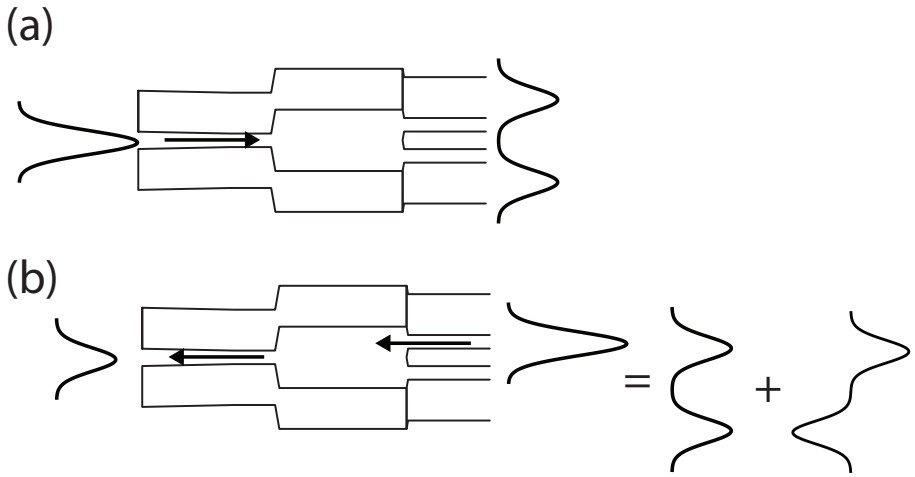

Figure 6.2: **a)** A sketch of the symmetric MMI coupler with a field propagating in the forward direction. The incoupled mode couples to the symmetric modes of the MMI coupler, which are coupled equal to the two outcoupling single-mode waveguides, thereby facilitating a 1x2 MMI power splitter. **b)** A sketch of the MMI coupler with a field propagating in the reverse direction through the MMI section. The mode in the single-mode waveguide is decomposed into a symmetric and anti-symmetric mode. By construction of the restricted interference, only the symmetric mode couples to the output single-mode waveguide. As the symmetric mode constitutes half of the incoupled mode half the intensity is not recovered in the single-mode waveguide.

Multimode interference beamsplitter

In Fig. 6.2 (a) a sketch of the MMI beamsplitter is shown. The structure has one input and two outputs, which consist of single mode waveguides.

The MMI structure is based on multimode interference [137]. The fundamental operation principle is self imaging in a multimode optical waveguide, where the input field profile is retrieved at a single or multiple points at periodic spacing along the waveguide [142].

The width of the MMI section is chosen to support several modes at the design wavelength, this ensures that multimode interference can occur. The following theory is based on Ref. [137]. Assuming a stepindex waveguide as seen in figure 6.2 (a), the needed dimension for the waveguide is calculated using analysis of the propagation constant. The propagation constant β_ν is found as:

$$\beta_\nu = \frac{2\pi}{\lambda_0} n_e - \frac{(\nu+1)^2 \pi \lambda_0}{4 n_e W_e^2}. \tag{6.3}$$

Here λ_0 is the free-space design wavelength, n_e is the effective refractive index of the waveguide, ν is the mode number and W_e is the effective width of the fundamental mode, which is related to the width of the waveguide.

From the propagation constant the beat length is calculated as:

$$L_\pi = \frac{\pi}{\beta_0 - \beta_1} \simeq \frac{4 n_e W_e^2}{3\lambda_0}. \tag{6.4}$$

The spacing between the fundamental mode and any mode is given by $(\beta_0 - \beta_\nu) \simeq \frac{\nu(\nu+2)\pi}{3L_\pi}$.

To describe the propagation in the multi-mode section, it is convenient to express the input field

$\Psi(y,z)$ as a superposition of all guided modes:

$$\Psi(y,x) = \sum_{\nu=0}^{m-1} c_\nu \psi_\nu(y) e^{i(\beta_0-\beta_\nu)x}. \tag{6.5}$$

The resulting field profile after propagating a distance L, is:

$$\Psi(y,L) = \sum_{\nu=0}^{m-1} c_\nu \psi_\nu(y) e^{i\frac{\nu(\nu+2)\pi}{3L_\pi}L}. \tag{6.6}$$

In the above expression, the phase accumulated by each mode is a multiple of π whenever the condition $L = \frac{3p}{2}L_\pi$ with $p = 1,3,5,...$ is fulfilled. This yields:

$$\Psi(y,\frac{3p}{2}L_\pi) = \sum_{\nu=0}^{m-1} c_\nu \psi_\nu(y) e^{ip\frac{\pi}{2}\nu(\nu+2)}. \tag{6.7}$$

By utilizing that for even modes $\psi(-y) = \psi(y)$ and for odd modes $\psi(-y) = -\psi(y)$ the mode is decomposed into:

$$\begin{aligned}\Psi(y,\frac{3p}{2}L_\pi) = &\sum_{\nu=0,2,4...} c_\nu\psi_\nu(y) + \sum_{\nu=1,3,5...}(-i)^p c_\nu\psi_\nu(y) = \\ &\frac{1+(-i)^p}{2}\Psi(y,0) + \frac{1-(-i)^p}{2}\Psi(-y,0).\end{aligned} \tag{6.8}$$

This is a pair of images of the initial field whose amplitudes are $1/\sqrt{2}$ of the initial field and the two images are $\pi/2$ out of phase. The structure thereby reproduces the behavior of the ideal beamsplitter. By terminating the multi-mode section at these specific lengths and introducing two single-mode waveguides, a 3 dB beamsplitter is obtained.

If only the even modes of the MMI-section are excited a 1xN power divider is devised, where the beating length for N output modes is given by:

$$L = \frac{3pL_\pi}{4N} = \frac{pn_eW_e^2}{N\lambda_0}. \tag{6.9}$$

To excite the even modes of the MMI coupler, the incoupling single-mode waveguide is placed in the symmetry point of the coupler. A sketch of the symmetric MMI power splitter is shown in Fig. 6.2 (a) with an input field propagating in the forward direction. As only the even modes are considered, the modes are symmetric and there is no longer any phase difference between the self-images. A structure with restricted interference is therefore not able to reproduce the behavior of an ideal beamsplitter.

The missing fourth port of the device is by construction a dissipation channel of the structure and cannot be collected by waveguides. The missing fourth port also breaks the reversible nature of a beamsplitter, as seen in Fig. 6.2 (b) a mode propagating in port 2 is decomposed in an even and odd mode, only the even mode couples to waveguide 1 and the coupling is -3 dB [143]. If the fourth port of the MMI structure is addressed an unitary beamsplitter is achievable. The anti-symmetric mode is lost through radiation to other modes.

A SEM image of a fabricated 1x2 MMI power splitter with a single-mode waveguide input and two single-mode waveguides as outputs.

Fig. 6.3 (b) shows a FEM simulation of an optical field propagating in a single mode waveguide coupled to a 1x2 MMI power splitter. The waveguide width is $W = 1.5\,\mu$m and the length of the multimode section is $L = 3.4\,\mu$m. The output field is coupled into two single mode waveguides that

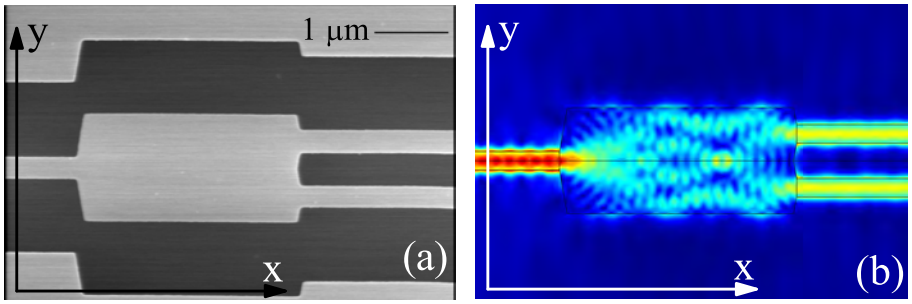

Figure 6.3: **a**) SEM image of the MMI beamsplitter seen from above. The structure consists of a single mode waveguide connected to a MMI waveguide beamsplitter that is terminated in two single mode waveguides. The input and the outputs of the MMI are ridge waveguides which guides the light with low losses.**b)** FEM simulation of a symmetric 3db MMI beamsplitter. An electric field is launched in the input single mode waveguide. As the electric field enters the MMI waveguide, the field couples to higher order modes. As the field propagates across the MMI waveguides the modes interfere. By terminating the MMI waveguide after $L = 3.4\,\mu$m and coupling into single mode waveguide, the power into each waveguide $-3.13\,$dB of the incident power.

are placed 760 nm of center, which maximizes the incoupling. The calculated power in each arm is $-3.13\,$dB, which is an even splitting ratio of 48.67% in each arm, meaning that the MMI beamsplitter has a theoretical efficiency of $\sim 97\%$. A negligible part of the loss stems from back reflection into the input waveguide, while the main loss arises from the transition between the waveguides of different widths.

Fig. 6.3 (b) shows that there are multiple self-images visible along the multimode section of the waveguide. These selfimages are understood from Eq. (6.9), where it is shown that when N is increased the length of the waveguide is shortened. As N is increased, the width of the MMI waveguide also has to be increased in order to be able to separate the modes and couple them into individual single mode waveguides.

Outcoupling grating

To excite the sample and collect the emission using the same microscope objective, it is necessary to scatter light out of the chip, which is achieved using a second order Bragg grating [112]. However these gratings cause the electric field profile to deviate from a Gaussian, thereby reducing the incoupling into a single mode fiber.

To improve the efficiency of the outcoupling a new grating is designed. The requirements for the grating are:

- The outcoupled mode has a Gaussian mode shape
- The mode diameter matches the spot size of the collection fiber
- Light is scattered out-of-plane with near-unity efficiency

A grating structure that fulfills all the above requirements and is possible to implement in suspended membranes, has been proposed in Ref. [144]. If the pitch of the trenches is $\Lambda = \frac{\lambda_0}{n_{\text{eff}}}$ there is

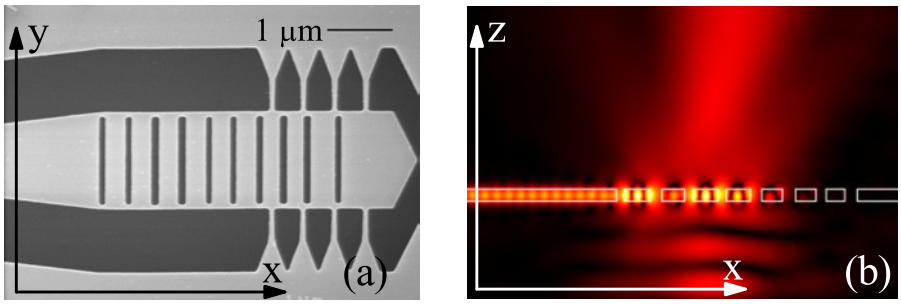

Figure 6.4: **a)** SEM image of the optimized outcoupling grating. **b)** FEM simulation of the outcoupling grating as viewed from the side. An electric field is propagating in the waveguide from the left. The trenches in the membrane cause the field to be scattered out of the membrane, both up and down. A substrate below the membrane causes a reflection upwards. The transmission through the waveguide is completely suppressed. The field above the membrane is at an angle with respect to the normal of the membrane.

scattering out of the membrane and thereby towards the microscope objective. Such a grating causes the emission to propagate at the normal of the membrane, but also causes a second-order diffraction process that reflects the light back into the waveguide. In order to avoid this backreflection the pitch of the grating is modified to scatter the light at an angle compared to the normal. Simulations and characterization of the outcoupling gratings is found in Ref. [145].

Using a genetic algorithm the grating is optimized. By varying the width of the trenches the outcoupling efficency is optimized by maximizing the overlap of the scattered light field with a Gaussian mode. The minimum trench width is bound to $w_{\text{trench}} > 100\,\text{nm}$, to ensure that the trench is etched through, while the egdes being vertical. The genetic algorithm converges on a design that yields a theoretical coupling efficiency of 0.65% and a bandwidth of 15 nm. The grating is etched into a waveguide that is significantly wider than the single mode waveguide used for propagating the light in the membrane. The width of the increased waveguide $w = 1.6\,\mu\text{m}$ is determined to ensure a Gaussian shape of the mode scattered out of plane, with a full width half max (FWHM) of $1.1\,\mu\text{m}$, which matches the spot size of a $NA = 0.85$ objective.

As seen in Fig. 6.4 (a) the increase in waveguide width happens gradually. This is done to avoid that the fundamental mode of the waveguide couples to the higher order modes, which occurs if the change is too drastic. Instead the width of the waveguide is adiabatically changed, and in this way the intensity is preserved in the desired fundamental mode. The rate of change is bound by the adiabatic criteria $\frac{\Delta w}{\Delta x} \leq \frac{\lambda}{n w_0}$, where w_0 is the initial width [115]. As the single mode waveguide witdth is $w_{\text{wg}} = 320\,\text{nm}$, the corresponding taper length is $\Delta x = 7.7\,\mu\text{m}$.

Simulations show that the transmission of the adiabatic taper increases with a square root dependence on the length of the taper that saturates at $\Delta x = 7.7\,\mu\text{m}$. This means that shorter taper length is usable with only a slight transmission penalty [145].

The far-field of the light scattering from the grating is linearly polarized and given by the orientation of the grating. Two gratings rotated by $\pi/2$ with respect to each other have orthogonal polarized far-field polarization, it is therefore possible to distinguish between the two gratings using

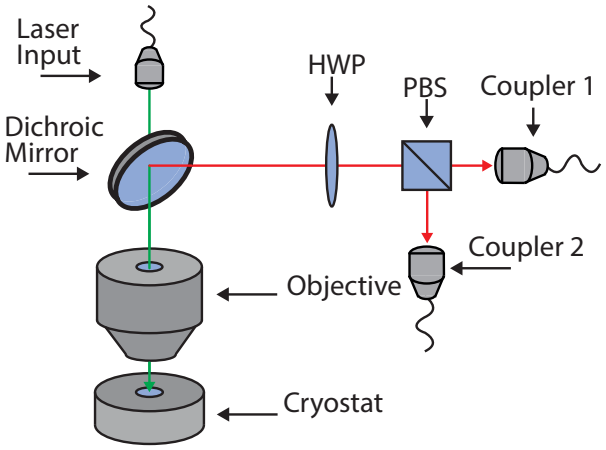

Figure 6.5: Schematic representation of the experimental setup. The excitation laser is coupled out from the laser input and collimated. It is transmitted through a dichroic mirror with a cutoff wavelength of $\lambda_{\text{laser}} = 875\,\text{nm}$. After the dichroic mirror, the excitation laser is focused using a microscope objective. The sample is mounted inside a flow He cryostat. The photoluminescence from the sample is collected using the microscope objective and sent to the dichroic mirror. If the wavelength of the emission is above the cutoff wavelength of the dichroic mirror it is reflected. The reflected part of the emission is sent through a HWP and a PBS. The HWP is used to match the polarization axis of the sample to the axis of the PBS. The PBS is used to separate the two orthogonal polarizations originating from the sample. The photoluminescence with orthogonal polarization is then coupled into respective fibers for detection.

the polarization.

6.2 Experimental setup

The sample containing QDs and waveguides is mounted in a liquid helium flow cryostat. The sample is optical accessible through a window from the top and a microscope objective is used to focus the excitation laser onto the sample and for collecting the emission. In order to separate the excitation laser and the emission, a dichroic mirror is used in a confocal setup, thereby making it possible to excite the sample in one spot and collect the emission from two separate spatial positions. The dichroic mirror has a cutoff wavelength at $\lambda_{\text{cutoff}} = 875\,\text{nm}$ and any emission above λ_{cutoff} is reflected by the dichroic mirror.

The emission above the dichroic cutoff wavelength is sent to a halfwave plate(HWP) followed by polarizing beamsplitter(PBS). The PBS is used to separate the two polarization axes of the emission. The HWP serves to align the polarization axes of the sample to the PBS. After the polarization axes are spatially separated by the PBS, the emission is coupled into single mode fibers for detection.

The optical fiber guiding the emission is coupled to a spectrometer, where a spectrum is recorded by a CCD camera. Alternatively the emission is sent to a grating setup for single-photon measurements. The grating setup suppresses the emission from the sample, except the emission line of interest. By coupling the filtered emission into a fiberbased beamsplitter, photon correlation measurements are performed using fibercoupled APDs. For cross correlation measurements two identical filter setups

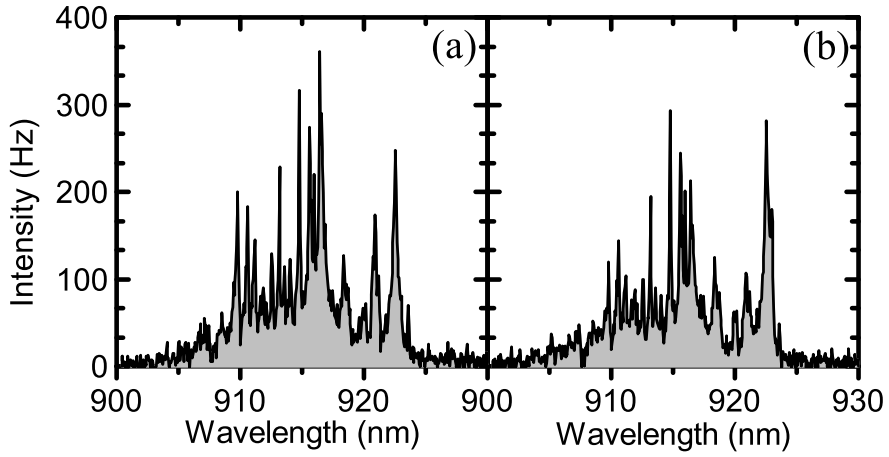

Figure 6.6: Emission spectrum from **a)** outcoupler 1 **b)** outcoupler 2. The sample is excited at $\lambda_{\text{laser}} = 800\,\text{nm}$ at saturation. In each spectrum single emission lines are visible. The intensity of the emission line at 914.9 nm is comparable in both the spectra. The photonic band gap of the photonic crystal is at 925 nm and is identified by the suppression of QD emission above that wavelength.

are aligned to the frequency of the emission line of interest.

6.3 Photoluminescence

Spectra

Figure 6.6 (a-b) shows the emission spectra from the two orthogonal outcouplings gratings. The orientation of the gratings dictates the polarization of the emission and in the sample the outcoupling grating of the MMI outputs are always rotated $\pi/2$ with respect to each other. The two gratings are therefore distinguished by their polarization and the detected signal from both gratings is maximized by aligning the polarization axis of the sample to the PBS using the HWP.

The spectra shows that the excitation spot is aligned to the photonic crystal waveguide, as the lack of emission above 925 nm indicates that the photonic band gap suppresses these frequencies.

In each of the spectra individual emission lines are identified and it is seen that there are similar emission lines visible in each of the spectra, which is the first indication that the MMI beamsplitter is splitting the signal in two different paths. It is also seen that the intensity of the lines is not equal in each of the spectra and this indicates that the overall transmission is not perfectly balanced. It is not possible to estimate the splitting ratio of the beamsplitter itself based on the spectra, as there are several components that can induce variations. The discrepancy is likely due to fabrication imperfections in the outcoupling gratings, as small variations in the trench width causes a deviation from the theoretical outcoupling efficiency.

From the spectra there are indications that the splitting ratio is wavelength dependent. This dispersive behavior might be caused by the outcoupling gratings, previous measurements of these outcoupling gratings have shown that these are susceptible to fabrication variations and the outcoupling efficiency is strongly depending on the emission wavelength [145].

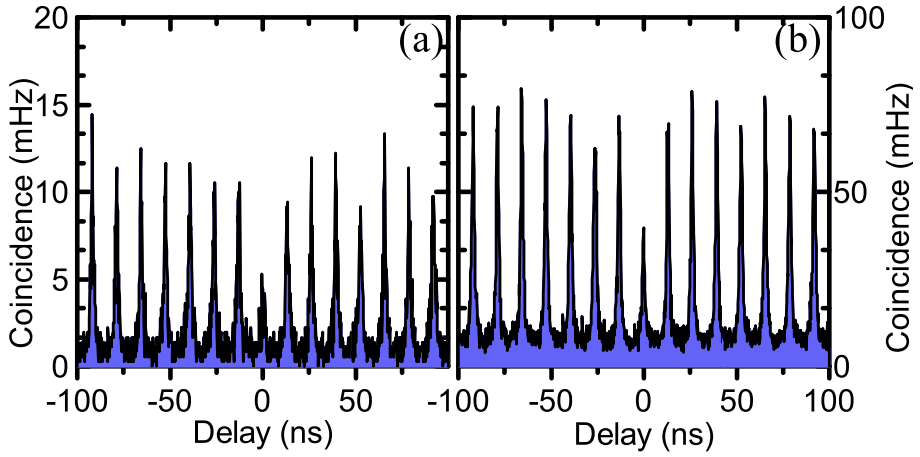

Figure 6.7: **a)** Autocorrelation measurement of the emission line at 914.9 nm. The sample is excited at $\lambda_{\text{laser}} = 800\,\text{nm}$ and at saturation. The peak at $\tau = 0$ is reduced compared to the side-peaks and the extracted value $g^{(2)}_{\text{auto}}(0) = 0.40 \pm 0.06$. **b)** Cross correlation measurement of the filtered emission in coupler 1 and coupler 2 under the same excitation conditions as the autocorrelation. The correlation at $\tau = 0$ is suppressed compared to the side peaks and normalized correlation function is extracted to $g^{(2)}_{\text{cross}}(0) = 0.48 \pm 0.03$.

Correlation measurements

The single-photon nature of the QD emission is determined by performing a cross-correlation measurement between the two outcoupling ports. The cross-correlation reveals whether an emission line observed in both spectra stems from the same QD.

A suitable candidate for such a measurement shows an intense emission line in both spectra and demonstrates some degree of single-photon purity, when conducting a HBT-measurement on the individual outcoupling ports. The need for an efficient outcoupling from both arms simultaneously is obvious, as a strong signal is required for the cross-correlation. Single-photon purity of the emission line is necessary to demonstrate an anticorrelation in the crosscorrelation measurement. The emission line at 914.9 nm has equal and high intensity in both spectra and therefore fulfills the first requirement.

In Fig. 6.7 (a) the autocorrelation of the emission line at 914.9 nm is shown, this measurement is obtained by coupling the output of the grating setup to a fiberbased beamsplitter and measure the correlations of the outputs. The reduced peak at $\tau = 0$ demonstrates a single-photon nature and the value is extracted to $g^{(2)}_{\text{auto}}(0) = 0.40 \pm 0.06$.

In Fig. 6.7 (b) the result of the cross-correlation between the two outcoupling gratings is shown. A suppression of the central peak is observed and a $g^{(2)}_{\text{cross}}(0) = 0.46 \pm 0.03$ is extracted. The extracted value of the cross correlation is on the order of the autocorrelation. This is the expected behavior as the excitation conditions for the two measurements are kept constant.

When conducting the cross-correlation the fiberbased beamsplitter is excluded, resulting in a doubling of the measured intensity at the same excitation power, causing a four fold increase in the coincidence counts measured at the same excitation power and integration time. This increase is reflected in Fig. 6.7 (b) compared to Fig. 6.7 (a).

The introduction of the fiberbased beamsplitter in the autocorrelation measurement does not alter

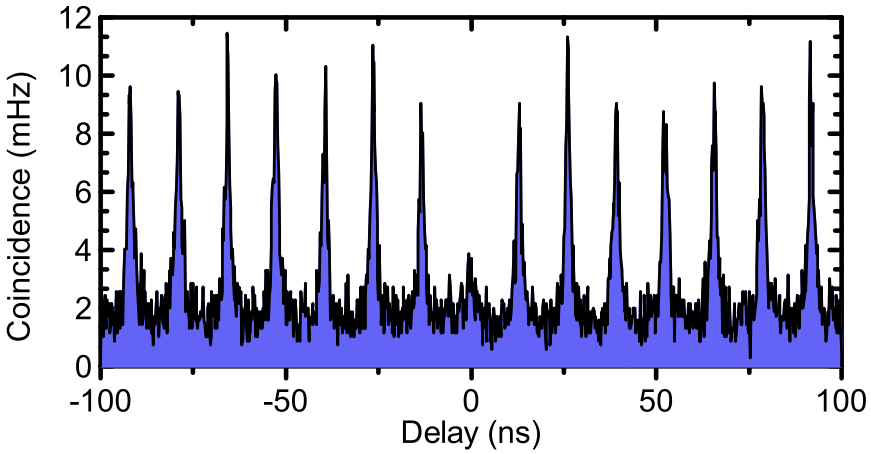

Figure 6.8: Cross-correlation measurement between the two outcoupling gratings of the filtered emission line at half the saturation power. The measurement exhibits a significantly reduced correlation at $g^{(2)}_{\text{cross}}(0) = 0.25 \pm 0.04$.

the result of the second order correlation, as linear loss does not change the correlation of the HBT. The photon statistic is therefore not expected to vary between the auto- and the cross correlation [113].

Due to the enhancement in intensity when performing a cross-correlation compared to the HBT, it is possible to halve the excitation power and still obtain sufficient statistics.

The excitation power is halved compared to the saturation power used in the previous measurements and a cross-correlation between the outcoupling ports is then conducted at these excitation conditions. Fig. 6.8 shows the unnormalized second order correlation of the cross-correlation, the value of the suppressed peak at $\tau = 0$ is extracted to $g^{(2)}_{\text{cross}}(0) = 0.25 \pm 0.04$.

The further reduced value of the $g^{(2)}_{\text{cross}}(0)$ confirms that the emission detected emanates from a single-photon source. Furthermore it demonstrates that the emission detected in the two output ports stems from the same QD. This demonstrates that the MMI beamsplitter is an on-chip beamsplitter and integration with single-photon emitters is possible.

6.4 Conclusion

In this chapter, it was demonstrated that QDs in photonic crystal waveguides can be interfaced with an on-chip beamsplitter to create complex circuits with single-photon sources.

The spectra of the emission from the outputs of the on-chip beamsplitter indicated that the emission from the QD was being split by the MMI beamsplitter.

An antibunching of $g^{(2)}_{\text{auto}}(0) = 0.40 \pm 0.06$ in the photon statistics proved that the emission consisted of single-photons. By performing a crosscorrelation between the beamsplitter outputs, it was found that the intensity was split by the device. An extracted $g^{(2)}_{\text{cross}}(0) = 0.46 \pm 0.03$ demonstrated that the QD was coupled to the beamsplitter. By reducing the excitation power the correlation was reduced futher to $g^{(2)}_{\text{cross}}(0) = 0.25 \pm 0.04$.

Transmission measurements on MMI beamsplitters not containing QDs could provide statistics on the efficiency and expected splitting ratio. Also active micro electro-mechanical system might provide

the possibility of reconfigurable networks, based on the same platform.

The findings in this chapter show that MMI beamsplitters are a viable platform for efficient and compact single-photon systems.

Chapter 7

Generation of entanglement with single-photons from quantum-dots

An efficient single-photon source has many potential applications in quantum information processing. For instance, implementation in boson sampling [120] and quantum chemistry [64]. A QD embedded in a photonic structure is an efficient resource of single photons with a high single-photon purity and indistinguishability [92, 101, 91]. Although an excellent resource of photonic qubits, the single photons emitted from the QD ground state exciton are not entangled.

Entangled single-photons have exciting prospects within fundamental research and practical applications. Entangled pairs have been used to demonstrate violations of Bell's inequality, where correlations due to entanglement in polarization were to be incompatible with a classical hidden variable theory [49]. The violation of Bell's inequality demonstrates the quantum mechanical nature of entanglement [146]. Using a resource of entangled qubits it is possible to generate secure cryptographic keys in quantum key distribution [147, 148]. By employing entangled qubits, the action of an eavesdropper is detected if the correlations do not violate Bell's inequalities. These qubits are then discarded from the key and no information is obtained by the eavesdropper.

Entangled states are also potentially a resource for efficient one-way quantum computing [59]. By measuring physical qubits sharing an entangled state in a specific pattern, a universal set of quantum gates is performed on virtual computational qubits, the value of the virtual computational qubits is then read-out by measuring the last remaining physical qubits in the state.

One method of generating entangled single-photon pairs is through SPDC, where single-photon pairs with parallel polarization are created during type-I SPDC [149]. Scalable single-photon production using SPDC is limited due to the probabilistic nature of the single-photon generation.

A potential method for efficient entangled single-photon pair generation is to utilize the cascaded emission of a QD biexciton state, which consists of two exciton pairs. Through the cascaded process the emitted photons show polarization correlations [150] and emission of entangled photon pairs is achieved [60, 61, 151]. A QD is prepared in the biexciton state through a cascaded decay after being excited above the bandgap. The biexciton has two radiative decay paths as either of the electron-hole pairs can decay, the radiative decay of the biexciton deterministically prepares the exciton according to the polarization of the photon emitted from the biexciton state. The polarization of the photons emitted by the biexciton and exciton is thereby interlocked.

Due to the fine-structure splitting of the exciton states, the which-path information revealed by the emission energy of the photons must be eliminated through filtering in order to demonstrate entanglement. Alternatively it is possible to eliminate the fine-structure splitting through the quantum Stark effect and erase the which-path information [152].

The non-resonant preparation of the biexciton and the subsequent cascaded decay acts as a dephasing process expected to reduce the photon coherence. To generate entangled photon pairs, while demonstrating single-photon indistinguishability, a two-photon resonance is utilized to resonantly prepare the biexciton state [125]. An entangled pair of single-photons is emitted and the photon emitted from the exciton (biexciton) state is indistinguishable with an exciton (biexciton) photon emitted in a subsequent pulse.

Although a polarization entangled photon pair with coherent single-photons is achieved, the photons of the entangled pair are not indistinguishable as the exciton and biexciton energies are split by the exciton binding energy [83]. Any interference between the exciton and biexciton photons of the entangled pair is therefore not possible. Entangled single-photon pairs, where the members of the pair are indistinguishable single-photons can be generated using SPDC [153].

A proposal to generate entangled states of arbitrary length, by utilizing the four-level system of the charge exciton trion state of a QD, is found in Ref. [62]. The negative trion state is generated by charging the QD with a single electron spin, which constitutes a four-level system with two excited states with $J_z = \pm\frac{3}{2}$ and two ground states with $J_z = \pm\frac{1}{2}$. If the trion is excited by a π-pulse, the spin of the excited state is locked to the initial state, as is the polarization of the emitted photon. If the electronic spin of the ground state is initialized in a superposition by a $\pi/2$-pulse, a π-pulse and the subsequent photon emission leaves the electronic spin and the photon polarization in an entangled state. A pulse sequence of $\pi/2$-pulse and π-pulse is continuously applied to generate an entangled state of arbitrary length. The length of the generated state is limited by the coherence time of the electronic spin.

A third method for generating entanglement between single-photons is through measurement. By interfering single-photons and detecting successful entangling events, the system state is collapsed onto an entangled state. The generation of entanglement is heralded by the detection event and is therefore event-ready. An entanglement scheme, with detection of single-photons was used to generate event-ready entanglement between distant electronic spins. The entangled system demonstrated loophole-free violation of Bell's inequalities [154].

In this chapter an event-ready scheme for generating entanglement between indistinguishable single-photons is presented and discussed. It is discussed how single-photons from a QD can be used as resource of entangled photons.

First part of the discussion concerns how entangled states can perform one-way quantum computations. Secondly, a setup to generate an entangled state from indistinguishable single-photons is presented and discussed. Thirdly, it is discussed how an entangled state is verified. And finally the source of single-photons is presented and characterized.

The work presented in this chapter was performed in close collaboration with the Quantum Technology group at University of Queensland.The data for Fig. 7.8 was provided by Juan Loredo and Marcelo de Almeida. The theory outlined in Sec. 7.2 is supplied by Nicolás Quesada in Ref. [155].

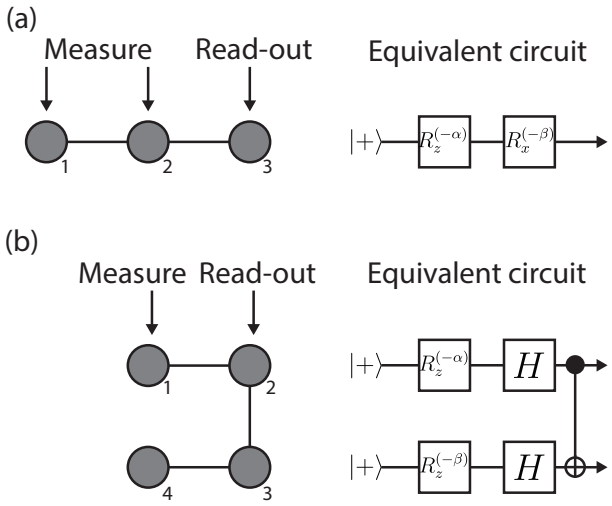

Figure 7.1: **a)** Linear three qubit cluster state and the equivalent quantum computation circuit. By measuring qubit 1 and 2, single-qubit rotations are performed on the computational qubit, which is read-out by measuring qubit 3. **b)** Two dimensional horseshoe cluster state $|\phi_{\supset 4}\rangle$ and the equivalent quantum computation circuit. By measuring qubit 1 and 4 single-qubit rotations $R_z^{(-\alpha)}$, a Hadamard gate H and a two-qubit CNOT operation is performed. The result is extracted by measuring qubit 2 and 3.

7.1 A one-way quantum computer

Optical quantum computing is currently limited by the probabilistic nature of LOQC or the absences of strong nonlinearities needed to perform deterministic quantum computing. To circumvent these challenges, entangled states, called cluster states, are utilized to perform quantum computation [156]. The advantage of cluster states is that only single-photon rotation and detection is required. As the computation is performed by detecting single-photons, the process is irreversible and is therefore termed a one-way quantum computer.

A one-way computer was demonstrated using single-photons from a SPDC source, where a four-fold single-photon cluster state was generated and verified through state tomography [157]. By performing single-photon rotations and measurements, Grovers search algorithm was implemented in the one-way computer.

Cluster states and quantum computation

The quantum computation is performed on computational qubits and the result is imprinted onto the computational qubits. A single computational qubit consists of several entangled physical qubits. By performing measurements on the physical qubits, operations are applied to the computational qubits.

A linear cluster state represents a single computational qubit, the linear cluster state seen in Fig. 7.1 (a) consists of three entangled physical qubits, which in combination constitutes a single computational qubit.

Two qubits are required to generate a cluster state. Preparing the two qubits in a superposition and performing a controlled phase operation results in an entangled state. Finally, the cluster state

is then expanded by performing this process with additional qubits.

The computational qubits are represented in the computational basis $\{|0\rangle, |1\rangle\}$, which can be mapped to any possible degree of freedom of the physical qubits. By measuring a physical qubit in the computational basis, it becomes disentangled from the cluster state, which is used to modify an arbitrary cluster state to a desired structure.

Single qubit rotations are applied to the computational qubit by measuring a physical qubit in the measurement basis $B_j(\alpha) = \{|+\alpha\rangle_j, |-\alpha\rangle_j\}$ with $|\pm\alpha\rangle = \frac{1}{\sqrt{2}}(|0\rangle \pm e^{i\alpha}|1\rangle)$, where α is a real number defining the angle of rotation. If the qubits are polarization encoded single-photons, this is achieved using a HWP and a PBS in front of a single-photon detector. An example of a three qubit linear cluster state is [157]:

$$|\Phi_{\text{lin3}}\rangle = \frac{1}{\sqrt{2}}\left[|+\rangle_1|0\rangle_2|+\rangle_3 + |-\rangle_1|1\rangle_2|-\rangle_3\right]. \tag{7.1}$$

Where the physical qubit $|+\rangle_i$ is prepared in the superposition $|\pm\rangle_i = \frac{1}{\sqrt{2}}|0\rangle_i \pm |1\rangle_i$. By writing the physical qubits in terms of the measurement basis, the state is:

$$\begin{aligned}|\Phi_{\text{lin3}}\rangle = \frac{1}{2}\left[|\alpha\rangle_1|\beta\rangle_2 R_z(-\alpha)R_x(-\beta)|+\rangle_3 + |\alpha\rangle_1|-\beta\rangle R_z(\alpha)R_x(-\beta)|+\rangle_3\right.\\ \left.+|-\alpha\rangle_1|\beta\rangle_2 R_z(-\alpha)R_x(\beta)|-\rangle_3 + |-\alpha\rangle_1|-\beta\rangle_2 R_z(\alpha)R_x(\beta)|-\rangle_3\right].\end{aligned} \tag{7.2}$$

Eq. (7.2) demonstrates that by measuring qubit 1 (2) in state $|\alpha\rangle$ ($|\beta\rangle$) performs a rotation of the computational qubit around the z(x)-axis of the Bloch's sphere $R_z(\alpha) = e^{-i\alpha\sigma_z/2}$ ($R_x(\beta) = e^{-i\beta\sigma_x/2}$) and imprints the result on the third qubit of the cluster state. By measuring qubit 3, the result of the computation is read-out, see Appendix A for full details.

Universal quantum computation requires a CNOT operation, which is implemented by the horseshoe cluster state in Fig. 7.1 (b). The horseshoe cluster state is described by the entangled state [157]:

$$|\phi_{\supset 4}\rangle = \frac{1}{2}[|0\rangle_1|+\rangle_2|0\rangle_3|+\rangle_4 + |0\rangle_1|-\rangle_2|1\rangle_3|-\rangle_4 + |1\rangle_1|-\rangle_2|0\rangle_3|+\rangle_4 + |1\rangle_1|+\rangle_2|1\rangle_3|-\rangle_4]. \tag{7.3}$$

By measuring qubit 1 and 4 single qubit rotations $R_z^{(-\alpha)}$ and Hadamard gate $H = \frac{1}{\sqrt{2}}(\sigma_x + \sigma_z)$ are applied to the computational qubits before a CNOT operation.. The outcome of the operations is imprinted on qubit 2 and 3, which is read-out by measuring their qubit value.

By constructing a cluster state of sufficient size and shape it is possible to perform any computational operation and therefore universal quantum computing is achieved.

Computation using cluster states is advantageous, as erroneous rotation is detected if the outcome of the measurement is e.g. $|-\alpha\rangle$ when the desired outcome is $|\alpha\rangle$. Such error outcomes can be corrected using feedforward techniques [158].

Optical fusion gates

A one-way quantum computer using cluster states is an appealing route to quantum computing, due to the relaxed requirements on gate operation. To implement a scalable one-way computing requires efficient generation of arbitrary size cluster states.

Photonic cluster states are generated probabilistic by using linear optical elements, such as a beamsplitter. By interfering two indistinguishable single-photons in a polarization superposition, an entangled state is generated with a success probability of 50%, which limits the scalability. It is

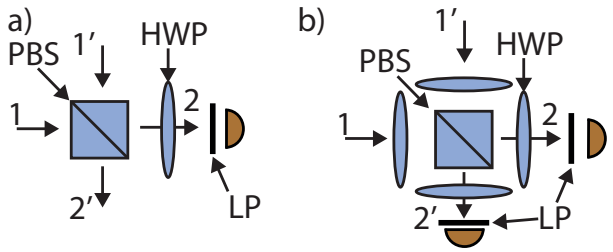

Figure 7.2: **a)** Type-I fusion gate. Two single-photons, both entangled in respective cluster states, are sent on the PBS port 1 and 1'. Photons in port 2 are rotated to the diagonal basis by a 45° HWP before being detected by a photon number and polarization discriminating detector. A successful fusion is heralded by the detection of a single-photon in port 2. **b)** Type-II fusion gate. Two single-photons entangled in respective cluster states, are sent in port 1 and 1'. Both inputs are rotated to the diagonal basis by 45° HWP. The photons are interfered on the PBS and the outputs are again rotated by HWP and detected by polarization discriminating single-photon detectors. A successful fusion is heralded by a detection event for both photodetectors.

possible to reduce the resource overhead by heralding on successful entangling events and recycle entangled states in the event of a failed event. These gates were proposed in Ref. [63] and are termed fusion gates.

In Fig. 7.2 two types of fusion gates are shown. The operation principle is based on single-photon interference and measurement. A successful or failed fusion event is heralded by the measurement outcome and the operation is therefore event-ready.

Fig. 7.2 (a) shows the type-I fusion gate, two photons are interfered on the PBS, with one output rotated using a half-waveplate (HWP) set to 45° and detected using a number and polarization discriminating detector. A successful fusion is heralded if a single-photon is detected and the fusion is failed if the outcome is zero or two photons.

If the two input qubits are part of respective entangled states, the successful operation outcome fuses the two qubits together into a single qubit, which inherits the bonds of the previous qubit and the result is a single cluster state consisting of the two previous separate cluster states.

Assuming the input of the Type-I fusion gate is two qubits, each a member of respective Bell states:

$$\begin{aligned}\mathcal{F}_I|\phi^+\rangle|\phi^+\rangle = \frac{1}{2}\mathcal{F}_I(|H_1H\rangle_{12}+|V_1V\rangle_{12})(|H_{1'}H\rangle_{12}+|V_{1'}V\rangle_{34}) \overset{\text{PBS}}{\rightarrow} \\ \frac{1}{2}(|H_2H\rangle+|V_{2'}V\rangle)(|H_{2'}H\rangle+|V_2V\rangle) \overset{\text{HWP}}{\rightarrow} \\ \frac{1}{2}\left(\frac{1}{\sqrt{2}}\left[|H_2H\rangle+|V_2H\rangle\right]+|V_{2'}V\rangle\right)\left(|H_{2'}H\rangle+\frac{1}{\sqrt{2}}\left[|V_2V\rangle-|H_2V\rangle\right]\right).\end{aligned} \tag{7.4}$$

If only successful fusion is considered, i.e. the cases where a single photon is detected in port 2:

$$\begin{aligned}\frac{1}{2}\left(\frac{1}{\sqrt{2}}\left[|H_2H\rangle+|V_2H\rangle\right]+|V_{2'}V\rangle\right)\left(|H_{2'}H\rangle+\frac{1}{\sqrt{2}}\left[|V_2V\rangle-|H_2V\rangle\right]\right) \overset{\Pi_1}{\rightarrow} \\ \frac{1}{\sqrt{8}}\left(|H_2H\rangle|H_{2'}H\rangle+|V_2H\rangle|H_{2'}H\rangle+|V_{2'}V\rangle|V_2V\rangle-|V_{2'}V\rangle|H_2V\rangle\right).\end{aligned} \tag{7.5}$$

The projected state is determined by the polarization of the detected photon:

$$\Pi_{V_2} : \frac{1}{\sqrt{8}}(|HHH\rangle + |VVV\rangle)\ \Pi_{H_2} : \frac{1}{\sqrt{8.}}(|HHH\rangle - |VVV\rangle) \tag{7.6}$$

Eq. (7.6) shows that the successful fusion of the two Bell states results in a combined cluster state with three qubits, which is the maximal entangled three qubit Greenberger-Horne-Zeilinger(GHZ) state [159]. Eq. (7.6) also shows that a successful outcome is expected in 50% of events.

A failed fusion attempt disentangles the qubits from their respective cluster states and reduces the length of the cluster states. As a failed Type-I fusion does not disentangle the full cluster state, the remaining state can be recycled thereby reducing the overhead. Type-I fusion is an efficient way of joining linear cluster states at the end qubits, but is an inefficient method for fusing two qubits enclosed in their respective cluster states, as a failed fusion operation results in a severed cluster state.

A more efficient method to fuse central qubits is the type-II fusion gate, shown in Fig. 7.2 (b), the photons on each input are rotated by a HWP at 45° before being interfered on the PBS, the outputs are rotated by HWPs and the photons are detected by polarization discriminating detectors. A successful fusion event is heralded by the detection of a photon in each output. The combination of the HWPs and PBS is called a rotated PBS (RPBS).

A failed Type-II fusion does not sever the two cluster states, but instead removes the qubit and reduces the state length, making it possible to recycle the cluster states.

A successful Type-II fusion removes a qubit from each cluster state and is more efficient than Type-I fusion when fusing large cluster states.

7.2 Bell pairs from indistinguishable single-photons

The two types of fusion gates presented above both require the input states to be an entangled state, in order to generate an expanded cluster state. The single-photons emitted by the QD exciton are not entangled a priori and are not immediately suitable as a resource for cluster state generation. By combining the Type-I and Type-II fusion gates, event-ready generation of Bell state pairs from four indistinguishable single-photons is achieved [160]..

Theory

Fig. 7.3 shows the optical setup for the generation of entanglement, which follows Ref. [160]. The four inputs are labeled $i = 1..4$, with each input containing a single-photon rotated to the diagonal state $|D\rangle_i = \frac{1}{\sqrt{2}}(|H\rangle_i + |V\rangle_i)$ and the input state is:

$$|\psi_{\mathrm{In}}\rangle = |D\rangle_1|D\rangle_2|D\rangle_3|D\rangle_4. \tag{7.7}$$

The photons in path 1 and 2 are interfered on PBS 1 and likewise for photons in path 3 and 4 on PBS 2. After the two initial PBS the system state is:

$$\begin{aligned}|\psi_{\mathrm{PBS}}\rangle = \frac{1}{4}\,&(|0\rangle_1|HV\rangle_2 + |HV\rangle_1|0\rangle_2 + |H\rangle_1|H\rangle_2 + |V\rangle_1|V\rangle_2)\otimes \\ &(|0\rangle_3|HV\rangle_4 + |HV\rangle_3|0\rangle_4 + |H\rangle_3|H\rangle_4 + |V\rangle_3|V\rangle_4)\,.\end{aligned} \tag{7.8}$$

The photons in path 2' and 3' are interfered on the RPBS, which is constructed by placing the HWP at 45° at input and outputs. The total state after the RPBS is extensive and cumbersome to calculate.

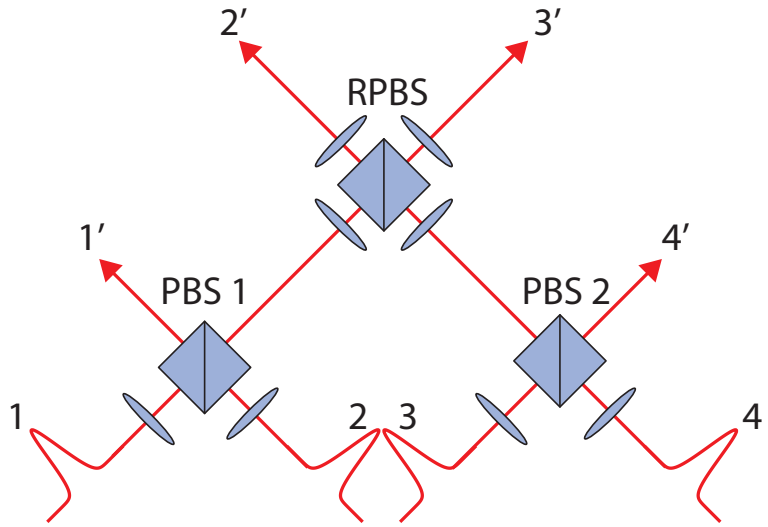

Figure 7.3: Sketch of the entangling gate. Each input contains a single-photon, HWPs in the inputs rotate the single-photons to the diagonal basis before the single-photons are interfered on the PBSs. Two paths are interfered on the RPBS, which is constructed by placing 45° HWPs on each the outputs of the third PBS.

Instead the state $|\psi_{\text{PBS}}\rangle$ can be separated into two regimes, states with single-photons in all paths or states with vacuum states and two photons states. If only terms with no vacuum is considered the state after the first PBS is:

$$|\psi^1_{\text{PBS}}\rangle = \frac{1}{4}(|H\rangle_1|H\rangle_2 + |V\rangle_1|V\rangle_2) \otimes (|H\rangle_3|H\rangle_4 + |V\rangle_3|V\rangle_4). \tag{7.9}$$

The state $|\psi^1_{\text{PBS}}\rangle$ can be rewritten in terms of the Bell states as:

$$|\psi^1_{\text{PBS}}\rangle = \frac{1}{4}\left(|\psi^+_{1,4}\rangle|\psi^+_{2,3}\rangle + |\psi^-_{1,4}\rangle|\psi^-_{2,3}\rangle + |\phi^+_{1,4}\rangle|\phi^+_{2,3}\rangle + |\phi^-_{1,4}\rangle|\phi^-_{2,3}\rangle\right). \tag{7.10}$$

Eq. (7.10) shows that the entanglement is swapped between the photons. The RPBS acts as a Bell state analyzer, which distinguishes between the two symmetric Bell states, i.e. a success probability of 50%. The reduced probability to distinguish the Bell states means that an event-ready entangled state is generated with a probability of $\frac{1}{8}$.

If the state with vacuum states and two-photons states is considered, the generation probability is increased to $\frac{3}{16}$ [160, 155].

The above calculation assumes completely indistinguishable photons, but if this is not the case the interference between the photons is reduced and the entangled state deteriorates. To examine the effect of partly distinguishable photons on the entangled pair, the initial state of the single-photons is $|D\rangle_i = \sqrt{1-\eta}|D\rangle_{i0} + \sqrt{\eta}|D\rangle_{ii}$, where the second index denotes the frequency of the photon, where 0 is the indistinguishable photon and i are distinguishable photons [161].

If the single-photons are partly distinguishable the concurrence C of the entangled pair is related to indistinguishability V through [155]:

$$\mathcal{C}(V) = \max[0, (2V^2 + V - 1)/2]. \tag{7.11}$$

The concurrence is plotted as a function of the indistinguishability in Fig. 7.4. As expected the entanglement of the generated pair is unity for fully indistinguishable photons. But as the indistin-

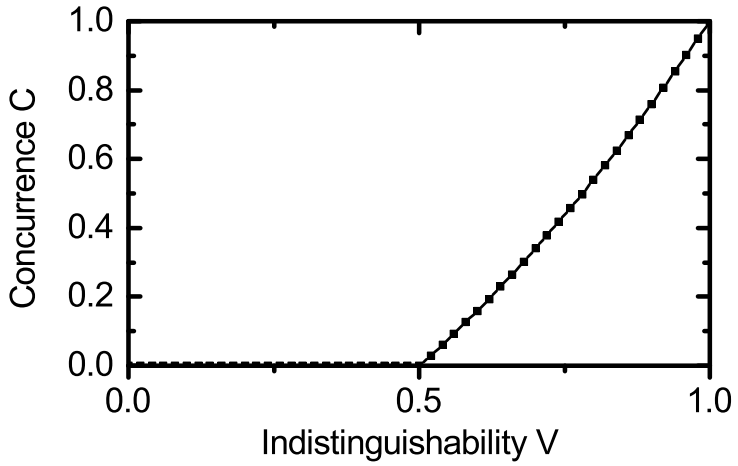

Figure 7.4: Theoretical curve for the concurrence of the generated Bell state as a function of the single-photon visibility. For $V < 0.5$ the concurrence of the Bell state is $\mathcal{C} = 0$, when $V > 0.5$ the concurrence rises first linearly and then quadratically until $\mathcal{C} = 1$ for $V = 1$.

guishability is reduced the concurrence is also decreased, until the indistinguishability reaches $V = 0.5$ where the concurrence is zero and the pair is no longer entangled.

Setup

The setup for event-ready entanglement generation shown in Fig. 7.3 was constructed at the Quantum Technology labatory at University of Queensland. Four single-photons are coupled into the setup through single-mode fibers, with the polarization of the single-photon being fixed by projecting it on a PBS on the input.

After the polarization projection no mirrors are used, as dielectric mirrors cause rotations of the polarization and thereby reduce the achieved interference. Although polarization maintaining, silver mirrors are unsuitable for single-photon application as the dissipation reduces the single-photon transmission.

The mode overlap of the single-photons is achieved by mounting the PBS on a manual rotation stage and on manual translation stage that displaces the PBS. The rotation stage controls the angle between the PBS and the beam. The stages provide the necessary degrees of freedom to obtain overlaps between the respective modes.

Using an intense C.W. laser at $\lambda = 920\,\text{nm}$ the optical paths of 1 and 3 are overlapped on the RPBS by rotating and displacing the RPBS. The two beams are overlapped in the near- and far-field using a CCD camera. With the two beams overlapped on the RPBS, the beams of path 1 and 2 are overlapped on PBS 1 using the same method, and likewise for path 3 and 4 on PBS 2.

After the beams are overlapped, the outputs of the RPBS are polarization projected onto PBSs and coupled into single mode fibers. The single-photons in path 1' and 4' are subjected to quantum state tomography by placing a quater-wave(QWP) and a HWP in the path. The QWP and HWP are mounted in automatic rotation stages that controls the angle with high precision. After the waveplates the single-photons in path 1' and 4' are coupled into single-mode polarizing fiber beamsplitters.

Fiber coupled APDs are used for detection, where the polarization discrimination is achieved using

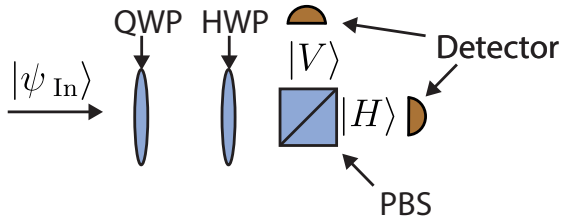

Figure 7.5: Quantum state tomography of polarization encoded single-photons. The QWP and HWP enable rotations between the three polarization bases and the PBS projects the single-photon onto the basis of choice. Single-photon detectors record the distribution of the photon polarization.

the PBSs, both free-space and fiber PBS. The correlation of detected photon events is registered using FPGA, which also controls the angle of the wave plates.

State verification

Prior to utilizing an entangled state for computation, the degree entanglement of the state must be verified. State verification of an entangled state is achievable in various ways, e.g. correlations that violate Bell's inequality indicates that the state is an entangled state. But the absence of observance of Bell's inequality violation does not imply absence of entanglement and another measure of entanglement is required.

The density matrix, reconstructed through a full quantum state tomography, reveals the degree of entanglement of a particular state. The measure of entanglement of a bipartite system is quantified by the tangle τ_{AB} [162]:

$$\tau_{\mathrm{AB}} = [\max\{0, \lambda_1 - \lambda_2 - \lambda_3 - \lambda_4\}]^2. \tag{7.12}$$

Here λ_i are the eigenvalues of the density matrix ρ_{AB} for the bipartite system consisting of qubits A and B. The eigenvalues are sorted in decreasing order $\lambda_1..\lambda_4$. A tangle of $\tau_{\mathrm{AB}} = 1$ signifies a maximal entangled state and a state with tangle $\tau_{\mathrm{AB}} = 0$ is completely disentangled. To measure a violation of Bell's inequality the tangle $\tau > 0.5$[163]. The concurrence of the state is related to the tangle through $C = \sqrt{\tau_{\mathrm{AB}}}$.

State tomography

The full density matrix of the quantum state is reconstructed through a quantum state tomography, which reveals both the occupation amplitudes and phases of the state [164].

If the qubits are photons and encoded in the polarization, the photon state is described as a point on the Poincaré sphere and characterized in either the linear basis $\{|V\rangle, |H\rangle\}$, the diagonal basis $\{|D\rangle, |A\rangle\}$ or the circular basis $\{|R\rangle, |L\rangle\}$. Under these circumstances the single-photon tomography is performed using wave plates, a PBS and single-photon detectors [165].

Fig. 7.5 shows a single-photon tomography setup, which consists of a QWP and a HWP placed in front of a PBS. The two wave plates enable rotations of the single-photon polarization between the different polarization bases. The polarization of the photon is then projected onto the $\{|V\rangle, |H\rangle\}$ basis by the PBS and detected by either detector.

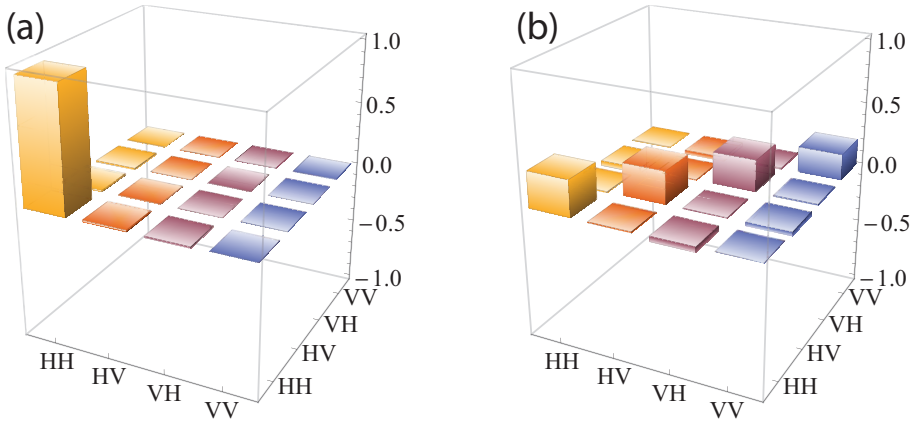

Figure 7.6: Two qubit tomography of the state **a)** $|HH\rangle$. The tomography shows the density matrix is dominated by the $|HH\rangle\langle HH|$. **b)** $|DD\rangle$. The density matrix demonstrates that there is an equal probability of measuring either $|HH\rangle$, $|HV\rangle$, $|VH\rangle$ or $|VV\rangle$.

The tomography of the single-photons is constructed by the projection onto the three basis. If two detectors are utilized there are three measurement settings needed to obtain a full description. Assuming the input state is a superposition of the two linear polarizations states $|\psi\rangle = \frac{1}{\sqrt{2}}(|H\rangle + |V\rangle)$, the detected count rates of the two detectors are expected to be equal and half of the total count rate when measuring in the linear polarization basis. But as a eigenstate of the other basis generates the same detection pattern, the chosen measurement setting is not sufficient to faithfully reconstruct the input state. By measuring projection onto the six basis states a detection pattern emerges that is reconciled uniquely by the input state.

If the state of interest is a two qubit state, e.g. a Bell state, the tomography is performed by analyzing each qubit using a setup as seen in Fig. 7.5. To obtain a full description of the two qubit state, the possible settings are permuted between the two setups to generate nine different measurement settings [165]. The detection events in the different basis are correlated between the two detection setups to achieve a description of the two qubit state.

The fidelity quantifies the overlap between the measured state ρ_1 and the expected state ρ_2, $F(\rho_1, \rho_2) = \mathrm{Tr}(\sqrt{\sqrt{\rho_1}\rho_2\sqrt{\rho_1}})$. The fidelity is dependent on the choice of expected state.

To characterize the tomography setup, a single-photon pair is prepared in a polarization pure state, e.g. $|HH\rangle$, using a HWP. The density matrix of the single-photon pair is then reconstructed using the tomography setup.

Fig. 7.6 (a) shows the reconstructed density matrix of a $|HH\rangle$ input state, the density matrix is dominated by the $|HH\rangle\langle HH|$ term as expected. The density matrix shows non-zero values in components expected to be zero, these errors are likely induced by either the tomography wave plates or the state preparation. The fidelity of the reconstructed density matrix with the ideal density matrix is extracted to $F_{|\psi\rangle|HH\rangle} = 0.99 \pm 0.02$ Fig. 7.6 (b) shows the density matrix of the $|DD\rangle$ state, which shows there is an equal probability of measuring any combination of the basis states. It also shows that the outcome is uncorrelated and no entanglement is present, as expected. The extracted fidelity is $F_{|\psi\rangle|DD\rangle} = 0.98 \pm 0.02$.

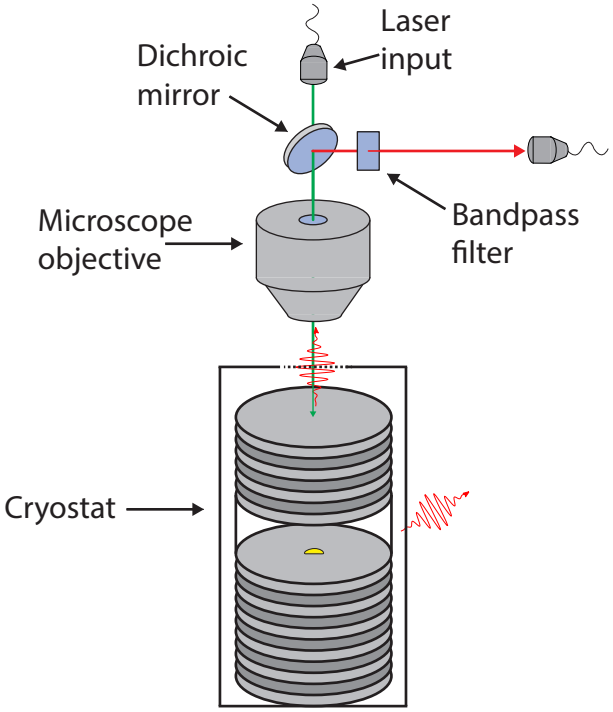

Figure 7.7: Experimental setup and sample. The sample is a micropillar cavity with a QD in the center, the cavity is comprised of Bragg reflectors, consisting of alternating layers of material, constituting highly reflective mirrors. The outcoupling mirror has fewer periods than the bottom reflector, which makes the outcoupling skewed towards the top.
The excitation laser, shown in green, is coupled out of a single-mode fiber and collimated by a lens. The laser is sent through a dichroic mirror and focused by the microscope objective onto the sample, which is mounted in a closed-cycle cryostat. The emission is collected by the objective and reflected off the dichroic mirror to filter the excitation laser. The reflected emission is sent through a narrow bandpass filter centered at the QD emission frequency. The filtered emission is coupled into a single-mode fiber for detection.

7.3 Source of single-photons

To generate a four-fold single-photon state at a sufficient rate, an efficient single-photon source is required. A QD embedded in a micropillar cavity constitutes an efficient single-photon source [36, 37]. A sketch of the micropillar structure is seen in Fig. 7.7, an optical cavity is formed by the high-index contrast between GaAs and air. To enhance the Q-factor of the cavity, distributed $\lambda/4$ Bragg gratings are formed above and below the cavity, which act as high reflectance mirrors at the resonance frequency. The Bragg mirrors are constructed by alternating GaAs and $Al_{0.9}Ga_{0.1}As$ layers, with a thickness fulfilling the Bragg condition. The reflection of the top and bottom mirror is made asymmetric, by having more alternating periods of the Bragg reflector below, to enhance the coupling in the upward direction in order to maximize the collected intensity. The QD is positioned in the antinode of the cavity.

The micropillar constitutes a circular stepindex waveguide, in the propagation direction of the collected emission, with $n_{\mathrm{GaAs}} = 3.5$ and $n_{\mathrm{Vacuum}} = 1$. The collected electric field is described by the

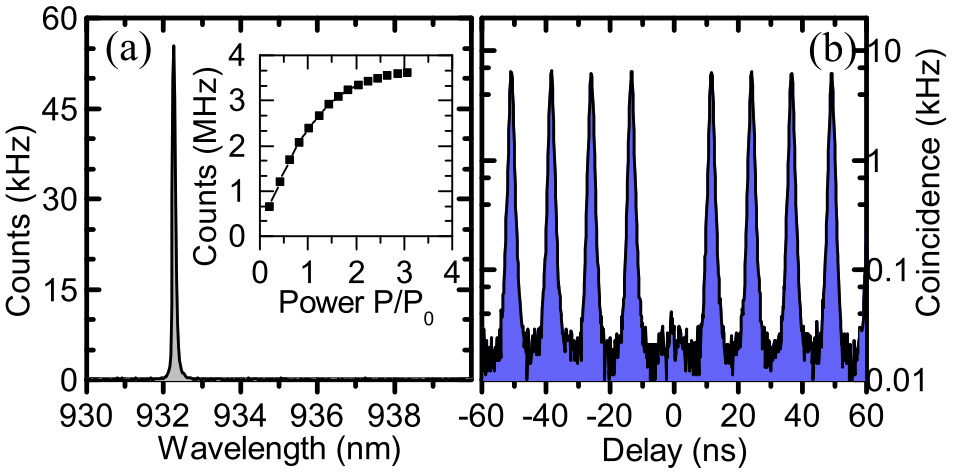

Figure 7.8: **a)** Emission spectrum from the sample with $\lambda_{\text{laser}} = 825\,\text{nm}$ and $T = 15\,\text{K}$. The spectrum is dominated by emission from a single QD coupled to the cavity. The inset shows the saturation curve of the QD measured on an APD. At saturation power the count rates are $\Gamma_{P_0} = 2.5\,\text{MHz}$ and the maximum count rates are $\Gamma_{3P_0} = 3.5\,\text{Mhz}$ **b)** A HBT measurement of the filtered emission. The extracted single-photon purity of the emission is $g^{(2)}(0) = 0.025 \pm 0.009$.

Helmholtz equation in spherical coordinates. The solutions are well-known and are Bessel functions. The fundamental Bessel function is a Gaussian mode, which enhances the overlap of the out-coupled mode with a single-mode fiber. The higher-order Bessel functions have intensity lopes along the radial distribution, causing a reduced overlap.

A confocal setup, shown in Fig. 7.7, is used to excite the QD and collect the emission. The excitation laser is coupled out of a single mode fiber and the polarization is projected onto a polarizer to ensure that the excitation polarization is constant. The excitation laser is transmitted through a dichroic mirror and focused through a microscope objective onto the sample. The emission from the sample is collected using the microscope objective and is reflected off the dichroic mirror. Residual scattered laser light and emission from unwanted states is suppressed using a narrow bandpass filter. The filtered emission is coupled into a single-mode fiber, which is coupled to either a spectrometer, single-photon detection setups or quantum photonic gates.

Fig. 7.8 (a) shows a spectrum of the QD on resonance with the cavity while the sample is excited above the bandgap. The detuning between emission line and cavity mode is controlled by the sample temperature. The emission energy of the QD is related to the temperature of the sample through the thermal expansion and contraction of the lattice. As the sample temperature is raised, the sample expands causing a redshift of the emission line, as the emission energy is inversely related to the size of the QD.

The QD is found to be on resonance with the cavity at $T = 15\,\text{K}$. By further red shifting, the QD the intensity is enhanced but the increased temperature causes an increased phonon sideband [101]. The increased phonon population causes a reduction in the measured indistinguishability and to enhance the indistinguishability of the emitted photons the temperature is kept at $T = 15\,\text{K}$.

In Fig. 7.8 (b) the second order correlation of a HBT measurement of the emission line is shown. The emission demonstrates a high single-photon purity with almost no correlation at $\tau = 0$. The

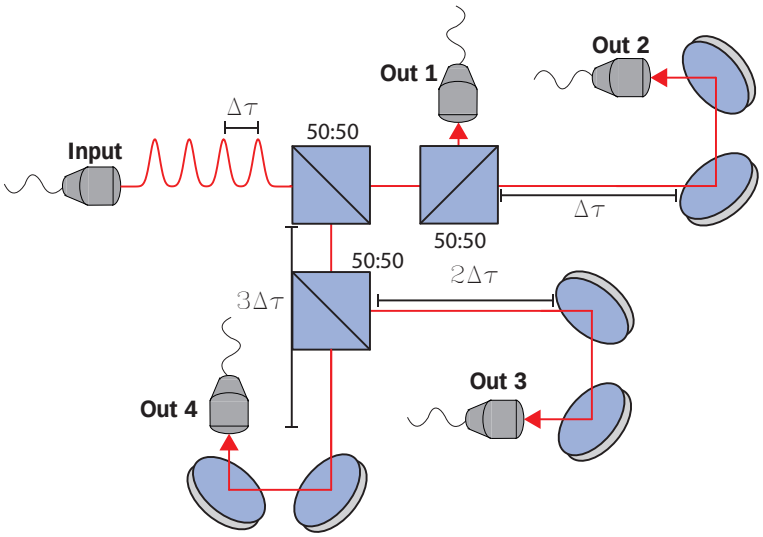

Figure 7.9: Setup for four-fold single-photon state generation. Single-photons are entering the probabilistic demultiplexing setup separated by the repetition time of the excitation laser $\Delta\tau = \frac{1}{\Gamma_{\text{Laser Rep}}}$. The single-photons are sent onto cascaded 50:50 beamsplitters that separate the single-photons in four paths. The path length difference is matched to a multiple of the repetition time and the single-photons are coupled into single-mode fibers.

extracted $g^{(2)}(0) = 0.025 \pm 0.009$ signifies an almost ideal single-photon source. The $g^{(2)}(0)$ extracted without background correcting.

To enhance the single-photon indistinguishability the QD is excited through a p-shell resonance at $\lambda_{\text{laser}} = 913.5\,\text{nm}$ for the following measurements.

Four-fold single-photon source

The entangling gate discussed requires a four-fold single-photon state as the initial state. To generate the four-fold single-photon state from a stream of single-photons, a probabilistic demultiplexing scheme is utilized. The setup is sketched in Fig. 7.9, a stream of single-photons, separated by the repetition time of the excitation laser $\Delta\tau = \frac{1}{\Gamma_{\text{Laser Rep}}}$ is coupled into the probabilistic demultiplexing setup. Cascaded 50:50 beamsplitters are used to separate the single-photons to individual beam paths and couple them to single-mode fibers. The path length difference of the four paths are roughly matched to the multiple of $\Delta\tau$ using single-mode fibers, while the temporal delay is fine-tuned using motorized translation stages in each arm.

The single-mode fibers are connected to respective inputs in the entangling gate. To offset any temporal mismatch induced by the entangling gate, the translation stages are used to synchronize the photons. As one of the outputs is temporally fixed, the other ports are matched to this port. A coarse temporal matching is achieved by a time of flight measurement with respect to a clock signal. The resolution of this method is limited by the bin size of the detection system, in this case $t_{\text{bin}} = 81\,\text{ps}$ of the time-tagging device.

To obtain a greater temporal resolution the observation of two-photon interference is utilized, which is a method commonly used in SPDC experiments [160]. As the paths are mode-matched Hong-Ou-Mandel bunching of the single-photons is observed when the temporal offset between the

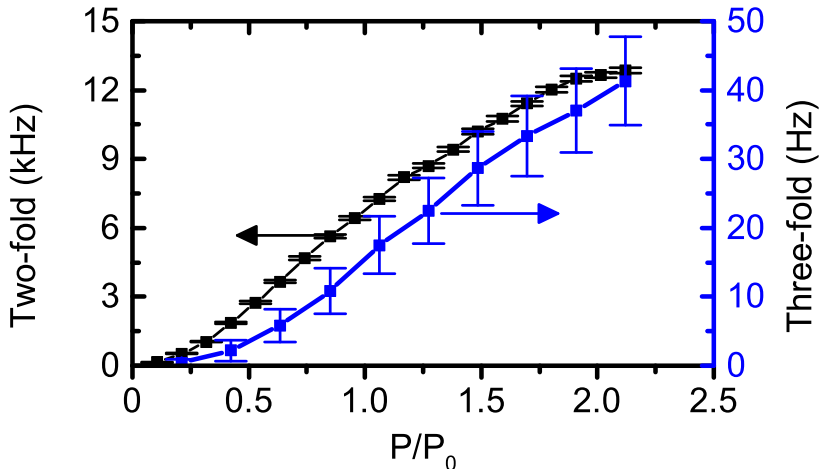

Figure 7.10: Measured two (three)-fold rate after the probabilistic demultiplexing setup as a function of pump power. For the two(three)- fold measurement, the loss induced by the demultiplexing setup is $\frac{1}{2^2}$ ($\frac{1}{3^3}$). The exponential scaling of the photon losses, in both extraction and demultiplexing, reduces the likelihood of observing multiple fold photon events.

two photons is less than the coherence time. By adjusting the temporal offset the measured correlation is minimized. The resolution is thereby not limited by the detection equipment, but instead limited by the stepping resolution of the translation stages. To achieve a reduction in correlation events, the single-photons must exhibit some degree of indistinguishability.

With the temporal delays fixed, the higher-fold count rates are tested. By rotating the HWP in front of the PBS, the splitting ratio of the resulting beamsplitter is reconfigurable. The source is therefore readily modified to any lower photon number. In Fig. 7.10 the saturation curve for the two-fold and three-fold source is shown. The coincidence window is set to 3 ns. At saturation a 2-fold (3-fold) rate of $\Gamma_{2-\text{fold}} = 12.9 \pm 0.1\,\text{kHz}$ ($\Gamma_{3-\text{fold}} = 41.3 \pm 6.4\,\text{Hz}$ is extracted. As the loss scales exponentially for the preparation of the multiple fold single-photon state, the rate of detected events is quickly diminishing. The probabilistic nature of the demultiplexing setup also induces an exponential scaling loss of $\frac{1}{N^N}$, where N is the desired number of single-photons in the N-fold single-photon state.

The ratio between the 3-fold rate and the 2-fold rate is not solely given by the ratio of their respective propabillistic scalings. The two rates also scales differently with the single-photon extraction rate:

$$\frac{\Gamma_{3-\text{fold}}}{\Gamma_{2-\text{fold}}} = \frac{4}{27}\eta_{\text{SP}} \tag{7.13}$$

Here η_{SP} is the single-photon efficiency, which quantifies the probabillity of a single-photon reaching the propabillistic demultiplexing setup. At saturation $\eta_{\text{SP}} = 0.022 \pm 0.003$ is extracted.

For the four-fold single-photon state a detail study of the count rates as a function of power is hindered by the low rate of coincidence counts, instead the 4-fold single-photon rate at saturation is measured to $\Gamma_{4-\text{fold}} = 0.074 \pm 0.013\,\text{Hz}$. By using the single-photon efficiency, the expected 4-fold rate is

$$\Gamma_{4-\text{fold}}^{\text{expected}} = \frac{1}{4^4}\eta_{\text{SP}}^4\Gamma_{\text{laser}} = 0.066 \pm 0.010\,\text{Hz}. \tag{7.14}$$

The expected rate extracted using η_{SP} aligns well with the measured $\Gamma_{4-\text{fold}}$ rate.

The four-fold single-photon rate combined with the success probability of the gate means the integration time required to generate sufficient statistics at present is unfeasible. Due to the polarization projection of the heralding photons only one polarization combination is probed, e.g. $|HH\rangle$. This projection reduces the available heralding states to half of a single Bell state of Eq. (7.10), which reduces the heralding success probability to $P_{\text{Succes}} = \frac{1}{32}$. As four detectors are used for the two qubit tomography, the required measurement settings to obtain a full tomography is N_{MeasSet}. To reduce the coefficient of variation to 10%, the number of recorded events must be N_{Cnt} and the total integration time at the current $\Gamma_{4-\text{fold}}$ is therefore:

$$T_{\text{Int}} = \frac{1}{\Gamma_{4-\text{fold}} P_{\text{Succes}}} N_{\text{MeasSet}} N_{\text{Cnt}} \approx 114.2\,\text{Hr}. \tag{7.15}$$

Instead methods to improve the four-fold detection rate is investigated. Improving the efficiency of the demultiplexing setup, using active switching could increase the rate significantly. Also improving the detector efficiency using superconducting single-photon detectors would yield a similar benefit [166].

Two-photon interference in the gate

To verify the temporal and spatial overlap of the single-photons in the gate, the two-photon interference between the various inputs is measured. The HOM measurements are all performed in the diagonal basis

The measured HOM interferences through the gate are shown in Fig. 7.11. The red curve in Fig. 7.11 (a) shows the interference between port 1 and 3 on the RPBS, while the blue plot shows the interference between port 1 and 4 on the RPBS. Fig. 7.11 (b) shows the interference of port 1 and 2 on the first PBS.

The extracted indistinguishability is $V_{12.5\,\text{ns}} = 0.42 \pm 0.02$, $V_{25\,\text{ns}} = 0.51 \pm 0.02$ and $V_{37.5\,\text{ns}} = 0.27 \pm 0.03$, which is considerably lower than previous measurements on the same device [101]. After these measurements were performed, it was realized that both dipoles of the QD was contributing to the collected signal and the fine-structure splitting was reducing the measured indistinguishability. By introducing a linear polarizer in the collection setup a single dipole is collected and the results of Ref. [101] is reproduced.

The three HOM measurements are used to quantify, if an entangled state is expected to be generated in the gate. As discussed the observed entanglement is dependent on the visibility of the single-photons interfered. The observed indistinguishability is constant between the various inputs due to the difference in temporal separation. It is expected that the smallest indistinguishability dominates the extracted concurrence. From the extracted indistinguishability it is not expected to generate an entangled state, but improvements in the indistinguishability should lead to an entangled state being generated.

As the three HOM measurements shows indistinguishability between port 1 and the remaining ports, it is inferred that the remaining ports are also matched.

Tthe HOM interference is expected to diminish as the separation in emission time between the single-photons is increased, which has been confirmed for this source [101], but in Fig. 7.11 (a) the correlated peak is suppressed stronger when the separation is $\Delta\tau = 25\,\text{ns}$ versus $\Delta\tau = 12.5\,\text{ns}$. This unexpected behavior indicates that either the mode or the temporal overlap is suboptimal.

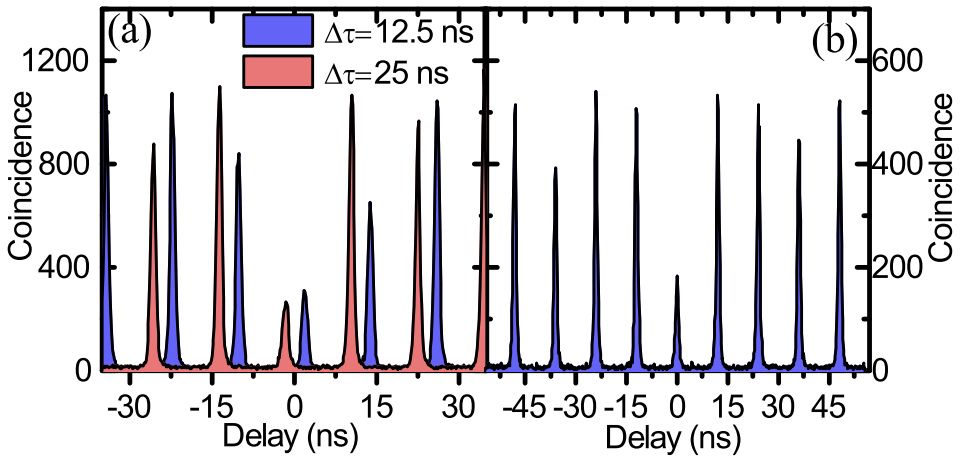

Figure 7.11: **a)** HOM measurement of the single-photon source through the entangling gate between port 1 and 3 with temporal separation of $\Delta\tau = 12.5\,\text{ns}$ for the blue curve. For the red curve the interference is between port 1 and 4 with a temporal separation of $\Delta\tau = 25\,\text{ns}$. The two curves are displaced for clarity. **b)** HOM measurement of the single-photon source through the entangling gate between port 1 and 2 with a temporal separation of $\Delta\tau = 37.5\,\text{ns}$.

The separation in emission time $\Delta\tau$ is readily deduced from the HOM measurements by observing the reduced peak at $\Delta\tau$, as it is reduced to 0.75 of the remaining uncorrelated peaks.

At the current measured indistinguishability it should be possible to measure the quantum discord [155]. The quantum discord are correlations between two particles that exhibits some degree of quantumness, but without being entangled [167]. The quantum discord should be measurable at $V = 0.07$ [155].

To generate an entangled state that can violate Bell's inequality a single-photon $V = 0.88$ is required. To obtain such a single-photon indistinguishability quasi-resonant excitation might be insufficient. But single-photon indistinguishability demonstrated using the source should be sufficient to measure a non-zero concurrence [101].

7.4 Conclusion

In this chapter a scheme for generating entangled single-photon pairs from a QD post-emission was presented. Different methods to generate entanglement between single-photons was discussed. Methods to verify an entangled photon pair was also presented and discussed.

A probabilistic demultiplexing setup for up to a 4-fold single-photon state was discussed and characterized. At saturation a 2-fold (3-fold) rate of $\Gamma_{2-\text{fold}} = 12.9 \pm 0.1\,\text{kHz}$ ($\Gamma_{3-\text{fold}} = 41.3 \pm 6.4\,\text{Hz}$) was found. The extracted 4-fold rate was $\Gamma_{4-\text{fold}} = 0.074 \pm 0.013\,\text{Hz}$. From these rates a single-photon efficiency of $\eta_{\text{SP}} = 0.022 \pm 0.003$ was extracted.

The theory behind the scheme was discussed and it was seen that the expected entanglement is strongly depended on the indistinguishability of the emitted single-photons. At the lowest extracted visibility of $V_{37.5\,\text{ns}} = 0.27 \pm 0.03$, entangled pairs was not expected to be generated.

Future work is proposed to focus on improving the efficiency of the demultiplexing setup by utilizing

deterministic demultiplexing, as the losses induced by the four-fold single-photon source is currently limiting the rate of generated entangled states.

Efforts to improve the indistinguishability of the emitted single-photons are also considered to improve the entanglement of the generated photon pair. Resonance florescence from the ground state exciton could potentially improve the indistinguishability on the various timescales. These efforts could potentially pave the way for Bell state test using post-emission generated entangled pairs with single-photons emitted from QDs.

Chapter 8

Conclusion

Quantum computation and simulation may be the resources of the next information revolution. Simulating increasingly more complex materials for catalysis or room-temperature superconducting transport of energy requires stable and scalable quantum computation.

In this thesis single-photons were discussed as a platform for scalable quantum computing.

Currently, the main challenge for quantum computing using single-photons is the efficient production of indistinguishable single-photons to ensure the scalability of the computation.

A theoretical study of a quantum dot in a photonic crystal cavity demonstrated, how the multi-level nature of the quantum dot combined with the complex local polarization of a photonic crystal causes deviation from the predictions of the Jaynes-Cummings model. It was shown that a slowly-decaying state is formed as a consequence of the destructive interference between the bright states of the QD. The formation of a slowly-decaying state has profound consequences for the indistinguishability of the emitted photons and it was demonstrated that even though the long-lived state is robust against dephasing, the inhibited decay causes the emitted photons to be distinguishable.

Two platforms for single-photon sources based on QD in photonic crystals were proposed. The photonic crystal cavity source was investigated theoretically. Theoretical simulations suggested the M3 mode of the cavity should be a suitable platform for a single-photon source. QDs in photonic crystal cavities were probed and a bright QD was examined. The source demonstrated a significant single-photon purity of $g^{(2)}(0) = 0.06 \pm 0.026$, but single-photon indistinguishability was not demonstrated with an extracted visibility of $V = 0.03 \pm 0.003$. The reduced indistinguishability is likely due to the quasi-resonant excitation method. A source based on QDs embedded in photonic crystal waveguide was also discussed. This source demonstrated a strong single-photon purity of $g^{(2)} = 0.014 \pm 0.004$ and indistinguishable photons under quasi-resonant excitation with an extracted visibility of $V = 0.032 \pm 0.02$. The indistinguishability of the single-photons was preserved over timescales up to 13 ns with an extracted visibility of $V = 0.24 \pm 0.06$.

It was discussed how the implementation of an efficient source of indistinguishable single-photons in quantum computing would require efficient demultiplexing of consecutive single-photons. A scheme for active demultiplexing of single-photons using electro-optical modulation on the timescale of a few ns was proposed and implemented. Using the single-photon demultiplexing setup a three-fold single-photon state was generated and demonstrated with a measured rate of $\Gamma_{3-\text{fold}} = 0.45 \pm 0.027\,\text{Hz}$. By correcting for device induced data loss, a post-selected 3-fold single-photon rate of $\Gamma_{3-\text{fold}}^{\text{Post-Selc}} =$

2.03 ± 0.49 Hz was extracted. The post-selected 3-fold single-photon rate exceeded the rate expected for an ideal passive demultiplexing source. This demonstrated how active demultiplexing is required for the successful implementation of quantum computation using single-photons produced by a single efficient source.

To build stable and efficient quantum computers based on single-photons emitted from quantum dots on-chip integration of source, photonic components and detectors are required. The integration of an on-chip power divider with a QD emitting single-photons was demonstrated. Through correlation measurements a single-photon purity of $g^{(2)}_{\text{auto}}(0) = 0.40 \pm 0.06$ was extracted. The power divider was confirmed to be separating the emitted single-photons into two ports by measuring a crosscorrelation between the two outputs. From the crossocorrelation a single-photon purity of $g^{(2)}_{\text{cross}}(0) = 0.25 \pm 0.04$ was extracted.

A scheme for generating entangled photon pairs post-emission was presented. In this context, the variety in application of entangled photon pairs was discussed. The methods of verifying an entangled state was discussed. An experimental demonstration of the scheme was build. A source of partially indistinguishable single-photons was used to characterize the expected performance of the gate. From the lowest extracted visibility of $V = 0.27 \pm 0.03$, no entanglement generation was expected.

The efficient single-photon source was utilized to prepare a four-fold single-photon state using a probabilistic demultiplexing. Due to the inefficiency of the probabilistic demultiplexing the generated four-fold rate was $\Gamma_{4-\text{fold}} = 0.074 \pm 0.013$ Hz. An enhancement of the four-fold rate was concluded to be required, in order to generate entangled pairs at a practical applicable rate.

Outlook

Employing resonant excitation of the ground state exciton should improve the indistinguishability of the emitted single-photons and making it a source of photonic qubits for quantum computing.

Utilizing the active demultiplexing setup for quantum computing would require an enhancement of the three-fold single-photon efficiency. Exploring the possibility of expanding the setup to demultiplexing higher fold single-photon states would mean new and more advanced protocols are realizable.

The combination of an efficient source of indistinguishable single-photons and an efficient generation of a four-fold single-photon state, would make the event-ready generation of Bell pairs possible at enhanced rates. Frequent generation of Bell pairs could be used for high count rate test of Bell's inequalities.

The technologies developed and discussed here, might in combination form the basis for efficient quantum computing using single-photons.

Bibliography

[1] Forest, J.J. & Sousa, M.V. *Oil and terrorism in the New Gulf: framing US energy and security policies for the Gulf of Guinea* (Lexington Books, 2006).

[2] Feynman, R.P. *Simulating physics with computers. Int. J. Theor. Phys* **21** 467–488 (1982).

[3] DiVincenzo, D. & Loss, D. *Quantum information is physical. Superlattices. Microstruct.* **23** 419 – 432 (1998).

[4] Stuhler, J. *Quantum optics route to market. Nat. Phys.* **11** 293–295 (2015).

[5] Ladd, T.D. et al. *Quantum computers. Nature* **464** 45–53 (2010).

[6] Lucero, E. et al. *Computing prime factors with a Josephson phase qubit quantum processor. Nat. Phys.* **8** 719–723 (2012).

[7] Nigg, D. et al. *Quantum computations on a topologically encoded qubit. Science* **345** 302–305 (2014).

[8] Barends, R. et al. *Superconducting quantum circuits at the surface code threshold for fault tolerance. Nature* **508** 500–503 (2014).

[9] Cirac, J.I. & Zoller, P. *Quantum computations with cold trapped ions. Phys. Rev. Lett.* **74** 4091 (1995).

[10] Harty, T.P. et al. *High-Fidelity Preparation, Gates, Memory, and Readout of a Trapped-Ion Quantum Bit. Phys. Rev. Lett.* **113** 220501 (2014).

[11] Kim, J. *Viewpoint: Trapped Ions Make Impeccable Qubits. Physics* **7** 119 (2014).

[12] Stick, D. et al. *Ion trap in a semiconductor chip. Nat. Phys.* **2** 36–39 (2006).

[13] Brown, R.H. & Twiss, R.Q. *Correlation between photons in two coherent beams of light. Nature* **177** 27–29 (1956).

[14] Hong, C.K., Ou, Z.Y. & Mandel, L. *Measurement of subpicosecond time intervals between two photons by interference. Phys. Rev. Lett.* **59** 2044–2046 (1987).

[15] U'Ren, A.B., Silberhorn, C., Banaszek, K. & Walmsley, I.A. *Efficient conditional preparation of high-fidelity single photon states for fiber-optic quantum networks. Phys. Rev. Lett.* **93** 093601 (2004).

[16] Ballentine, L.E. *Quantum Mechanics* (World Scientific, Singapore, 2003).

[17] Carmichael, H. & Walls, D. *A quantum-mechanical master equation treatment of the dynamical Stark effect. J. Phys. B* **9** 1199 (1976).

[18] Kimble, H., Dagenais, M. & Mandel, L. *Photon antibunching in resonance fluorescence. Phys. Rev. Lett.* **39** 691 (1977).

[19] Kuhn, A., Hennrich, M. & Rempe, G. *Deterministic single-photon source for distributed quantum networking. Phys. Rev. Lett.* **89** 067901 (2002).

[20] Kurtsiefer, C., Mayer, S., Zarda, P. & Weinfurter, H. *Stable Solid-State Source of Single Photons. Phys. Rev. Lett.* **85** 290–293 (2000).

[21] Brouri, R., Beveratos, A., Poizat, J.P. & Grangier, P. *Photon antibunching in the fluorescence of individual color centers in diamond. Opt. Lett.* **25** 1294 (2000).

[22] Michler, P. et al. *A quantum dot single-photon turnstile device. Science* **290** 2282–5 (2000).

[23] Santori, C., Pelton, M., Solomon, G., Dale, Y. & Yamamoto, Y. *Triggered single photons from a quantum dot. Phys. Rev. Lett.* **86** 1502 (2001).

[24] Leonard, D., Krishnamurthy, M., Reaves, C., Denbaars, S.P. & Petroff, P. *Direct formation of quantum-sized dots from uniform coherent islands of InGaAs on GaAs surfaces. Appl. Phys. Lett.* **63** 3203–3205 (1993).

[25] Má rquez, J., Geelhaar, L. & Jacobi, K. *Atomically resolved structure of InAs quantum dots. Appl. Phys. Lett.* **78** 2309–2311 (2001).

[26] Adler, F. et al. *Optical transitions and carrier relaxation in self assembled InAs/GaAs quantum dots* **80** 4019–4026 (1996).

[27] Kiraz, A., Atatüre, M. & Imamoğlu, A. *Quantum-dot single-photon sources: Prospects for applications in linear optics quantum-information processing. Phys. Rev. A* **69** 032305 (2004).

[28] Kuhlmann, A.V. et al. *Charge noise and spin noise in a semiconductor quantum device. Nat. Phys.* **9** 570–575 (2013).

[29] Madsen, K.H. et al. *Measuring the effective phonon density of states of a quantum dot in cavity quantum electrodynamics. Phys. Rev. B* **88** 045316 (2013).

[30] McKeever, J. et al. *Deterministic Generation of Single Photons from One Atom Trapped in a Cavity. Science* **303** 1992–1994 (2004).

[31] Darquié, B. et al. *Controlled Single-Photon Emission from a Single Trapped Two-Level Atom. Science* **309** 454–456 (2005).

[32] Trupke, M. et al. *Atom detection and photon production in a scalable, open, optical microcavity. Phys. Rev. Lett.* **99** 063601 (2007).

[33] Purcell, E.M. *Spontaneous emission probabilities at radio frequencies. Phys. Rev.* **69** (1946).

[34] Goban, A. et al. *Atom–light interactions in photonic crystals. Nat. Comm.* **5** (2014).

[35] Tiecke, T. et al. *Nanophotonic quantum phase switch with a single atom. Nature* **508** 241–244 (2014).

[36] Claudon, J. et al. *A highly efficient single-photon source based on a quantum dot in a photonic nanowire. Nat Photon* **4** 174–177 (2010).

[37] Gazzano, O. et al. *Bright solid-state sources of indistinguishable single photons. Nat Commun* **4** 1425 (2013).

[38] Ding, X. et al. *On-Demand Single Photons with High Extraction Efficiency and Near-Unity Indistinguishability from a Resonantly Driven Quantum Dot in a Micropillar. Phys. Rev. Lett.* **116** 020401 (2016).

[39] Yablonovitch, E. *Inhibited Spontaneous Emission in Solid-State Physics and Electronics. Phys. Rev. Lett.* **58** 2059–2062 (1987).

[40] Lodahl, P. et al. *Controlling the dynamics of spontaneous emission from quantum dots by photonic crystals. Nature* **430** 654–657 (2004).

[41] Madsen, K.H. et al. *Efficient out-coupling of high-purity single photons from a coherent quantum dot in a photonic-crystal cavity. Phys. Rev. B* **90** 155303 (2014).

[42] Arcari, M. et al. *Near-unity coupling efficiency of a quantum emitter to a photonic crystal waveguide. Phys. Rev. Lett.* **113** 093603 (2014).

[43] Lodahl, P., Mahmoodian, S. & Stobbe, S. *Interfacing single photons and single quantum dots with photonic nanostructures. Rev. Mod. Phys.* **87** 347 (2015).

[44] Reithmaier, G. et al. *On-chip generation, routing, and detection of resonance fluorescence* **15** 5208–5213 (2015).

[45] Prtljaga, N. et al. *Monolithic integration of a quantum emitter with a compact on-chip beam-splitter. Appl. Phys. Lett.* **104** 231107 (2014).

[46] Han, S., Seok, T.J., Quack, N., Yoo, B.w. & Wu, M.C. *Monolithic 50x50 mems silicon photonic switches with microsecond response time.* In *Optical Fiber Communication Conference* (Optical Society of America, 2014), M2K.

[47] Einstein, A., Podolsky, B. & Rosen, N. *Can Quantum-Mechanical Description of Physical Reality Be Considered Complete? Phys. Rev.* **47** 777–780 (1935).

[48] Bell, J. *On the Problem of Hidden Variables in Quantum Mechanics. Rev. Mod. Phys.* **38** 447–452 (1966).

[49] Aspect, A., Grangier, P. & Roger, G. *Experimental Tests of Realistic Local Theories via Bell's Theorem. Phys. Rev. Lett.* **47** 460–463 (1981).

[50] O'Brien, J.L., Pryde, G.J., White, A.G., Ralph, T.C. & Branning, D. *Demonstration of an all-optical quantum controlled-NOT gate. Nature* **426** 264–267 (2003).

[51] Knill, E., Laflamme, R. & Milburn, G.J. *A scheme for efficient quantum computation with linear optics. Nature* **409** 46–52 (2001).

[52] Gazzano, O. et al. *Entangling quantum-logic gate operated with an ultrabright semiconductor single-photon source. Phys. Rev. Lett.* **110** 250501 (2013).

[53] Politi, A., Matthews, J.C. & O'brien, J.L. *Shor's quantum factoring algorithm on a photonic chip. Science* **325** 1221–1221 (2009).

[54] Shor, P.W. *Algorithms for quantum computation: Discrete logarithms and factoring.* In *Foundations of Computer Science, 1994 Proceedings., 35th Annual Symposium on* (IEEE, 1994), 124–134.

[55] O'Brien, J.L. *Optical quantum computing. Science* **318** 1567–1570 (2007).

[56] Volz, J., Scheucher, M., Junge, C. & Rauschenbeutel, A. *Nonlinear [pi] phase shift for single fibre-guided photons interacting with a single resonator-enhanced atom. Nat. Phot.* **8** 965–970 (2014).

[57] Javadi, A. et al. *Single-photon non-linear optics with a quantum dot in a waveguide. Nat. Comm.* **6** (2015).

[58] Ralph, T., Söllner, I., Mahmoodian, S., White, A. & Lodahl, P. *Photon sorting, efficient Bell measurements, and a deterministic controlled-Z gate using a passive two-level nonlinearity. Phys. Rev. Lett.* **114** 173603 (2015).

[59] Raussendorf, R. & Briegel, H.J. *A one-way quantum computer. Phys. Rev. Lett.* **86** 5188 (2001).

[60] Akopian, N. et al. *Entangled photon pairs from semiconductor quantum dots. Phys. Rev. Lett.* **96** 130501 (2006).

[61] Stevenson, R.M. et al. *A semiconductor source of triggered entangled photon pairs. Nature* **439** 179–182 (2006).

[62] Lindner, N.H. & Rudolph, T. *Proposal for pulsed on-demand sources of photonic cluster state strings. Phys. Rev. Lett.* **103** 113602 (2009).

[63] Browne, D.E. & Rudolph, T. *Resource-efficient linear optical quantum computation. Phys. Rev. Lett.* **95** 010501 (2005).

[64] Lanyon, B.P. et al. *Towards quantum chemistry on a quantum computer. Nat. Chem.* **2** 106–111 (2010).

[65] Aspuru-Guzik, A., Dutoi, A.D., Love, P.J. & Head-Gordon, M. *Simulated quantum computation of molecular energies. Science* **309** 1704–1707 (2005).

[66] Broome, M.A. et al. *Photonic boson sampling in a tunable circuit. Science* **339** 794–798 (2013).

[67] Spring, J.B. et al. *Boson sampling on a photonic chip. Science* **339** 798–801 (2013).

[68] Huh, J., Guerreschi, G.G., Peropadre, B., McClean, J.R. & Aspuru-Guzik, A. *Boson sampling for molecular vibronic spectra. Nature Photon.* (2015).

[69] Yoshie, T. et al. *Vacuum Rabi splitting with a single quantum dot in a photonic crystal nanocavity. Nature* **432** 200–3 (2004).

[70] Hennessy, K. et al. *Quantum nature of a strongly coupled single quantum dot-cavity system. Nature* **445** 896–9 (2007).

[71] Andersen, M.L., Stobbe, S., Sørensen, A.S. & Lodahl, P. *Strongly modified plasmon–matter interaction with mesoscopic quantum emitters. Nat. Phys.* **7** 215–218 (2010).

[72] Tighineanu, P., Sørensen, A.S., Stobbe, S. & Lodahl, P. *Unraveling the mesoscopic character of quantum dots in nanophotonics. Phys. Rev. Lett.* **114** 247401 (2015).

[73] Faraon, A. et al. *Coherent generation of non-classical light on a chip via photon-induced tunnelling and blockade. Nat. Phys.* **4** 859–863 (2008).

[74] Laucht, A. et al. *Dephasing of Exciton Polaritons in Photoexcited InGaAs Quantum Dots in GaAs Nanocavities. Phys. Rev. Lett.* **103** 087405 (2009).

[75] Englund, D. et al. *Resonant Excitation of a Quantum Dot Strongly Coupled to a Photonic Crystal Nanocavity. Phys. Rev. Lett.* **104** 073904 (2010).

[76] Reinhard, A. et al. *Strongly correlated photons on a chip. Nat. Phot.* **6** 93–96 (2012).

[77] Madsen, K.H., Lehmann, T.B. & Lodahl, P. *Role of multi-level states on quantum-dot emission in photonic-crystal cavities* (2016).

[78] Jaynes, E. & Cummings, F. *Comparison of quantum and semiclassical radiation theories with application to the beam maser. Proc. IEEE* **51** 89–109 (1963).

[79] Rabi, I.I. *Space quantization in a gyrating magnetic field. Phys. Rev.* **51** 652–4 (1937).

[80] Lindblad, G. *On the generators of quantum dynamical semigroups. Commun. Math. Phys.* **48** 119–130 (1976).

[81] Carmichael, H., Brecha, R., Raizen, M., Kimble, H. & Rice, P. *Subnatural linewidth averaging for coupled atomic and cavity-mode oscillators. Phys. Rev. A* **40** 5516–5519 (1989).

[82] Madsen, K.H. & Lodahl, P. *Quantitative analysis of quantum dot dynamics and emission spectra in cavity quantum electrodynamics. New J. Phys.* **15** (2013).

[83] Bayer, M. et al. *Fine structure of neutral and charged excitons in self-assembled In(Ga)As/(Al)GaAs quantum dots. Phys. Rev. B* **65** 195315 (2002).

[84] Johansen, J., Julsgaard, B., Stobbe, S., Hvam, J.M. & Lodahl, P. *Probing long-lived dark excitons in self-assembled quantum dots. Phys. Rev. B* **81** 081304 (2010).

[85] Hudson, A.J. et al. *Coherence of an Entangled Exciton-Photon State. Phys. Rev. Lett.* **99** 266802 (2007).

[86] Dicke, R.H. *Coherence in Spontaneous Radiation Processes. Phys. Rev.* **93** 99–110 (1954).

[87] De Greve, K. et al. *Ultrafast coherent control and suppressed nuclear feedback of a single quantum dot hole qubit. Nat. Phys.* **7** 872–878 (2011).

[88] Bylander, J., Robert-Philip, I. & Abram, I. *Interference and correlation of two independent photons. EUR. PHYS. J. D* **22** 295–301 (2003).

[89] Santori, C., Fattal, D., Vučković, J., Solomon, G.S. & Yamamoto, Y. *Indistinguishable photons from a single-photon device. Nature* **419** 594–597 (2002).

[90] Loudon, R. *The Quantum Theory of Light* (Oxford Science Publications, Oxford, 2000), third edition.

[91] Wang, H. et al. *Near Transform-Limited Single Photons from an Efficient Solid-State Quantum Emitter* (2016).

[92] Somaschi, N. et al. *Near-optimal single-photon sources in the solid state. Nature Photon.* (2016).

[93] Akahane, Y., Asano, T., Song, B.S. & Noda, S. *High-Q photonic nanocavity in a two-dimensional photonic crystal. Nature* **425** 944–7 (2003).

[94] Stobbe, S., Johansen, J., Kristensen, P., Hvam, J. & Lodahl, P. *Frequency dependence of the radiative decay rate of excitons in self-assembled quantum dots: Experiment and theory. Phys. Rev. B* **80** 155307 (2009).

[95] Johansen, J. et al. *Size dependence of the wavefunction of self-assembled InAs quantum dots from time-resolved optical measurements. Phys. Rev. B* **77** 073303 (2008).

[96] Madsen, K.H. *Coherent Dynamics of Quantum Dots in Photonic-Crystal Cavities.* Ph. d. thesis, Technical University of Denmark (2013).

[97] Schmid, B., Petrov, A. & Eich, M. *Optimized grating coupler with fully etched slots. Opt. Express* **17** 11066–11076 (2009).

[98] Kiršanské, G. *Electrical control of excitons in semiconductor nanostructures.* Ph. D. thesis, Niels Bohr Institute (2016).

[99] Albrecht, S. *Highly Efficienct Extraction of Single Photons from a Quantum Dot in a Photonic Crystal Nanocavity.* Ph.D. thesis, Niels Bohr Institute (2013).

[100] Ates, S. et al. *Post-Selected Indistinguishable Photons from the Resonance Fluorescence of a Single Quantum Dot in a Microcavity. Phys. Rev. Lett.* **103** 167402 (2009).

[101] Loredo, J.C. et al. *Scalable performance in solid-state single-photon sources. Optica* **3** 433–440 (2016).

[102] Khaetskii, A.V., Loss, D. & Glazman, L. *Electron spin decoherence in quantum dots due to interaction with nuclei. Phys. Rev. Lett.* **88** 186802 (2002).

[103] Merkulov, I., Efros, A.L. & Rosen, M. *Electron spin relaxation by nuclei in semiconductor quantum dots. Phys. Rev. B* **65** 205309 (2002).

[104] Atatüre, M. et al. *Quantum-dot spin-state preparation with near-unity fidelity. Science* **312** 551–553 (2006).

[105] Houel, J. et al. *Probing single-charge fluctuations at a GaAs/AlAs interface using laser spectroscopy on a nearby InGaAs quantum dot. Phys. Rev. Lett.* **108** 107401 (2012).

[106] Gazzano, O. et al. *Entangling Quantum-Logic Gate Operated with an Ultrabright Semiconductor Single-Photon Source. Phys. Rev. Lett.* **110** 250501 (2013).

[107] Matthiesen, C. et al. *Phase-locked indistinguishable photons with synthesized waveforms from a solid-state source. Nat Commun* **4** 1600 (2013).

[108] Rao, V.M. & Hughes, S. *Single quantum-dot Purcell factor and β factor in a photonic crystal waveguide. Phys. Rev. B* **75** 205437 (2007).

[109] John, S. *Strong localization of photons in certain disordered dielectric superlattices. Phys. Rev. Lett.* **58** 2486 (1987).

[110] Hughes, S., Ramunno, L., Young, J.F. & Sipe, J. *Extrinsic optical scattering loss in photonic crystal waveguides: role of fabrication disorder and photon group velocity. Phys. Rev. Lett.* **94** 033903 (2005).

[111] Sapienza, L. et al. *Cavity quantum electrodynamics with Anderson-localized modes. Science* **327** 1352–5 (2010).

[112] Faraon, A. et al. *Dipole induced transparency in waveguide coupled photonic crystal cavities. Opt. Express* **16** 12154–12162 (2008).

[113] Sollner, I. *Quantum Dots in Photonic Crystal Waveguides.* Ph. D. thesis, Niels Bohr Institute (2014).

[114] McNab, S.J., Moll, N. & Vlasov, Y.A. *Ultra-low loss photonic integrated circuit with membrane-type photonic crystal waveguides. Opt. Express* **11** 2927–2939 (2003).

[115] Burns, W., Milton, A. & Lee, A. *Optical waveguide parabolic coupling horns. Appl. Phys. Lett.* **30** 28–30 (1977).

[116] Kuhlmann, A.V. et al. *A dark-field microscope for background-free detection of resonance fluorescence from single semiconductor quantum dots operating in a set-and-forget mode. Rev. Sci. Instrum.* **84** 073905 (2013).

[117] Arcari, M. *Efficiency and Coherence of Quantum-Dot Single-Photon Sources.* Ph.D. thesis, Niels Bohr Institute (2015).

[118] Thoma, A. et al. *Exploring Dephasing of a Solid-State Quantum Emitter via Time-and Temperature-Dependent Hong-Ou-Mandel Experiments. Phys. Rev. Lett.* **116** 033601 (2016).

[119] He, Y. et al. *Indistinguishable Tunable Single Photons Emitted by Spin-Flip Raman Transitions in InGaAs Quantum Dots. Phys. Rev. Lett.* **111** 237403 (2013).

[120] Loredo, J. et al. *BosonSampling with single-photon Fock states from a bright solid-state source. arXiv preprint arXiv:1603.00054* (2016).

[121] He, Y. et al. *Scalable boson sampling with a single-photon device. arXiv preprint arXiv:1603.04127* (2016).

[122] Takahashi, H., Suzuki, S., Kato, K. & Nishi, I. *Arrayed-waveguide grating for wavelength division multi/demultiplexer with nanometre resolution. Electron. Lett.* **26** 87–88 (1990).

[123] Collins, M.J. et al. *Integrated spatial multiplexing of heralded single-photon sources. Nat. Commun.* **4** (2013).

[124] Mendoza, G.J. et al. *Active Temporal Multiplexing of Photons. arXiv preprint arXiv:1503.01215* (2015).

[125] Müller, M., Bounouar, S., Jöns, K.D., Glässl, M. & Michler, P. *On-demand generation of indistinguishable polarization-entangled photon pairs. Nature Photon* **8** 224–228 (2014).

[126] Maldonando, T.A. *Handbook of Optics, Vol. II*, Ch. 13 Electro-Optic Modulators (McGraw-Hill, Inc., 1995).

[127] Casson, J.L. et al. *Electro-optic coefficients of lithium tantalate at near-infrared wavelengths. J. Opt. Soc. Am. B* **21** 1948–1952 (2004).

[128] *Electro-optic Components and Systems.*

[129] *Model 25D Manual.*

[130] Wootters, W.K. & Zurek, W.H. *A single quantum cannot be cloned. Nature* **299** 802–803 (1982).

[131] Santori, C. et al. *Submicrosecond correlations in photoluminescence from InAs quantum dots. Phys. Rev. B* **69** 205324 (2004).

[132] *PicoHarp 300 Manual.*

[133] Gerry, C. & Knight, P. *Introductory quantum optics* (Cambridge university press, 2005).

[134] Rundquist, A. et al. *Nonclassical higher-order photon correlations with a quantum dot strongly coupled to a photonic-crystal nanocavity. Phys. Rev. A* **90** 023846 (2014).

[135] He, Y.M. et al. *On-demand semiconductor single-photon source with near-unity indistinguishability. Nat Nano* **8** 213–217 (2013).

[136] Somekh, S., Garmire, E., Yariv, A., Garvin, H. & Hunsperger, R. *Channel optical waveguide directional couplers. Appl. Phys. Lett.* **22** 46–47 (1973).

[137] Soldano, L.B. & Pennings, E. *Optical multi-mode interference devices based on self-imaging: principles and applications. J. Lightwave Technol.* **13** 615–627 (1995).

[138] Kennard, J. et al. *On-chip manipulation of single photons from a diamond defect. Phys. Rev. Lett.* **111** 213603 (2013).

[139] Wang, J. et al. *Gallium arsenide (GaAs) quantum photonic waveguide circuits. Opt. Commun.* **327** 49–55 (2014).

[140] Jöns, K.D. et al. *Monolithic on-chip integration of semiconductor waveguides, beamsplitters and single-photon sources. J. Phys. D: Appl. Phys.* **48** 085101 (2015).

[141] Rengstl, U. et al. *On-chip beamsplitter operation on single photons from quasi-resonantly excited quantum dots embedded in GaAs rib waveguides. Appl. Phys. Lett.* **107** 021101 (2015).

[142] Ulrich, R. & Ankele, G. *Self-imaging in homogeneous planar optical waveguides. Appl. Phys. Lett.* **27** 337–339 (1975).

[143] Syms, R.R. & Cozens, J.R. *Optical guided waves and devices* (McGraw-Hill, 1992).

[144] Taillaert, D. et al. *Grating couplers for coupling between optical fibers and nanophotonic waveguides. Jpn. J. Appl. Phys.* **45** 6071 (2006).

[145] Matthiae, M. *Efficient extraction of single photons from a quantum dot in a photonic crystal waveguide.* M. Sc. thesis, Niels Bohr Institute (2015).

[146] Bell, J. *On the Einstein-Podolsky-Rosen Paradox. Physics* **1** 195–200 (1964).

[147] Ekert, A.K. *Quantum cryptography based on Bell's theorem. Phys. Rev. Lett.* **67** 661 (1991).

[148] Bennett, C.H. & Wiesner, S.J. *Communication via one-and two-particle operators on Einstein-Podolsky-Rosen states. Phys. Rev. Lett.* **69** 2881 (1992).

[149] Kwiat, P.G. et al. *New high-intensity source of polarization-entangled photon pairs. Phys. Rev. Lett.* **75** 4337 (1995).

[150] Santori, C., Fattal, D., Pelton, M., Solomon, G.S. & Yamamoto, Y. *Polarization-correlated photon pairs from a single quantum dot. Phys. Rev. B* **66** 045308 (2002).

[151] Dousse, A. et al. *Ultrabright source of entangled photon pairs. Nature* **466** 217–220 (2010).

[152] Muller, A., Fang, W., Lawall, J. & Solomon, G.S. *Creating polarization-entangled photon pairs from a semiconductor quantum dot using the optical stark effect. Phys. Rev. Lett.* **103** 217402 (2009).

[153] Bao, X.H. et al. *Generation of narrow-band polarization-entangled photon pairs for atomic quantum memories. Phys. Rev. Lett.* **101** 190501 (2008).

[154] Hensen, B. et al. *Loophole-free Bell inequality violation using electron spins separated by 1.3 kilometres. Nature* **526** 682–686 (2015).

[155] Quesada, N. *Fusion gates with partially distinguishable photons.* Unpublished (2016).

[156] Briegel, H.J. & Raussendorf, R. *Persistent entanglement in arrays of interacting particles. Phys. Rev. Lett.* **86** 910 (2001).

[157] Walther, P. et al. *Experimental one-way quantum computing. Nature* **434** 169–176 (2005).

[158] Nielsen, M.A. *Optical Quantum Computation Using Cluster States* **93** 040503 (2004).

[159] Greenberger, D.M., Horne, M.A. & Zeilinger, A. *Going beyond Bell's theorem.* In *Bell's theorem, quantum theory and conceptions of the universe* (Springer, 1989), 69–72.

[160] Zhang, Q. et al. *Demonstration of a scheme for the generation of "event-ready" entangled photon pairs from a single-photon source. Phys. Rev. A* **77** 062316 (2008).

[161] Ralph, T.C., Langford, N.K., Bell, T. & White, A. *Linear optical controlled-NOT gate in the coincidence basis. Phys. Rev. A.* **65** 062324 (2002).

[162] Coffman, V., Kundu, J. & Wootters, W.K. *Distributed entanglement. Phys. Rev. A* **61** 052306 (2000).

[163] Predojević, A. & Mitchell, M.W. *Engineering the Atom-Photon Interaction: Controlling Fundamental Processes with Photons, Atoms and Solids* (Springer, 2015).

[164] James, D.F.V., Kwiat, P.G., Munro, W.J. & White, A.G. *Measurement of qubits. Phys. Rev. A* **64** 052312 (2001).

[165] Altepeter, J.B., James, D.F.V. & Kwiat, P.G. *Quantum State Estimation.* volume 649 of *Lecture Notes in Physics*, Ch. Qubit Quantum State Tomography (2004), 113–146.

[166] Marsili, F. et al. *Detecting single infrared photons with 93% system efficiency. Nature Photon.* **7** 210–214 (2013).

[167] Ollivier, H. & Zurek, W.H. *Quantum Discord: A Measure of the Quantumness of Correlations* **88** 017901 (2001).

Appendix A

One way computer

The following relations are used in the following derivation:

$$|\pm\alpha\rangle = \frac{1}{\sqrt{2}}(|0\rangle \pm e^{i\alpha}|1\rangle, \tag{A.1}$$

$$|\pm\rangle = \frac{1}{\sqrt{2}}(|0\rangle \pm |1\rangle) \tag{A.2}$$

$$|0\rangle = \frac{1}{\sqrt{2}}(|\alpha\rangle + |-\alpha\rangle) \tag{A.3}$$

$$|1\rangle = \frac{e^{-i\alpha}}{\sqrt{2}}(|\alpha\rangle - |-\alpha\rangle) \tag{A.4}$$

$$|+\rangle = \cos\left(\frac{\alpha}{2}\right)|\alpha\rangle + i\sin\left(\frac{\alpha}{2}\right)|-\alpha\rangle \tag{A.5}$$

$$|-\rangle = i\sin\left(\frac{\alpha}{2}\right)|\alpha\rangle + \cos\left(\frac{\alpha}{2}\right)|-\alpha\rangle \tag{A.6}$$

$$\tag{A.7}$$

The Bell pair in the computational basis $|\Phi^+\rangle = \frac{1}{\sqrt{2}}[|+\rangle|+\rangle + |-\rangle|-\rangle]$ can be utilized for simple one qubit rotations:

$$\begin{aligned} |\Phi^+\rangle = \frac{1}{\sqrt{2}}[|+\rangle|+\rangle + |-\rangle|-\rangle] = \\ \frac{1}{2}\left(\left[\cos\left(\frac{\alpha}{2}\right)|\alpha\rangle + i\sin\left(\frac{\alpha}{2}\right)|-\alpha\rangle\right]|+\rangle + \left[i\sin\left(\frac{\alpha}{2}\right)|\alpha\rangle + \cos\left(\frac{\alpha}{2}\right)|-\alpha\rangle\right]|-\rangle\right) = \\ \frac{1}{2}\left(|\alpha\rangle\left[\cos\left(\frac{\alpha}{2}\right)|+\rangle + i\sin\left(\frac{\alpha}{2}\right)|-\rangle\right] + |-\alpha\rangle\left[i\sin\left(\frac{\alpha}{2}\right)|+\rangle + \cos\left(\frac{\alpha}{2}\right)|-\rangle\right]\right) = \\ \frac{1}{\sqrt{2}}\left[|\alpha\rangle R_z(-\alpha)|+\rangle + |-\alpha\rangle R_z(-\alpha)|-\rangle\right] \end{aligned} \tag{A.8}$$

Alternatively if the initial cluster state is $|\Phi\rangle = \frac{1}{\sqrt{2}}[|0\rangle|+\rangle + |1\rangle|-\rangle]$ another type of qubit rotation is obtained:

$$|\Phi\rangle = \frac{1}{\sqrt{2}}[|0\rangle|+\rangle + |1\rangle|-\rangle] = \frac{1}{2}\left[(|\alpha\rangle + |-\alpha\rangle)|+\rangle + e^{-i\alpha}(|\alpha\rangle - |-\alpha\rangle)|-\rangle\right] =$$

$$\frac{1}{2}[|\alpha\rangle(e^{i\alpha/2}|+\rangle + e^{-i\alpha/2}|-\rangle) + |-\alpha\rangle(e^{i\alpha/2}|+\rangle - e^{i\alpha/2}|-\rangle)] = \frac{1}{\sqrt{2}}\left[|\alpha\rangle R_x(-\alpha)|+\rangle + |-\alpha\rangle R_x(-\alpha)|-\rangle\right] \tag{A.9}$$

For the three qubit horseshoe cluster state $|\Phi_{\text{lin3}}\rangle = \frac{1}{\sqrt{2}}(|+\rangle|0\rangle|+\rangle + |-\rangle|1\rangle|-\rangle)$ more complex

rotations are acheived:

$$
\begin{aligned}
|\Phi_{\text{lin3}}\rangle = \frac{1}{\sqrt{2}}(|+\rangle|0\rangle|+\rangle + |-\rangle|1\rangle|-\rangle) = \\
\frac{1}{2}\Big[(\cos(\frac{\alpha}{2})|\alpha\rangle_1 + i\sin\left(\frac{\alpha}{2}\right)|-\alpha\rangle_1)(|\beta\rangle_2 + |-\beta\rangle_2)|+\rangle_3 \\
+(i\sin(\frac{\alpha}{2})|\alpha\rangle_1 + \cos(\frac{\alpha}{2})|-\alpha\rangle_1)\frac{e^{-i\alpha}}{\sqrt{2}}(|\beta\rangle_2 - |-\beta\rangle_2)|-\rangle_3\Big] = \\
\frac{1}{2}\Big[|\alpha\rangle_1|\beta\rangle_2(\cos\frac{\alpha}{2}e^{i\beta/2}|+\rangle_3 + i\sin\frac{\alpha}{2}e^{-i\beta/2}|-\rangle_3) + \\
|\alpha\rangle_1|-\beta\rangle_2(\cos\frac{\alpha}{2}e^{i\beta/2}|+\rangle_3 - i\sin\frac{\alpha}{2}e^{-i\beta/2}|-\rangle_3) + \\
|-\alpha\rangle_1|\beta\rangle_2(i\sin\frac{\alpha}{2}e^{\beta/2}|+\rangle_3 + \cos\frac{\alpha}{2}e^{-\beta/2}|-\rangle_3) + \\
|-\alpha\rangle_1|-\beta\rangle_2(i\sin\frac{\alpha}{2}e^{\beta/2}|+\rangle_3 - \cos\frac{\alpha}{2}e^{-\beta/2}|-\rangle_3)\Big] = \\
\frac{1}{2}\left[|\alpha\rangle_1|\beta\rangle_2 R_z(-\alpha)R_x(-\beta)|+\rangle_3 + |\alpha\rangle_1|-\beta\rangle R_z(\alpha)R_x(-\beta)|+\rangle_3\right. \\
\left.+|-\alpha\rangle_1|\beta\rangle_2 R_z(-\alpha)R_x(\beta)|-\rangle_3 + |-\alpha\rangle_1|-\beta\rangle_2 R_z(\alpha)R_x(\beta)|-\rangle_3\right]
\end{aligned}
\tag{A.10}
$$

Appendix B

Estimating drop rate

The post-selected count rate extracted in Chapter 5 was done using the following Python script. The detected events are binned with a binwidth of 2 μs. The elapsed time where photon events occur is compared to the elasped time where no event is detected. In the following two seconds of integrationtime is used, since loading the full file requires more computer power than available. The error on the post-selected rate can thereby be reduced if a large integration time is used.

```
import numpy as np
import matplotlib.pyplot as plt

# Number of bins for binning
noBins=1000
# Load the channel timestaps
ch1=np.fromfile('/home/taubl/Downloads/Demuxg3/demux_260116_10min_aftecalib_400kHz_Ch1.ttd',dtype=int)
ch2=np.fromfile('/home/taubl/Downloads/Demuxg3/demux_260116_10min_aftecalib_400kHz_Ch2.ttd',dtype=int)
ch3=np.fromfile('/home/taubl/Downloads/Demuxg3/demux_260116_10min_aftecalib_400kHz_Ch3.ttd',dtype=int)

# Selecting the first 2 seconds of the Timestamps
ch1_2s=(ch1[0:np.argmax(ch1*1E-12>1)])*1E-12
ch2_2s=(ch2[0:np.argmax(ch2*1E-12>1)])*1E-12
ch3_2s=(ch3[0:np.argmax(ch3*1E-12>1)])*1E-12

#plotting
hfont= {'fontname':'Arial','size':9}
f,(ax1,ax2,ax3) = plt.subplots(3,sharex=True, sharey=True,figsize=(8.4/2.54,8.4/2.54))

# Binning in 2us bins
binnedCh1 = ax1.hist(ch1_2s,noBins)
binnedCh2=ax2.hist(ch2_2s,noBins)
binnedCh3=ax3.hist(ch3_2s,noBins)

# Calculates the post-selected Cnt
AverageCh1=np.average(binnedCh1[0],weights=binned[0].astype(bool))
PSCh1CntR=(Average*noBins)/np.amax(binned[1])
# Standard deviation on post-selected counts
```

```
29 std = np.sqrt(np.average((binned[0]-Average)**2, weights=binned[0].astype(bool)))
   # Standardeviation on the postselected rates
31 stdPSC=(std*noBins)/np.amax(binned[1])

33 # Calculate detected count rate and Standard deviations
   DetCh1=np.trapz(binned[0])/np.amax(binned[1])
35 DetCh2= np.trapz(binnedch2[0])/np.amax(binnedch2[1])
   DetCh3=np.trapz(binnedch3[0])/np.amax(binnedch3[1])
37 StdCH1=np.sqrt(np.trapz(binned[0]))/np.amax(binned[1])
   StdCh2= np.sqrt(np.trapz(binnedch2[0]))/np.amax(binnedch2[1])
39 StdCh3= np.sqrt(np.trapz(binnedch3[0]))/np.amax(binnedch3[1])
   # On ratio
41 Onratio= DetCntR/PSCntR
   OnSTD=(DetCntR/PSCntR)*np.sqrt(1/DetCntR+(stdPSC/PSCntR)**2)
```